IMAGE ANALYSIS APPROACHES TO COLORIMETRIC AND MULTISPECTRAL DETECTION OF HEAVY METAL OR BACTERIAL CONTAMINATION WITH PRINTED PAPER-BASED TEST DEVICES

by

Min Zhao

A Dissertation

Submitted to the Faculty of Purdue University

In Partial Fulfillment of the Requirements for the degree of

Doctor of Philosophy

School of Electrical and Computer Engineering

West Lafayette, Indiana

December 2021

THE PURDUE UNIVERSITY GRADUATE SCHOOL
STATEMENT OF COMMITTEE APPROVAL

Dr. Jan P. Allebach, Chair

School of Electrical and Computer Engineering

Dr. George T.-C. Chiu

School of Mechanical Engineering

Dr. Fengqing Maggie Zhu

School of Electrical and Computer Engineering

Dr. Michael D. Zoltowski

School of Electrical and Computer Engineering

Approved by:

Dr. Dimitrios Peroulis

Dedicated to my parents, my sister, my husband, and my lovely daughter.

ACKNOWLEDGMENTS

The meaningful journey at Purdue University changes my life in a wonderful way. I want to express my gratitude to my advisor, committee members, my lab mates and other friends, my research sponsor, and my family. Without the support they brought me, it would not be possible for me to complete this work.

First and foremost, I would like to express my sincere gratitude to my advisor, Prof. Jan P. Allebach, for the great opportunity to do research with him! Prof. Allebach constantly gave me professional guidance, exposed me to novel research ideas, and always encouraged me during my research. I have learned a lot from him both professional knowledge and the attitude of doing research which encourages me to ask myself to be a dedicated person. I would like to thank him for his energy, organization, humble and well cultivation that can influence me forever, and for the support to my family during my Ph.D. period.

I would also like to give sincere thanks to Prof. George T.-C Chiu, for his valuable guidance that how to think and solve the problems of research or life. Thank him for showing me how to be creative, work smart and expert in the fields.

Also, I would like to thank my other committee members, Prof. Fengqing Maggie Zhu, and Prof. Mike D. Zoltowski for their important feedback and advice on my research.

I want to thank my research sponsor, United States Department of Agriculture and their employees for their support during my Ph.D. study at Purdue. My gratitude also goes to all the EISL colleagues for their help in my Ph.D study.

Last but not least, I would like to thank my parents, my parents-in-law, my sister, and my husband for all their unconditional love and support on my PhD journey. I wish to thank my lovely daughter, Elizabeth, who is a source of lots of strength and joy for me.

TABLE OF CONTENTS

LIST OF TABLES

LIST OF FIGURES

LIST OF SYMBOLS

V	heating pulse voltage
W	heating pulse width
Hz	printing frequency
δ	compactness
A	area of shape
R	radius of the minimum enclosing circle for shape
$X,\ Y,\ Z$	pixel value of $X,\ Y,\ Z$ channels.
ΔE	Euclidean distance between two points in $CIE\ Lab$ color space
$L^*,\ a^*,\ b^*$	pixel value of $L,\ a,\ ,b$ channels.
$L_{ave},\ a_{ave},\ b_{ave}$	average value of $L,\ a,\ ,b$ channels
ω	probability of a class
μ	average gray values of a class
σ	variance
α	Lagrange multiplier

ABBREVIATIONS

LOD	limitation of detection
PTSs	printed test strips
CFU	colony-forming unit
DOD	drop-on-demand
TIPS	Thermal Inkjet PicoJet System
BSA	Bovine serum albumin
PBS	phos-phate-buffered saline
Biotin-BSA	Biotinylated BSA
Y-biotin	Lucifer yellow-labeled biotin
CCD	Charge Coupled Device
DI	Deionize
CFU/mL	amount of bacterial colonies per milliliter
μPAD	microfluidic paper-based analytic devices
Hg	Mercury
As	Arsenic
ppm	parts per million
PCA	principal component analysis
SFS	sequential forward feature selection
k-NN	k-nearest-neighbor
RF	random forest
CNN	convolutional neural networks
GAN	generative Adversarial Network
AUG	data set enlarged using traditional data augmentation

ABSTRACT

Nowadays, safety in food has become critical. The main two types of threats related to food safety are foodborne pathogens and heavy metals. One of the most common foodborne pathogens that can be found in our daily food is Escherichia coli O157:H7 (*E. coli* O157:H7). Human infections with *E. coli* O157:H7 poses severe disease in our bodies and even death. Heavy metals, Mercury (Hg), Arsenic (As), Copper (Cu), and so on can be enriched in living tissue through food chains and have proven to be harmful to human health at low concentrations. So, the detection of the contaminants in daily food and drinking water is crucial for global public health. To date, the widely used pathogen detection methods and heavy metal detection methods are expensive, involve laborious procedures, and cannot support on-site detection. In this dissertation, two different novel printing platforms, and accompanying rapid, microfluidic architecture platforms are proposed for the detection of *E. coli* O157:H7, and As and Hg, respectively. These devices can be fully integrated with a mobile phone and an image analysis pipeline to capture and analyze the sensor images on-site.

The first system that we develop consists of inkjet printed lateral diffusion strips for the capture of *E. coli* O157:H7. This effort includes the characterization of the consistent size droplets used to develop the print masks, and functional printing of the test and control lines with the corresponding DNA solutions. Then we propose an image analysis method to read the responses of the test strips to the presence of targets, and quantitatively correlate the color intensity of responses to the target concentrations. Finally, the response variation of the optical properties of the test lines detecting the target at the same concentration is investigated. To reduce the sample-to-sample variation in response to *E. coli* O157:H7, and in an effort to reduce material cost and printing time, we optimize the numbers of print layers and explore various well-used image segmentation methods to detect the response in the test lines of test strips. The usefulness of these segmentation methods is evaluated by comparing the response variance of the corresponding segmentation results.

To move towards multiplexed heavy metals detection of As and Hg, we design a second patterned microfluidic paper-based device, capable of instrument-free, portable, and

multiplexed sensing detection via aptamer recognition. We explore three different printing technologies for fabricating these devices, and choose screen printing with UV cured inks for further development. We then conduct empirical studies to optimize the device geometry. We propose three image analysis methods to obtain a higher prediction accuracy with our developed paper-based devices for detecting and measuring heavy metal contaminants in food or liquids. (1) We use ΔE from a white background as our baseline method to correlate the optical properties with the different concentrations of the target, and optimally quantize these responses into five groups to evaluate the prediction accuracy. (2) We propose a CNN classifier and explore two kinds of data augmentation techniques to compare their effectiveness for the classification task. (3) We consider the use of the spectral reflectance of the sensor pad, then develop two different machine learning approaches: k-nearest-neighbor with sequential forward feature selection to determine the best number of features, and random forest with principal component analysis for feature reduction for classifying the level of contamination by As^{3+} into one of five categories. The accuracy of these three models is compared by implementing them with the same training and test datasets.

1. INTRODUCTION

Inkjet printing has been around for several decades. The most popular application of this printing technology has been to print paper documents containing text and graphics. From the mid-1990s, the field of bio-printing began to grow, with a rapid increase after 2000 because inkjet printers began to be used for dispensing functional materials. The incorporation of printing technology with biomaterials has recently gained considerable attention. For instance, printing techniques have been used for the regeneration of bone or ear tissues [1]. Inkjet printing is an advanced technique enabling the deposition of various kinds of solutions (biomolecules, polymers, metals) onto different types of substrates (cellulose, polymer, silicon.). It enables fast printing of any computer-generated pattern onto substrates by precise placement of pico-to-nanoliter volumes of inks [2].

Currently, mobile phones are low-cost, and affordable, so they are widely available across the globe. For mobile phones, the integration of cameras, light-sensors and microphones has enabled mobile phones become a popular and accessible platform for diagnostic systems. For example, pregnacy monitoring can be done on a mobile phone [3][4], and food dietary control [5].

1.1 Inkjet Printing System for Foodborne Pathogen Detection

Recently printing technologies have become very popular in environmental pollution and food safety testing applications. According to the World Health Organization (WHO), there are estimated 600 million people falling ill after eating contaminated food and 420 thousand deaths every year [6]. The most common foodborne pathogens include Salmonella, Campylobacter, and Enterohaemorrhagic Escherichia coli. Among these foodborne pathogens, *E. coli* O157:H7 can be easily found in contaminated water and contaminated food, especially undercooked ground beef, milk and juice, raw fruits and vegetables. It is known that *E. coli* O157:H7 can cause bloody diarrhea and sometimes cause kidney failure and even death. Therefore, an affordable, rapid and simple method for detecting *E. coli* O157:H7 is more and more in demand. The manufacturing process of inkjet printing can guarantee rapid, reliable,

and reproducible mass production of functional biosensors with specific detection properties at low cost.

The goal of our research is to design printed test strips (PTSs) to be used for the detection of *E. coli* O157:H7. Each functional PTS with two printed lines: the test line and the control lines, is intended to be affordable, portable, sensitive, rapid, and easy-to-use. Natural cellulose paper (Hi-flow HFC075, EMD Milipore, www.emdmilipore.com) is the substrate and the printing consists of two types of DNA-based biomaterial (the biomaterial on the test lines and control lines, respectively: Carboxyl functionalized Aptamer sequence, and Biotin DNA complementary sequence). To precisely control the amount of the DNA solution and to design a system for reproducible mass production, a piezoelectric inkjet printer PipeJet (BioFluidiX, Freiburg, Germany) with deposition of single droplets in the range of 2 - 70 nL is used to print the DNA solution onto the substrates. The focus of the functional printing part is to develop processes for inkjet and roll-to-roll patterning of nano-functionalized biocompatible and biodegradable cellulose test strips, therefore enabling the efficient manufacture of food pathogen biosensors. To date, we have fabricated and used the PTSs to successfully detect the presence of foodborne pathogens (*E. coli* O157:H7), and confirm an immune detection limit of 10^2 CFU/ml (CFU is an acronym for Colony Forming Unit).

1.2 Image Analysis Pipeline to Capture and Analyze the Responses in Lateral Diffusion Strips

In Chapter 2 and 3, we develop the inkjet printing process for producing the pattern for the capture of *E. coli* O157:H7, and design an image analysis method to detect the responses in test lines of test strips. In the following sections of those chapters, we first characterize the consistent size droplets to design the print mask, and functionally print the test and control lines with the corresponding solutions. We then detect *E. coli* O157:H7 with different concentrations to validate our approach by showing the responses in test lines and control lines of the PTSs. Our image analysis method deploys a quantitative metric to characterize the responses in the test lines of the images captured by a mobile camera. We also correlate the color change of the response area with the concentration of the target and determine the limitation of detection (LOD) of our biosensor using our developed image

analysis pipeline. Finally, we assess the variation among the responses in test lines of test strips by correlating the color intensity under a fixed concentration.

So, our approach successfully combines three technologies: aptamer-based detection, reproducible mass production by inkjet printing, and image analysis with a mobile phone camera to quantitatively correlate color intensity to pathogen concentration. We will present the detailed information of the last two technologies in Chapters 2 and 3.

1.3 Printing System and Traditional Image Analysis Model for Heavy Metal Detection

In Chapters 2 and 3, we discuss the inkjet printing system and the image analysis pipeline for foodborn pathogen *E. coli* O157:H7 detection. Beyond the foodborne pathogen *E. coli* O157:H7, we notice that the presence of heavy metals in food chains also poses a threat to public health. Heavy metals, including Mercury (Hg), Arsenic (As), Copper (Cu), and so on can be enriched in living tissue through food chains and have proven to be harmful to human health at low concentrations. Currently, heavy metal detection methods used are Mass spectroscopy, Atomic Emission Spectroscopy, Potentiometric Methods, and so on. These methods are sensitive but expensive and require expensive equipment, trained personnel and cannot support on-site detection. Therefore, rapid detection methods for heavy metal pollutants are more and more in demand.

During the last few decades, a wide variety of microfluidic paper-based biosensors have been successfully developed, demonstrating powerful tools for detecting food and environmental contamination. Microfluidic paper-based analytic devices (μPADs), developed in 2007 by Whiteside's team, have the characteristic of controlling a fluid motion via capillary force through specially designed microfluidic channel patterns on cellulose paper. As the major component of μPADs, cellulose papers with flexible porous fiber structure can wick liquids in small volumes without the need for external pumping equipment. The major task in the fabrication of μPADs is to create well-defined, millimeter-sized dimensional channels, comprising hydrophilic paper bounded by hydrophobic materials (wax or UV-curable inks) on cellulose papers. The heavy metals can be detected by gold nanoparticles (AuNPs) usually preloaded in reaction zones, by providing colorimetric signals in biosensors. The colorimetric

signals in the detection zones are commonly collected using a professional digital camera or a high-resolution scanner. Then, the color intensity of the signal in the captured images will be analyzed by some open source software.

Unsurprisingly, μPADs have gained great attention due to their ease of use, low cost, amenability to colorimetric detection, and little test sample consumption. To detect multiple targets in one test, which is hard to achieve with traditional lateral flow strips, our group focuses on developing a novel paper-based biosensor for colorimetric detection of two types of heavy metals: As and Hg. In Chapter 4, we first present paper-based devices fabricated by different technologies with different materials used to pattern hydrophobic walls across chromatography paper. Second, we propose preliminary patterns for multiple and multiplexed detection. Then, we detect the heavy metals at different concentrations to validate our approach. Finally, our optical system and image analysis pipeline are shown to obtain consistent data acquisition captured by a mobile phone camera, and deliver quantitative responses to correlate the colorimetric change of the biosensors to the concentration of the target substance.

1.4 Spectral Imaging to Differentiate Contaminant Levels

In Chapter 4, we show that our image analysis pipeline delivers quantitative responses to correlate the colorimetric change of the biosensors to the concentration of the target substance. For this base model, we used the grayscale values as a metric, calculating average $CIE\ \Delta E$ from the white reference, to characterize the response of the paper-based devices, and to correlate the response with the concentration of the analytes. Nonetheless, we notice that the relationship is not monotonic and the $CIE\ \Delta E$ data from the different concentrations overlaps a lot. Still, the detection of lower contamination levels using traditional image analysis remains challenging due to the small number of available data samples and the insufficient utilization of the spatial information contained in the sensor pad images.

To overcome this challenge, we use the spectra data of the colorimetric response pads and propose two kinds of classification models for differentiating contaminant levels with high test accuracy. In the first model, we apply the sequential forward selection algorithm [7] to select

optimal wavelength features in combination with the k-NN classifier [8] to discriminate five contaminant levels. The second technique comprises principal component analysis (PCA) used as a dimensionality reduction technique combined with the random forest (RF) classifier [9] to classify five contaminant levels. Our proposed system is trained and evaluated on a limited dataset of 126 spectral responses of five contamination levels. Our algorithms can yield 77% and 87% average accuracy, respectively.

In Chapter 5, we present an overview of the base model, the pipelines and the comparison of our proposed two classification models, and a phone-based narrow-band spectral imaging system that can obtain the camera spectral response for accurate and precise heavy metals analyses with the aid of a narrow bandpass filters in front of a cell phone's camera lens.

1.5 Deep Learning Approach for Classifying Contamination Levels with Limited Samples

To improve the accuracy of our previously developed paper-based devices for detecting and measuring heavy metal contaminants (As^{3+} and Hg^{2+}) in food or liquids, we explore some deep learning methods because convolutional neural networks (CNN) have gained tremendous popularity in computer vision, especially in the image classification domain for better performance than popular image processing methods. Deep learning algorithms yield high classification accuracy by using large, annotated datasets of images. Therefore, to develop accurate image classifiers for the contamination-levels classification task, we needed a large dataset of images of colorimetric responses. However, obtaining large-scale datasets of detection images of contamination levels is challenging because of limited test samples.

In Chapter 6, we aim to solve the classification problem posed by a small scale of data samples and large intra-class variance. To obtain large-scale datasets of detection images of contamination levels, we explore traditional data augmentation and GAN-based augmentation techniques for synthesizing realistic colorimetric images; and we propose a CNN classifier for five-contamination-levels classification. Our proposed system is trained and evaluated on a limited dataset of 126 phone captured images of five contamination levels, and is compared with our previous work. Our system yields 88.1% classification accuracy and 91.9% precision, demonstrating the feasibility of this approach. We hope that the proposed meth-

ods can be a strong candidate for phone-based contamination-levels detection. Because the user need only take an image of the test response using his or her phone camera and feed the captured image into the proposed model, the model can automatically classify the test sample's contamination level.

2. PRINTING SYSTEMS AND PRINTING OPTIMIZATION

There are two main technologies in use in drop-on-demand (DOD) inkjet printers: thermal DOD and piezoelectric DOD. In the thermal inkjet process, the print cartridges consist of a series of tiny chambers, each containing a heater, all of which are constructed by photolithography. To eject a droplet from each chamber, a pulse of current is passed through the heating element causing a rapid vaporization of the ink in the chamber and forming a bubble, which causes a large pressure increase, propelling a droplet of ink onto the paper. The ink's surface tension, as well as the condensation and resultant contraction of the vapor bubble, pulls a further charge of ink into the chamber through a narrow channel attached to an ink reservoir. For a piezoelectric printer, the applied voltage can change the piezoelectric material shape to generate a pressure pulse in the fluid, which forces a droplet of ink from the nozzle.

2.1 Thermal Inkjet Printing System

There is a thermal inkjet printer: Thermal Inkjet PicoJet System (TIPS, HP brand), in our Spira Lab. It has replaceable tips which has multiple nozzles per tip and the drop volumes between 2 pl and 200 pl. Figure 2.1 shows the installation of TIPS. There are two major printing parameters determining the quality of ejected drops. The detail information of printing parameter optimization can be found in the Section 2.4. Since the working temperature of this printing system varies according to the kinds of inks, we were concerned that the high working temperature of this thermal inkjet printer could affect the activity of the proteins during printing process.

2.2 Pieozoelectric Inkjet Printing System

We also have a pieozelectric inkjet printer in our Spira lab: PipeJet inkjet (BioFluidiX, Freiburg, Germany). It has disposable pipes with a single nozzle. The range of ejected volumes varies from 10 to 60 nL. Figure 2.2 shows the set up of the PipeJet printing system.

Since ejection of the drops is caused by a pressure pulse, we believe that this printer cannot affect the activity of proteins.

2.3 Protein Printing

To test the survivability of the protein and the functionality after thermal inkjet deposition, we first did protein printing experiments [10]. The basic idea is to print 4 different kinds of protein in a substrate. A schematic of the experiment is shown in Figure 2.3. After final printing, an examination of the glass slide under a fluorescent microscope revealed the yellow letters, , as illustrated in Figure 2.4. It indicates that the printing did not interfere significantly with the structures of the proteins, or at least their active sites. These results suggest that the TIPS thermal inkjet printer can be used for high-throughout colorimetric biochemical assays.

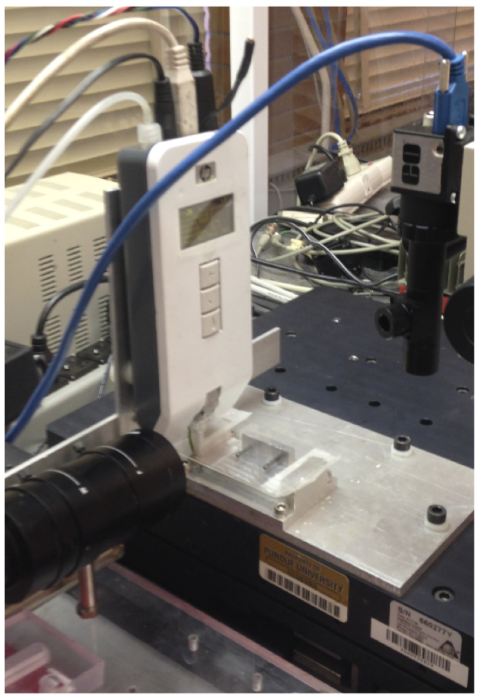

Figure 2.1. TIPS is mounted in a platform.

2.4 Printing Optimization

Both electrophotographic (laser) and inkjet technologies can generate artifacts that limit print quality: banding and dot gain, dot irregularity with creation of satellites. To have a better print quality with inkjet, consistent droplets without satellites are required [11], which can be achieved by tuning printing parameters. They can also influence the fabrication process. For inkjet, these parameters include the print mode, print mask, and number of print passes. To design the print masks for the DNA-based solution, the average droplet volume and the average diameter of the deposited droplets on the substrate need to be determined.

2.4.1 System

The inkjet systesm used for our current work is shown in Figure 2.5. The system consists of an XY motorized stage (Anorad WKY-150) with an encoder resolution of 0.5 μm, an op-

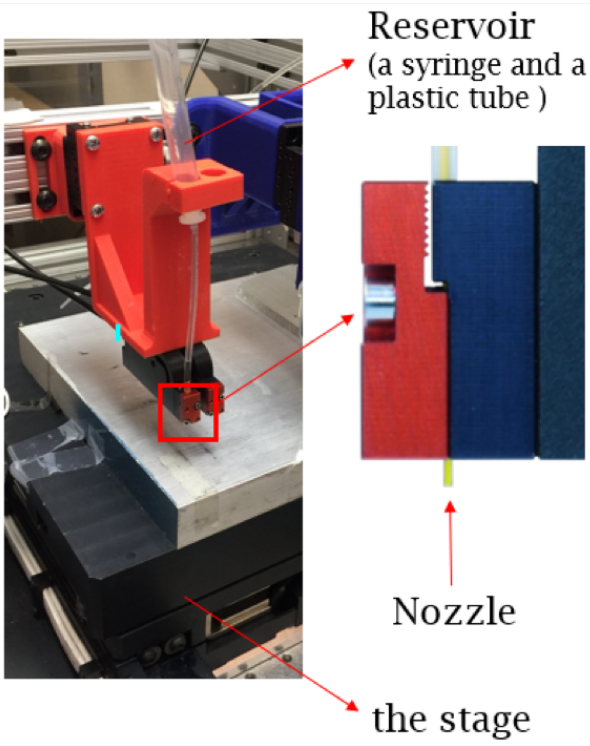

Figure 2.2. Set up of the PipeJet printer system.

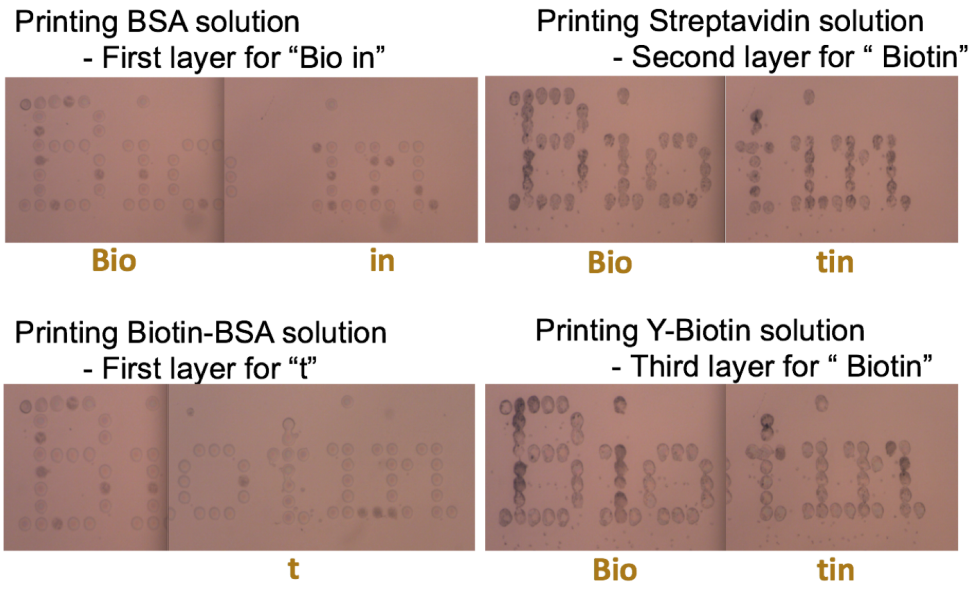

Figure 2.3. Views of our protein printing pattern on a glass slide.

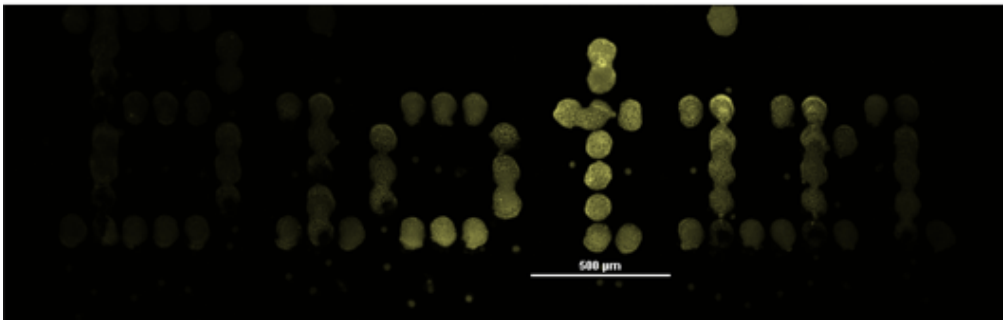

Figure 2.4. Fluorescent image of protein printing pattern.

tical system for ink ejection visualization, a stationary PipeJet piezoelectric droplet ejection system with one nozzle of diameter 200 μm that can eject a single droplet in the range of 2 - 70 nL at an ejection frequency ranging from 1 to 100 Hz, and a stationary TIPS with multiple nozzles that can eject a single droplet in the range of 2 - 200 pL [12]. We use a visual C-based printing software package to read an input bitmap image and pixel resolution, then correlate the controller with dot positions. The controller sends trigger signals of ejection to the printer at prescribed addresses when the stage moves beneath the printer [13][14].

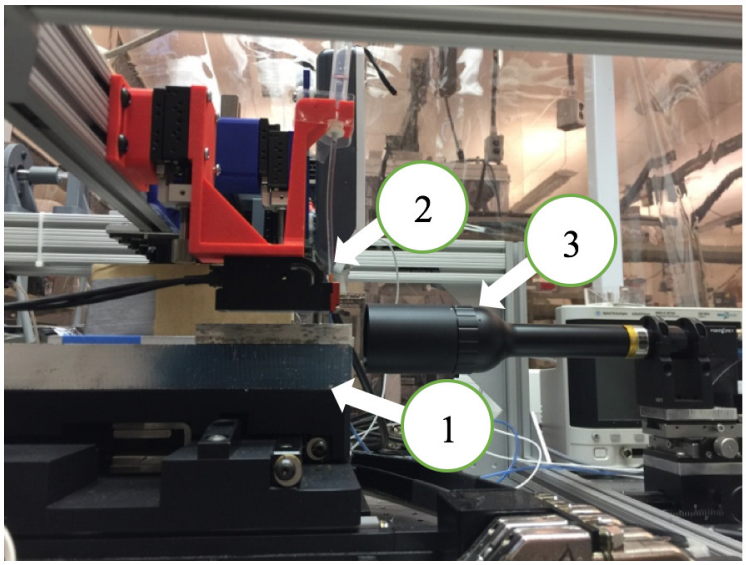

Figure 2.5. Inkjet system includes: (1) An XY motorized stage, (2) A PipeJet printer, (3) An optical system.

2.4.2 Consistent droplets and their volume

One of the sources of artifacts in the inkjet process is the creation of satellites, which occurs due to the separation of ink emerging from the nozzle exit. To view the ejection result, we set up an optical system, as illustrated in Figure 2.5 [13]. The optical system mainly consists of a PipeJet Inkjet System or a TIPS Inkjet System, a SPiiPlus Series motion controller, a stroboscope light, a CCD camera (Point Grey Flea3 USB3.0: FL3-GE-13Y3M-C), and a three-axis optical table (NRC pneumatic isolation table type XL-A). A PipeJet with one nozzle is installed on the top of the three-axis table and the nozzle exit is oriented toward gravity. The controller sends the trigger signals to the printer, and also sends the delay unit trigger signals to the stroboscope light. After the printer receives the trigger signal, the images of the ejected droplets can be captured by the CCD camera, displayed on the monitor screen, and stored in a file. Figure 2.6 shows the schematic view of the optical system for viewing droplet formation. The detailed components of this optical system are illustrated in Figure 2.7.

Thermal Inkjet PicoJet System (TIPS)

The printing system can be tuned to produce droplets without satellites. For the TIPS system, the key printing parameters are the operating voltage of the heating pulse (V) and

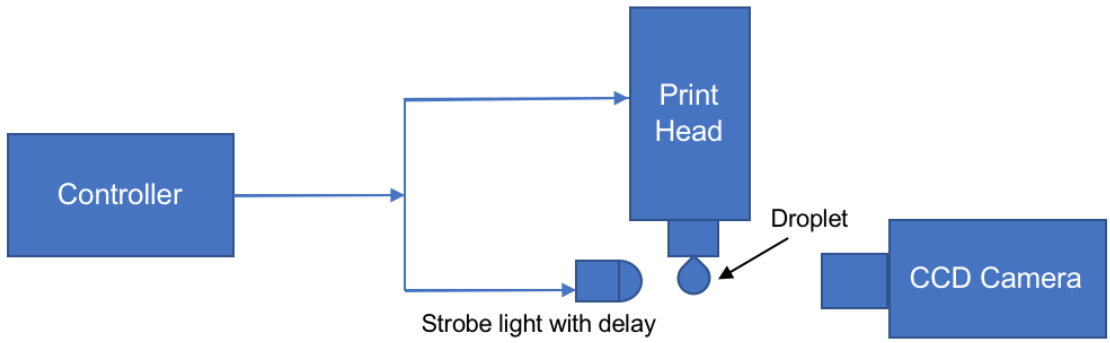

Figure 2.6. A schematic view of the optical system for viewing droplet formation.

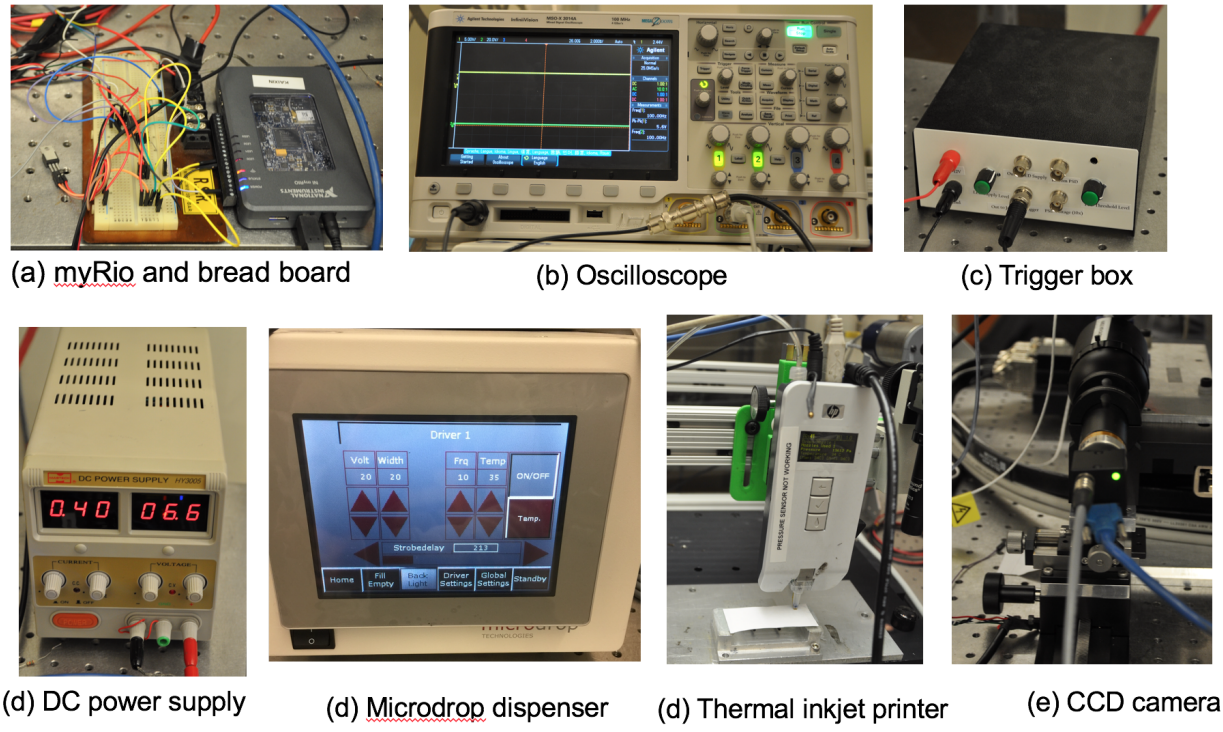

Figure 2.7. The components of our optical system.

the width of heating pulse (W). The print head was installed on the top of the work platform and the TIP 43 nozzle exit was oriented toward gravity. We use Deionized (DI) water as ink. The frequency of the heating pulse and the camera are fixed at 100 Hz, the operating pulse width and pulse voltage are varied in a range from 0.06 to 0.58 μs with an increment of 0.02 μs, and 15 to 29.25 V with an increment of 0.25 V, respectively.

As we tune the printing parameters during the ejection process, the ejection results can be recorded, as illustrated in Figure 2.8. By observing the number of satellites from the captured images, we make a table to record the printing results for different voltage and pulse width, as illustrated in Figure 2.9. We notice that there are 79 pairs data (green area) can satisfy no satellite during water ejection. We also observe that low voltage tends to producing consistent droplets without satellites when printing a low viscosity fluid.

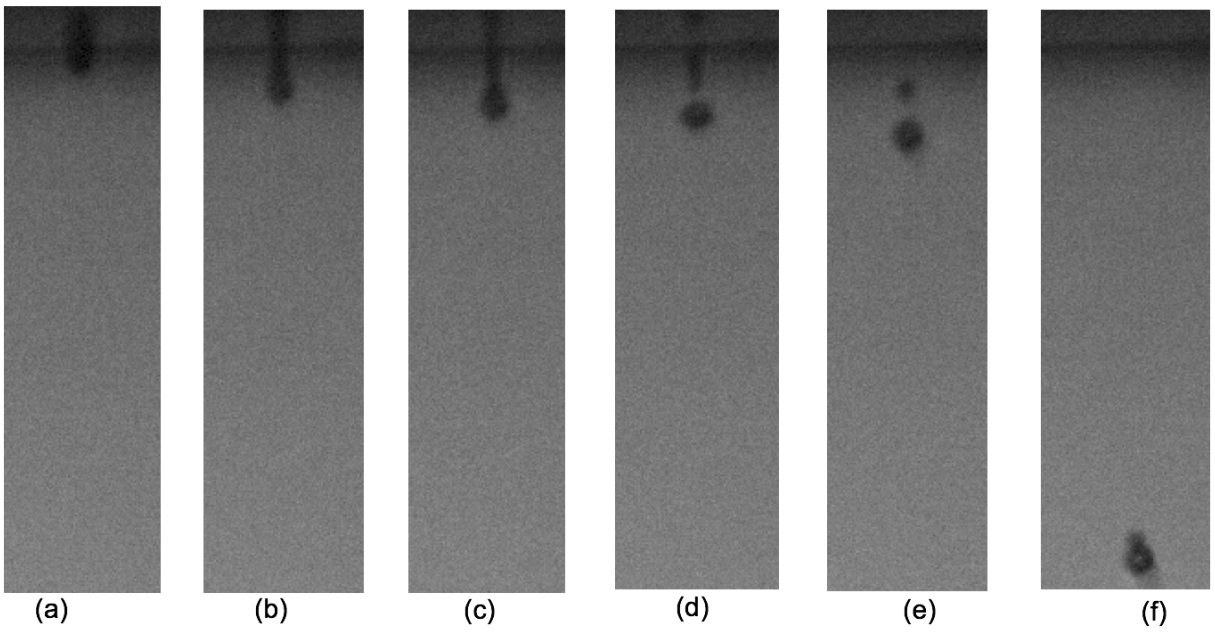

Figure 2.8. Temporal evolution of DI water ejection at V = 18.75 V and W = 0.18 μs. (a) Droplet just ejected from the nozzle exit; (b) Eyedrop-like shape; (c, d) A round droplet flies away from the ejected water droplet, and one small satellite droplet appears; (f) Main droplet and satellite merged together.

Piezoelectric inkjet PicoJet system

For our PipeJet printer, there are two major printing parameters that can affect printing quality: Stroke and Stroke velocity. The stroke is the ratio of the piston displacement to the maximum displacement, and the stroke velocity is the velocity of the displacement of the piston.

To find the relationship between the printing quality and printing parameters, we capture the images of the ejection results when tuning the printing parameters, as illustrated in Figure 2.10. In our experiment, the ink is Deionized (DI) water, the frequency of the firing is fixed at 100 Hz, the dispensing nozzle is Pipe 200, and the operating stroke and stroke velocity

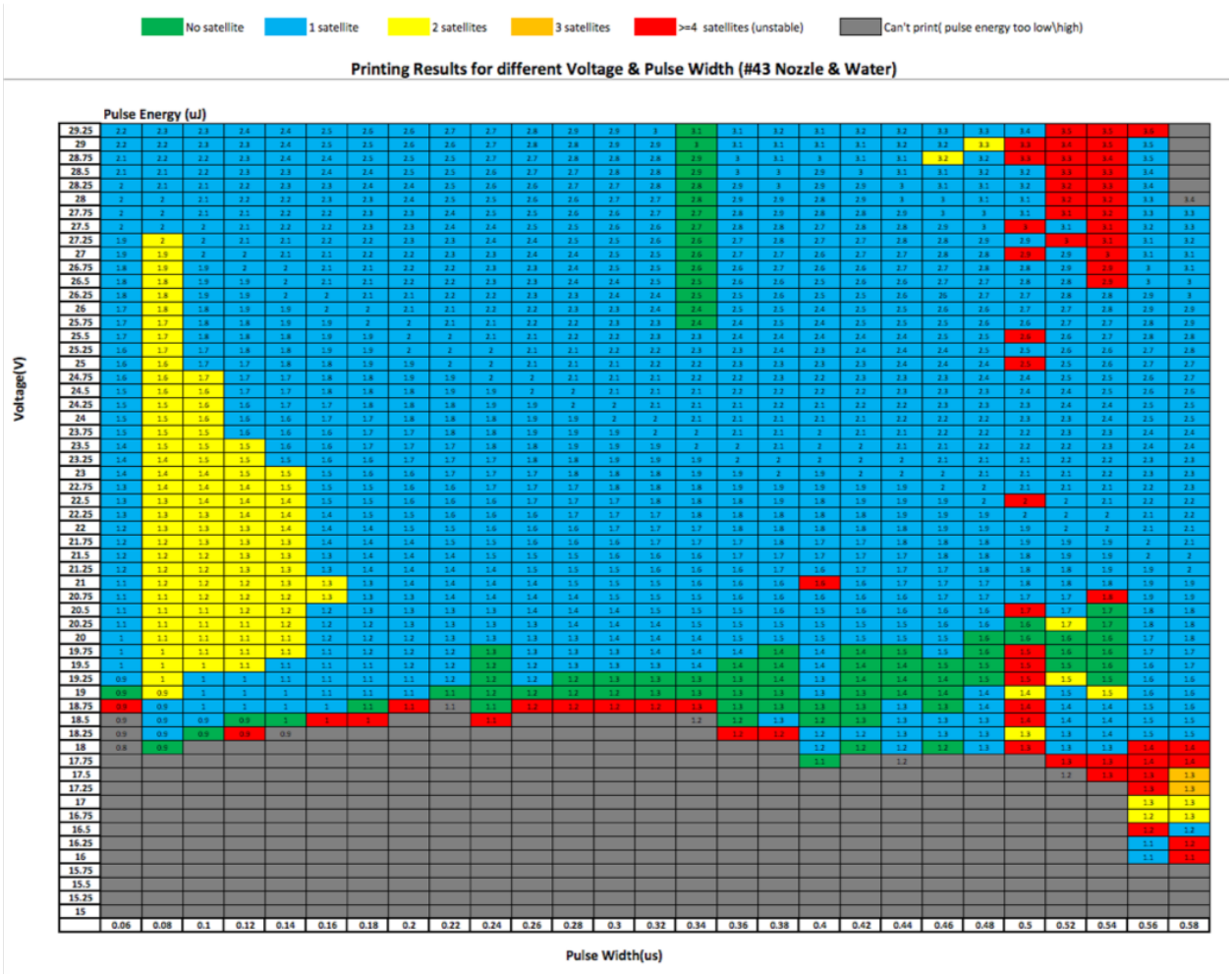

Figure 2.9. The printing results at different voltages and pulse widths for the TIPS.

are varied in a range from 0 to 100% with an increment of 10%, and 0 to 100 μm/ms with an increment of 10 μm/ms, respectively. The results are shown in Figure 2.11. We notice that there are 14 pairs of data (green area) can satisfy no satellite during water ejection. For low viscosity fluids, the tendency is to produce consistent droplets without satellites through high stroke injection.

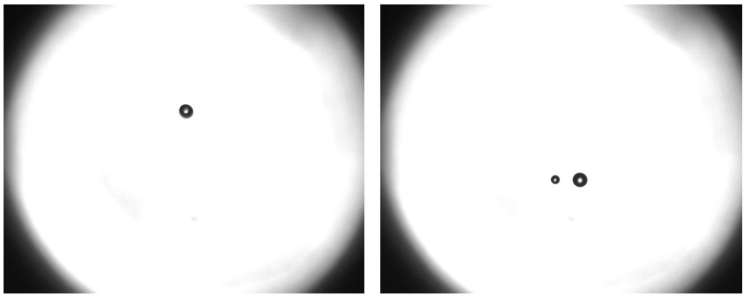

Figure 2.10. (a) The process of DI water drop ejection when the stroke and the stroke velocity equal 0% and 80 μm/ms, respectively, resulting in only one droplet. (b) The process of DI water drop ejection when the stroke and the stroke velocity equal 0% and 90 μm/ms, respectively, resulting in one main droplet and a satellite.

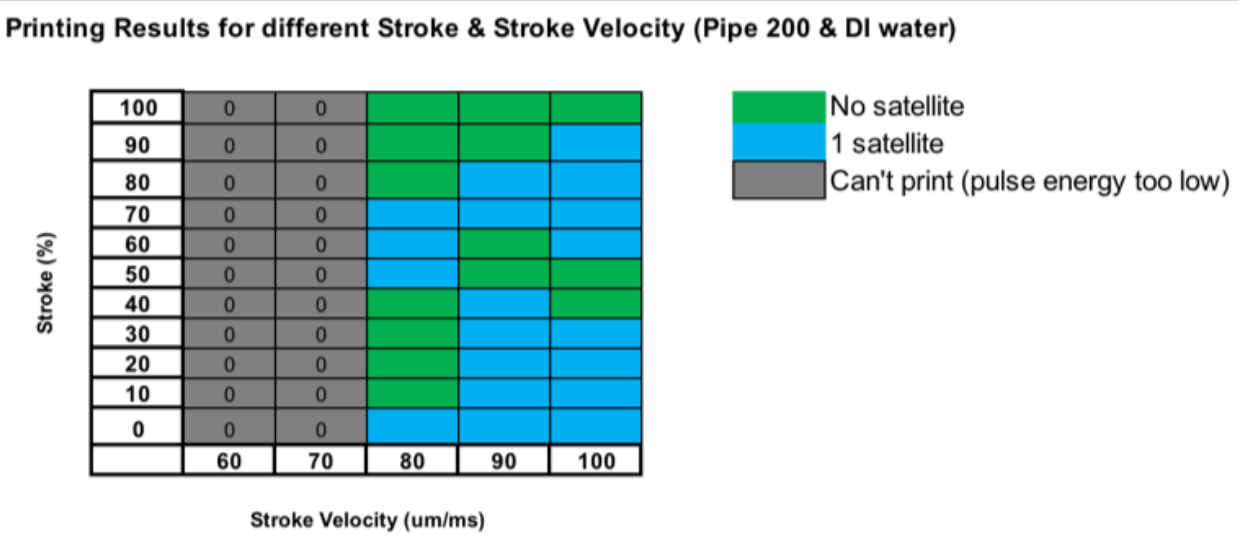

Figure 2.11. The printing results at different strokes and stroke velocities for the PipeJet system.

2.4.3 Dot Analysis

Dot diameter

To measure the average diameter of the drops produced by the PipeJet system after impacting the substrate, we first design a test pattern which can quantify the measurement of the dot size, and the presence or absence of satellites.

The test pattern we designed is a 10×10 pixel grid of single drops, each separated by a single pixel. Hence, there are a total of 100 dots in the test pattern, as illustrated in Figure 2.12(a) [15]. The print mode parameters used to print the test pattern are as follows:

Printing frequency: 100 Hz, Stroke: 100%, Stroke velocity: 100 μm/ms, Unidirectional printing, Media advance speed: 2 mm/s, Media return speed: 20 mm/s, Nozzle resolution: 200 μm, Ink: black ink (BCH), Substrate: Hi-flow HFC075, Standoff distance between the print head and the substrate: 1 mm.

Then we scanned the printed test pattern using an EPSON 10000XL (Epson America, Inc., Long Beach, CA, USA) flatbed scanner with resolution 1000 dpi, and obtained the grayscale image, as illustrated in Figure 2.12(b). The threshold for the image binarization is calculated using Otsu's method to find the threshold that maximizes the between-class variance [16]. Figure 2.12(c) shows the corresponding binary image. We then find the boundaries delimiting dot regions by vertically and horizontally projecting the data of the binary image, as illustrated in Figure 2.12(d). With the aid of these boundaries, we can calculate the total number of nonzero pixels for each dot. The average diameter of the dots can be calculated using the following equation, assuming that each dot is circular.

$$\mathrm{D} = \sqrt{\frac{4 \cdot N \cdot S}{\pi}}, \tag{2.1}$$

where N is the number of pixels of a dot, and S is the area of a pixel. Based on the above image analysis pipeline, we calculate that the average diameter of droplets printed by TIP with Nozzle 43 and PipeJet printer with Pipe 200 are about 51.46 μm, and 1004.10 μm, respectively.

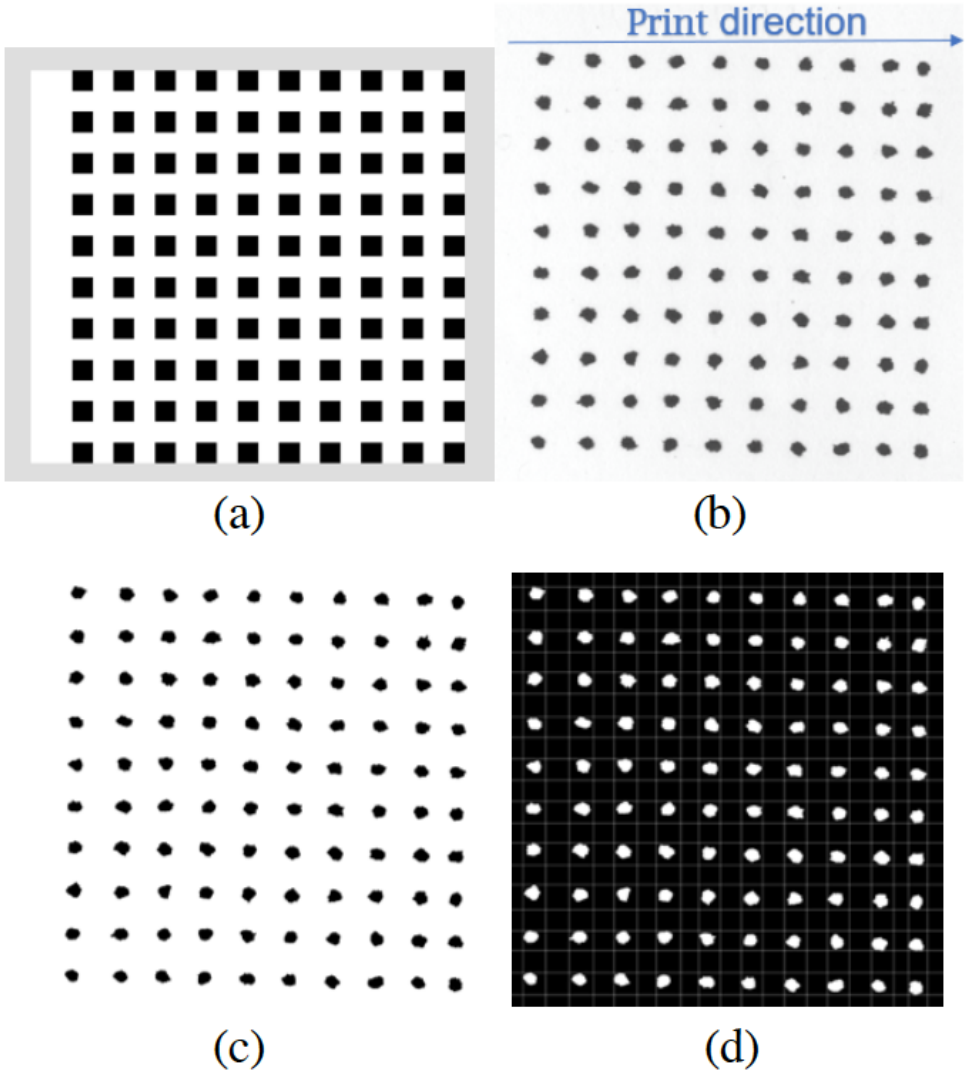

Figure 2.12. (a) Test pattern for dots characterization, (b) Print result of test pattern scanned at 1000 dpi with EPSON 10000XL with no satellites, (c) Corresponding binary image, (d) Boundaries delimiting dot regions shown in white.

Droplets placement accuracy

In order to control the printing quality, such as the straightness of a printed line, we need to know how much accuracy of drop placement the printing system can achieve. The ideal case is that centroids of the following black dots can be connected in a straight line, and the distance between adjacent black dots is equal, as illustrated in Figure 2.13(a). Figure 2.13(b) shows that in practice, centroids of the black dots do not lie on the same line, and

the distances between each adjacent black dots are unequal, which can affect the geometry design of the dot array.

Figure 2.14 shows the schematic of the skew estimation and the misalignment measurement. The total misalignment is estimated by computing the orthogonal distance between the dot centroid and its row regression line.

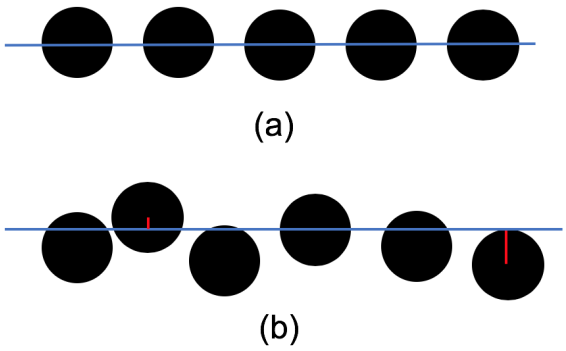

Figure 2.13. Schematic of droplets placement accuracy.

To calculate the printed dots misalignment, we use the printed test pattern (10 × 10 dots) to do the following steps:

1. Calculate the centroid of each dot.

2. Find a fitting straight line to each of the rows or columns of dot centroids via linear regression.

3. Calculate the angle of skew by finding the mean orthogonal regression line, as illustrated in Figure 2.14.

4. Calculate the orthogonal distance between centroids of dots and the corresponding mean fitting line, which is shown in Figure 2.15.

Figures 2.16(a) and (b) show the distribution for the TIPS of computed misalignments for 100 points in the row and column directions, respectively. The corresponding ranges of misalignment values are [-50 , 30] and [-30 , 20] μm. Considering that the average diameter of the ink droplets printed from TIPS is calculated to be 54 μm, the average misalignment between ink droplets is relatively large. We also explore the drop placement accuracy of the PipeJet printer. The results are shown in Figure 2.17. We find that the misalignment

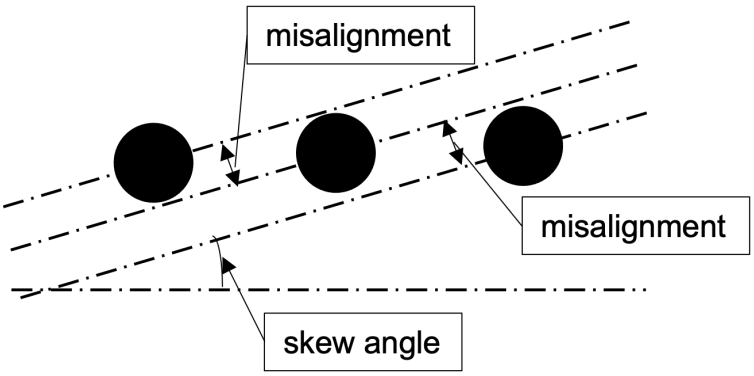

Figure 2.14. Skew estimation and misalignment measurement.

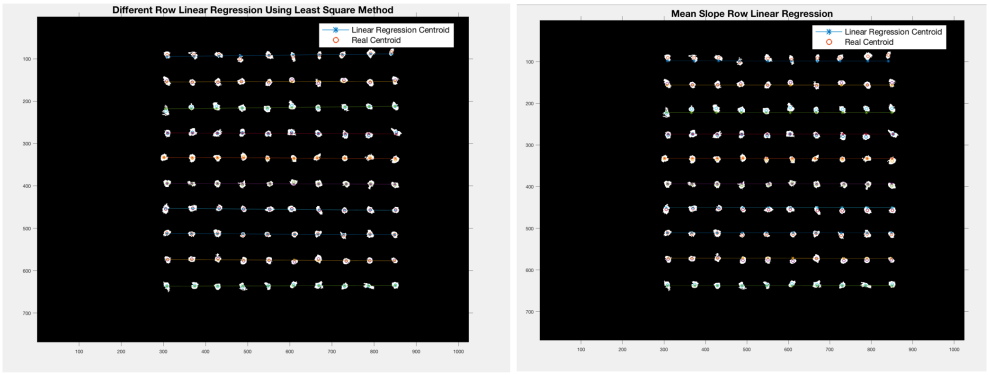

Figure 2.15. The orthogonal regression line of each row.

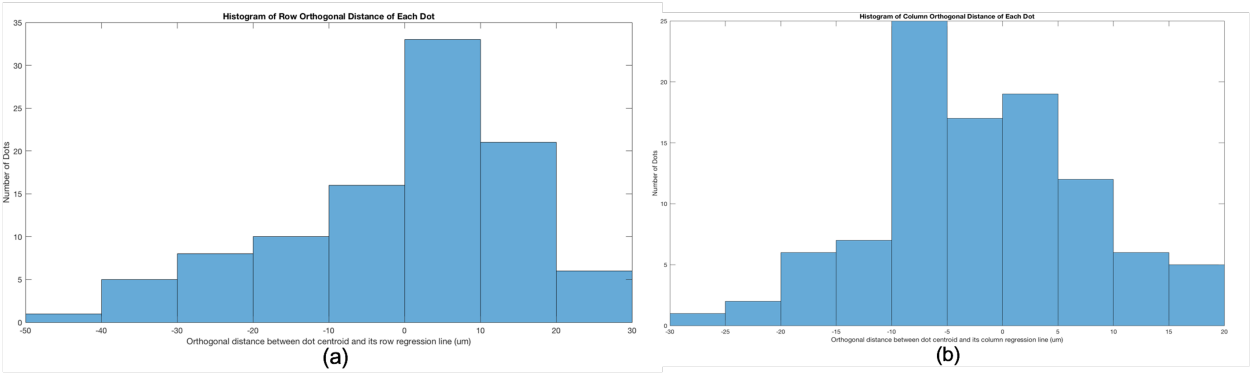

Figure 2.16. Misalignment results of each row and column (TIPS).

of most of the dots in the row and column directions is controlled in the range of [-50, 50] μm. The maximum value of misalignment of each column is 218.44 μm. Compared with the average drop size of 1004.10 μm, we can ignore the misalignment error. Therefore, from this

perspective, we believe that the PipeJet printer system is more qualified for our application.

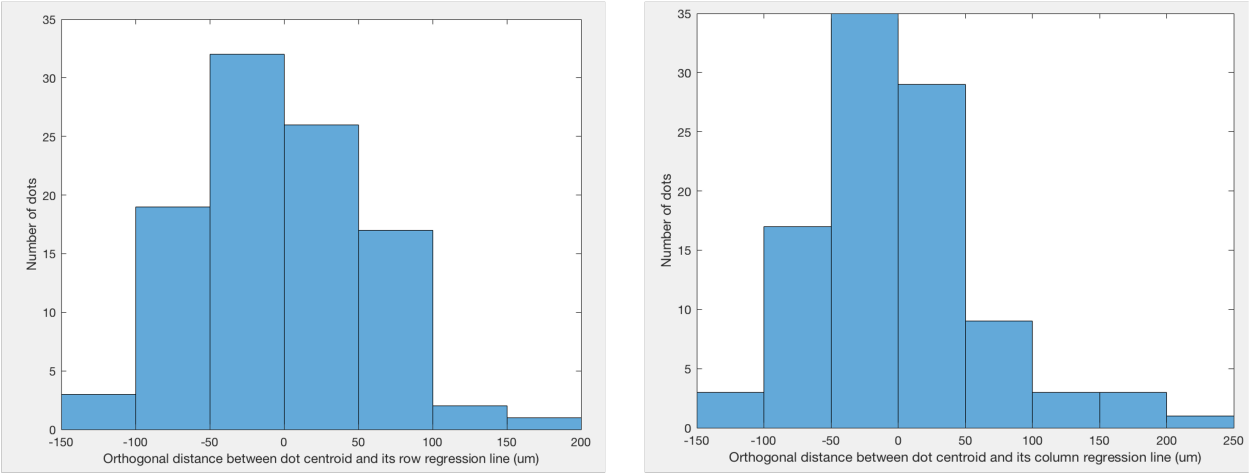

Figure 2.17. Misalignment results of each row and column (PipeJet printer).

Dot compactness

Another printing quality is the shape of printed dots [17]. The authors of the paper [17] use the compactness measure (δ) to quantitatively compare and assess the print quality of different stochastic clustered-dot halftoning methods.

The equation of the compactness is

$$\delta = \frac{A - 1}{\pi R^2} \tag{2.2}$$

where A is the area of the shape under consideration and R is the radius of the minimum enclosing circle of the shape.

Each printed dot is composed of many pixels. We treat each pixel as a point, and let the set P denote all the points in a printed dot.

1. We find the convex hull of all points in the set P, let the set Q denote points in the convex hull.

2. We pick three points from Q, and find the minimum enclosing circle S that contains those three points.

3. We calculate the distance d between every other point and the center of the circle S.

4. If the maximum of d is less than the radius of the circle S, that means every other point in Q is inside the above circle S, then we are done.

5. If not, pick the point which lies furthest from the center, and find the enclosing circle of those four points.

We repeat Steps 3 to 5 until no more points lie outside of the current minimum enclosing circle [18][19].

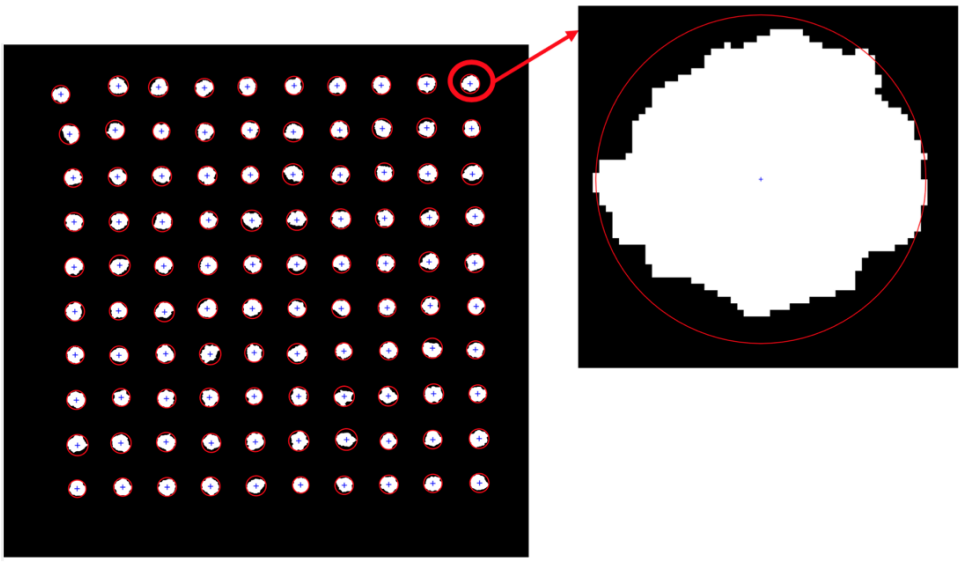

Figure 2.18. The image processing of dots printed with the PipeJet system (Stroke = 100% and stroke velocity = 50 um/ms).

To explore the compactness of the dots printed by the PipeJet system, we use the printed test pattern (10×10 dots) with different values of stroke and stroke velocity yielding no satellite to find enclosing circles of the printed dots. We notice that the circle passes through center of some pixels, and not all the pixels are enclosed in the circle, as illustrated in Figure 2.18. The reason is that we treat a pixel as a point, but actually the size of a pixel is 1 × 1. To solve this problem, we use subpixel interpolation to find the radius of the minimum enclosing circle, as illustrated in Figure 2.19.

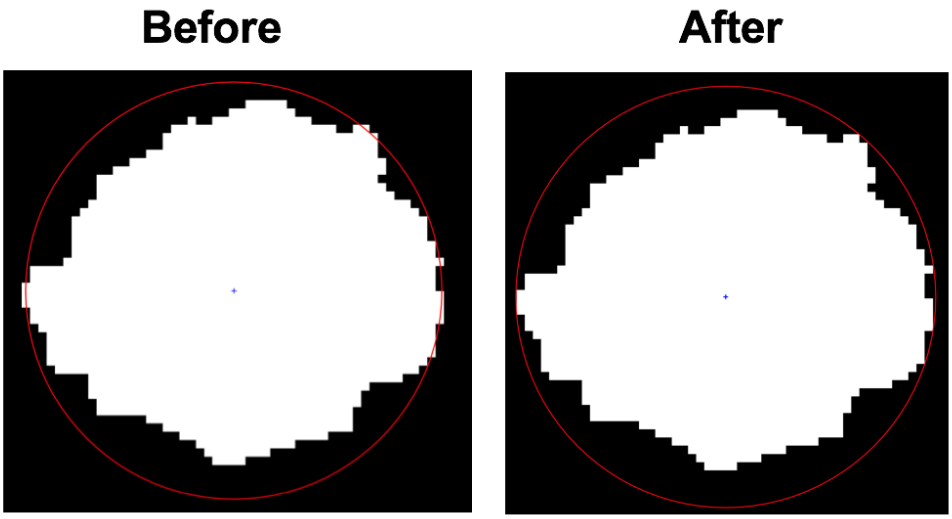

Figure 2.19. The improvement of the enclosing circles of dots printed with the PipeJet system (Stroke = 100 % and stroke velocity = 50 μm/ms).

We also validate our algorithm by comparing our calculated radius of the minimum enclosing circle of the given halftone dots in [17] with the radius given in the paper and conclude that they are very close.

The authors reported in [17] that the maximum compactness of the 24 dot clusters was 0.7. Table 2.1 shows the compactness of the dots printed with different values of stroke and stroke velocity yielding no satellite. The average compactness of the dots printed with different values of stroke and stroke velocity is about 0.7. So, we conclude that the PipeJet printer system produces high quality printed ink drops.

Table 2.1. Compactness of the printed test patterns.

Stroke Velocity (μm/ms)	100	100	100	80	80	80	50	50
Stroke	100	80	5	100	80	10	100	80
Compactness (δ)	0.699	0.696	0.693	0.724	0.715	0.730	0.719	0.720

2.4.4 Print mask design

According to the requirements of the printed volume and the size of each test or control line, we can design the print mask and the number of printing cycles for the test and the control line. The print head of a PipeJet printer consists of one nozzle which enables the printing patterns to be easily formed.

The number of the droplets in the horizontal (vertical) direction equals the length (width) of the test line divided by the average diameter of the dots, and the number of the printing cycles equals the total target printed volume of a test line divided by the total volume of a printing cycle. The calculation process is similar for a control line, except that the bio-inks are different.

Figure 2.20 shows the print mask, which consists of two print patterns to be applied to the test line. The optimized print mask provides better control of the printed DNA pattern. The numbers in the print mask represent the sequence of the print-head passes over the substrate. We spread out the drops to increase the time between the printing of adjacent pixels. Here is how we define a cycle (or a layer): print one pass of pattern A, then print one pass of pattern B. In our work, we print 15 cycles for the test line and the control line of each test strip. So, each pixel in the test line and the control line receives a total of 15 drops.

2.4.5 Bio-printing experiment and test results

For each test line and control line, pathogen capture arrays are printed using the printing system with the corresponding colorless bio-inks and the designed print patterns described above. To verify that the PTS is functioning, we apply Aptamer-based assay test technology to the PTSs to detect *E. coli* O157:H7 with different concentrations.

We describe the Aptamer-based assay test as follows: we add the Au-Ps particles (Gold decorated Polysterene) in a solution with *E. coli* O157:H7, then drop the mixed solution on the absorption pads (the end near to the test lines) of the PTSs [6]. The mixed solution will be drawn from the test zone to the control zone through capillary phenomena. After 20 minutes, two pink zones appear on each PTS. The test interpretation is described as follows:

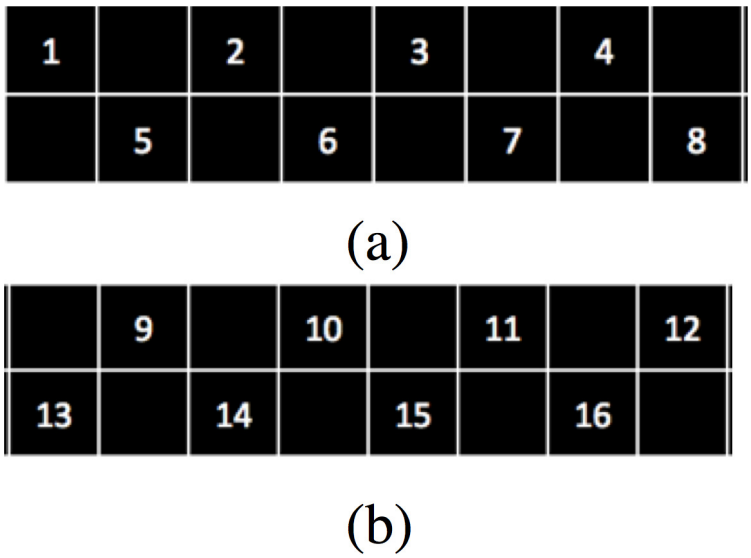

Figure 2.20. Print mask used to control the printing of a 4 mm × 1 mm line of DNA solution. The printing is done in two passes defined as a cycle, using pattern (a) and pattern (b), in sequence. Therefore, for a cycle, eight droplets are ejected in each row and two droplets are ejected in each column.

the pink test line in the test zone is used to confirm the presence of *E. coli* O157:H7, and the control lines are designed to confirm the functioning of the PTSs because the pink control line still appears when the mixed solution without *E. coli* O157:H7 reaches the control zone.

Figures 2.21(a) and (b) show the test results of the PTSs used to detect the concentration of *E. coli* O157:H7 with 0, $10^3, 10^4, 10^5$, and 10^6 CFU/ml, respectively. The visible responses in the control lines and test lines indicate that the PTS is able to sucessfully capture the *E. coli* O157:H7. To determine the detection limit, another ten PTSs are used to detect the concentration of *E. coli* O157:H7 with 10^2 CFU/ml. After doing the Aptamer-based assay test on these PTSs, the pink lines appeared on the test lines and the control lines, as illustrated in Figures 2.21(a) and (b). Therefore, we prove that our PTSs can capture *E. coli* O157:H7 with limits of detection down to 10^2 CFU/ml.

2.5 Image Analysis via A Cell Phone Camera

We propose an image analysis method to assess the responses by using a mobile phone camera. The metric that we used to characterize the responses in the test lines of the test

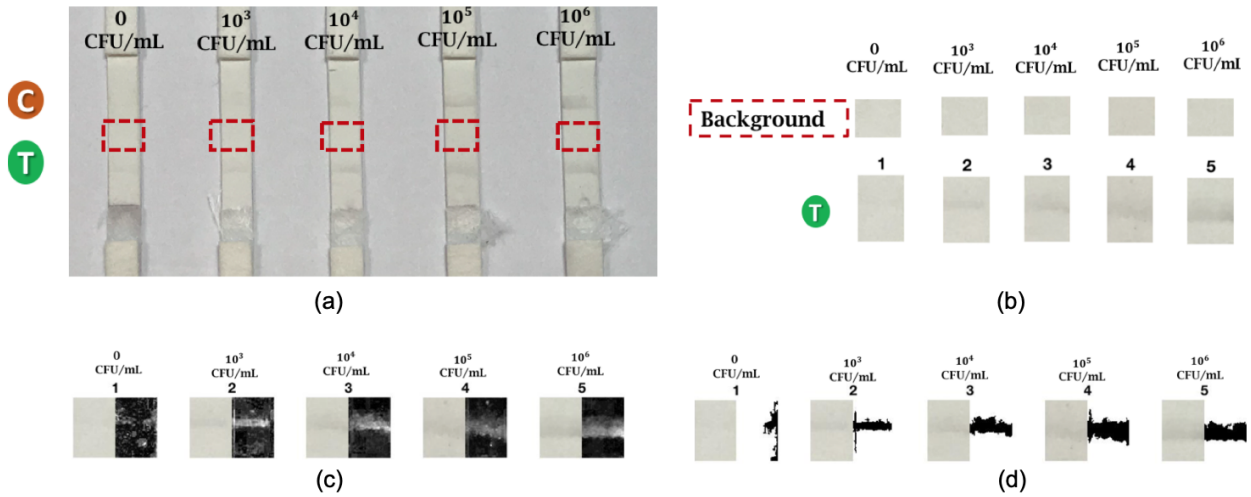

Figure 2.21. (a) The test results of the PTSs used to detect the different concentrations of *E. coli* O157:H7. The image is captured by a mobile phone (iPhone 7 Plus). (b) Cropped version of test zones and the local background of the test strips. (c) The original RGB images of the test zones and the corresponding grayscale images. (d) The original RGB images of the test zones and the final version of the corresponding binary images.

strips in this approach is the grayscale values, which is the sum of the CIE ΔE values of the test line. The image of the test strips was captured in a Macbeth SpectraLight II light booth (Gregtag Macbeth, New Windsor, NY, USA)) for providing a daylight environment with a mobile phone camera, as illustrated in Figure 2.21(a). The test zone images and the corresponding background images were cropped to 60 × 130, and 60 × 40 pixels, respectively, using Adobe Photoshop and saved in TIFF format without compression, as illustrated in Figure 2.21(b).

We transform the gamma-corrected sRGB values of these five images to linear RGB values according to Eq. (2.3) [20].

$$I_{linear} = \begin{cases} \frac{I_{sRGB}/255}{12.92}, & (I_{sRGB}) \leq 0.03928 \\ \left(\frac{I_{sRGB}/255+0.055}{1+0.055}\right)^{2.4}, & otherwise \end{cases} \tag{2.3}$$

Then, these linear RGB values are converted into CIE XYZ values in the matrix transformation step.

$$\begin{bmatrix} X \\ Y \\ Z \end{bmatrix} = \begin{bmatrix} 0.4124 & 0.3576 & 0.1805 \\ 0.2126 & 0.7151 & 0.0721 \\ 0.0193 & 0.1192 & 0.9505 \end{bmatrix} \begin{bmatrix} R_l \\ G_l \\ B_l \end{bmatrix}. \tag{2.4}$$

We then transform CIE XYZ to the CIE L* a* b* color space, which is a uniform color space.

$$\begin{aligned} L^* &= 116 \times f(\tfrac{Y}{Y_n}) - 16 \\ a^* &= 500 \times [f(\tfrac{X}{X_n}) - f(\tfrac{Y}{Y_n})] \\ b^* &= 200 \times [f(\tfrac{Y}{Y_n}) - f(\tfrac{Z}{Z_n})]. \end{aligned} \tag{2.5}$$

Here, $[X_n, Y_n, Z_n]$ is the reference white point, and $f(t)$ is given by

$$f(t) = \begin{cases} t^{\frac{1}{3}}, & t > \left(\frac{6}{29}\right)^3 \\ \frac{1}{3} \cdot \left(\frac{19}{6}\right)^2 t + \frac{4}{29}, & otherwise \end{cases} \tag{2.6}$$

To obtain the corresponding gray scale images, we compute the ΔE value from the background which is the color difference between the pixel values and the local background.

$$\Delta E = \sqrt{(L^* - L_{avg})^2 + (a^* - a_{avg})^2 + (b^* - b_{avg})^2}, \tag{2.7}$$

where $(L_{avg}, a_{avg}, b_{avg})$ are the average values from the local background. Then we normalize the ΔE values of the images to the range [0, 255] [21][22].

Figure 2.21(c) shows the original RGB images and the corresponding grayscale images. We use Otsu's method to get the initial binary images. To get the final version of the binary images, we use the 4-point connected component method to remove noise by calculating the area of each component and making sure that the pixel values of the largest area are 1, while the rest is 0. Figure 2.21(d) shows the original RGB images and the final version of the binary images. With the aid of the binary images, the location of the responses in the test lines can be defined. We use grayscale values as a metric, calculating the sum of ΔE

values of the test lines, to characterize the responses in the test lines. Figure 2.22 shows the relationship between the grayscale values and the concentration of *E. coli* O157:H7.

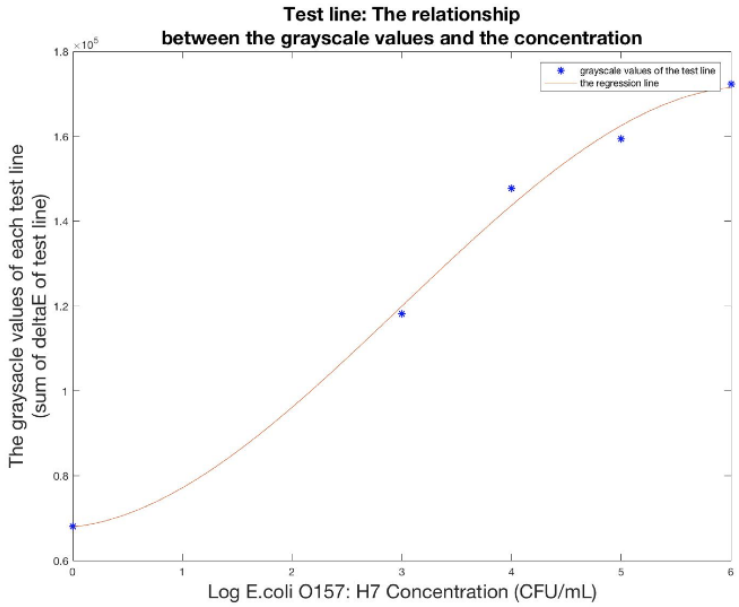

Figure 2.22. The plot of the cubic relationship between the grayscale values and the concentration of *E. coli* O157:H7 was found by applying the least-squares fitting method.

To assess the variation among the responses in test lines of test strips by correlating the color intensity under a fixed concentration of 10^2 CFU/ml, we do the same image analysis on the 10 test strips to obtain the grayscale images and the corresponding binary images, as illustrated in Figures 2.23(c) and 2.23(d). The color intensity on the test lines on different strips appears differently because of the variations in the mesh structure, the flow path, and the shape of the test strips. Figure 2.24 shows a plot of the variation among the responses of the test lines at the same concentration.

2.6 Conclusion

In this chapter, we propose a system for printing test strips to detect foodborne pathogens, and image processing algorithms to analyze images of the exposed test strip that have been captured with a mobile phone camera. The image processing algorithms are designed to detect the presence a pathogen, and to estimate its concentration. The overall goal of the

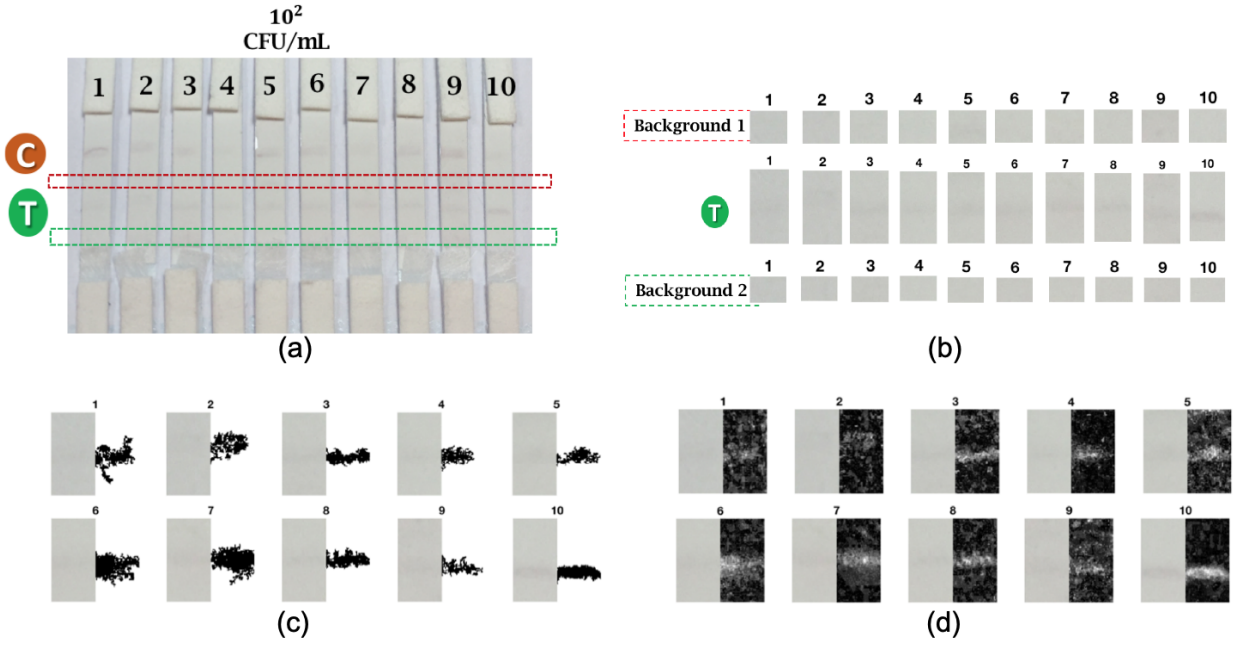

Figure 2.23. (a) Test results of PTSs used to detect *E. coli* O157:H7 with the concentration 10^2 CFU/ml. The image is captured by a mobile phone (iPhone 6 Plus). (b) Cropped version of test zones and two types of local background of the test strips. (c) The original RGB images of the test zones and the corresponding grayscale images. (d) The original RGB images of the test zones and the final version of the corresponding binary images.

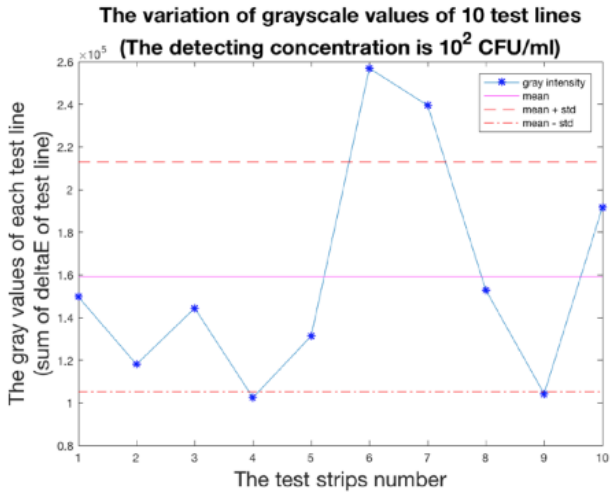

Figure 2.24. The plot of the variation of the grayscale values as a function of test strip number. The mean and standard deviation of the sum of ΔE values across the 10 test strips are 1.59×10^5 and 1.59×10^5, respectively.

project is to develop a test system that is low-cost, and simple enough to implement in the field. We believe that printing offers a manufacturing method that is low-cost, reliable, and scalable. To date we have worked only with *E. coli* O157:H7. But we believe that our framework could be applied to other food-borne pathogens, as well.

We show that the functioning PTS can detect the presence of foodborne pathogens; and we confirm an Aptamer-based assay detection limit of 10^2 CFU/ml. The relationship between the optical properties of the test lines and the different concentrations of the pathogen is also investigated. Further research can include the optimization of printing layers that can reduce material (bio-inks) cost and printing time, as well as an effort to reduce the sample-to-sample variation in the response to low concentrations of *E. coli* O157:H7.

3. DETECTION, IMAGING, AND QUANTIFICATION OF DNA-BASED PATHOGEN BASED ON INKJET-PRINTED TEST STRIPS

3.1 Introduction

The foodborne pathogen *E. coli* O157:H7 that produces toxins that damage the lining of the intestine, is a worldwide threat to public health. *E. coli* O157:H7 can be easily found in contaminated water and contaminated food, especially undercooked ground beef, milk and juice, raw fruits and vegetables. And, *E. coli* O157:H7 infections from contaminated food continue to occur regularly, and result in severe disease and even loss of life. Therefore, a fast, reliable, and affordable biosensor is more and more in demand. Many traditional lateral flow biosensors have been developed for foodborne pathogen detection. However, most of these are laboratory-based and cannot be manufactured economically. To address this problem, we incorporate printing and biomaterials technologies to design inkjet-printed test strips (PTSs) that guarantee rapid, affordable, reliable, and reproducible detection of the pathogens.

The detection result of biosensors can be determined by visual inspection or by a color measuring device. To have a quantitative and objective color analysis, color measuring instruments are more favored. As digital technologies continue to develop, cheap and compact image sensors are widely used in common electronics, like cell phones. The phone-based imaging system is promising for signal detection due to the above features, and also is emerging in different fields, such as high-resolution microscopy [23] and fluorescence imaging [24]. In our work, we propose a phone-based image processing algorithm to analyze images of the exposed test strip that have been captured with a mobile phone camera.

Overall, we develop the inkjet printing process for producing the pattern for the capture of *E. coli* O157:H7. The readouts of test results can be interpreted either by our image analysis system or by the naked human eye. We prove that our PTSs can successfully detect the presence of *E. coli* O157:H7 down to 10^2 CFU/ml [25].

One of the conditions that a successful biosensor must be meet is that the detection results show a low variation between assays. To measure response variations of our PTSs, ten independent experiments were performed for the same concentrations of *E. coli* O157:H7 test solution to obtain statistically reliable data by dropping the same amount of test solution onto the PTSs using a pipette. Figure 3.1 shows the color change in test zones for *E. coli* O157:H7 with the concentration 10^2 CFU/ml. The visible responses in the test zone and control zone indicate that the PTSs are able to successfully capture *E. coli* O157:H7 with a low concentration. Visually, we notice that the response of the test zones varies. The reasons are the following: (i) the random flow path of the reagents in the porous substrate (natural cellulose paper: Hi-flow HFC075, EMD Millipore); (ii) the extra amount of the bio-inks on the test zones increases the diffusion area; and (iii) the response intensity can be varied by using different segmentation methods. We optimize this problem in two aspects: the comparison of various image segmentation methods, and the optimization of the printing process in print layers that can reduce the sample-to-sample variation.

In this work, we propose two methods that reduce the response variation between assays. First, we review the various well-used image segmentation methods and apply them to detect the responses in the test lines of test strips. The usefulness of these segmentation methods is evaluated by comparing the response variance of the corresponding segmentation results. Second, we propose the optimization of the printing process, and obtain less response variation.

3.2 Image Segmentation Techniques

In order to quantify the response of detection results, a given phone-captured image needs to be appropriately segmented, so that the test zone can be separated from the background in the image. An example of phone-captured images is shown in Figure 3.1. The target region will consist of a contiguous region of pixel locations indicating low brightness. And the background consists of pixels that correspond to brighter or higher intensity pixels surrounding the target. However, there are some noisy black areas, such as scratches or black dots in the background, which increases the difficulty of segmentation. Preprocessing is required before

segmenting the test zones from the background. Based on the printing location of biomaterials, we crop the test zone containing detection information and background images, scale them to 60 × 130 and 60 × 50 pixels, respectively, using Adobe Photoshop, and save them in TIFF format without compression, as illustrated in Figure 3.2. Then, we transform the gamma-corrected sRGB values of the digital images to the $CIE\ L^*a^*b^*$ color space, which has a visually uniform distribution of colors and is closer to the human perception of color differences than is sRGB. After transformation, an image difference matrix ΔE of each test image is obtained by subtracting the test zone images from the corresponding background image matrix using Equation (3.1).

$$\Delta E = \sqrt{(L^* - L_{avg})^2 + (a^* - a_{avg})^2 + (b^* - b_{avg})^2} \tag{3.1}$$

where $(L_{avg}, a_{avg}, b_{avg})$ are the average values from the local background. Then, we normalize the ΔE values of the images to the range [0, 255].

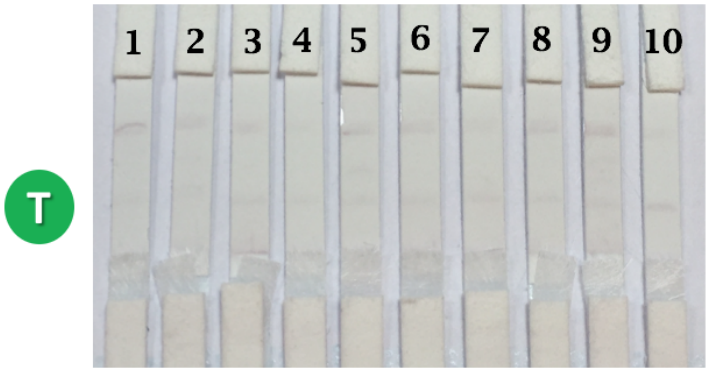

Figure 3.1. An image of test strips detecting the target at the concentration of 10^2 CFU/ml.

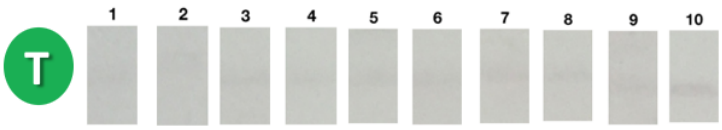

Figure 3.2. The crop of just the test region for each test strip.

Image segmentation is one of the most important steps of image processing, in which an image is subdivided into several regions with the aid of pixel information, such as color, intensity, and texture. A number of automatic segmentation methods have been developed [26][27][28]. It is observed that the segmentation result can directly affect the subsequent analysis, and there is not a best image segmentation method because different images have different characteristics. Here, we evaluate how well several existing segmentation techniques can determine the response signal in our PTSs when the boundary between the test zone and the background region is unclear. In particular, we use Otsu's method [16], the valley-emphasis method [29], the twice Otsu method, the histogram thresholding using hierarchical cluster analysis [30], multi-level thresholding [31][32], and a Support Vector Machine (SVM) method [33]. The usefulness of these segmentation methods is also evaluated in this chapter.

3.2.1 Otsu's method

Otsu's thresholding method is one of the best-known methods for automatic image segmentation [16]. Based on the histogram of a grayscale image, Otsu's method finds the optimal threshold t^* that maximizes the between-class variance $\sigma_B^2(t)$. The optimal threshold is expressed as follows:

$$t^* = ArgMax_{0 \leq t < L}\{\omega_1(t)\mu_1^2(t) + \omega_2(t)\mu_2^2(t)\} \tag{3.2}$$

where L is the number of distinct gray values ranging from 0 to L - 1, $\omega_1(t)$ and $\omega_2(t)$ are the probabilities of the two classes, and $\mu_1(t)$ $\mu_2(t)$ are the average gray values of the two classes. This method works well when the histogram has a strongly bimodal distribution. However, the segmentation result is poor when the histogram is close to an unimodal distribution, or when the background variance is large.

3.2.2 The valley-emphasis method

The valley-emphasis segmentation is a weighted Otsu's method. The idea of this method is to select the optimal threshold value corresponding to a grayscale value that has a small

probability of occurrence and also maximizes the between-class variance, as in Otsu's method [16]. The objective function of this method is expressed as:

$$t^* = ArgMax_{0 \leq t < L}\{(1 - p_t)(\omega_1(t)\mu_1^2(t) + \omega_2(t)\mu_2^2(t))\} \tag{3.3}$$

where p_t is probability of occurrence of the grayscale value corresponding to the threshold t [34].

3.2.3 The twice Otsu method

We can observe that the background variance is large for each image, so it is hard for a single threshold segmentation algorithm to effectively segment the target test zones from such kinds of background, as illustrated in Figure 3.3 O-7. It causes some of the background pixels to be classified as foreground pixels. To address this problem, we apply Otsu's method again to the segmented image after the first application of the single Otsu's threshold method. One of the examples that the segmented image after second application of single Otsu segmentation is shown in Figure 3.3 T-7, which is expected to remove extra background regions. This method is referred to as the twice Otsu method [31]. In our application, the criterion for an image to be treated with the twice Otsu method is that the ratio between the height and the width of the foreground should be higher than an empirically chosen threshold. We use 0.4 as the threshold in our application.

3.2.4 The histogram thresholding method

The histogram thresholding method using cluster analysis is adopted to segment images with overlapping intensity distributions. Initially, every non-empty gray level is regarded as a separate mode contained in a cluster. Then, the smallest distance pair is merged based on the computation of distance between adjacent clusters. The distance between the clusters C_{k1} and C_{k2} is defined as

$$Dist(C_{k1}, C_{k2}) = \sigma_I^2(C_{k1} \cup C_{k2})\sigma_A^2(C_{k1} \cup C_{k2}) \tag{3.4}$$

where $\sigma_I^2(C_{k1} \cup C_{k2})$ and $\sigma_A^2(C_{k1} \cup C_{k2})$ are inter-class variance and intra-class variance, respectively. $\sigma_I^2(C_{k1} \cup C_{k2})$ is the sum of the squared distances between the means of the two clusters and the total mean of both clusters. And $\sigma_A^2(C_{k1} \cup C_{k2})$ is the variance of all pixel values in the merged cluster [29].

The optimal threshold for the m-level thresholding is obtained by iterating the previous process until m groups of gray levels are obtained. For the two-level thresholding, we obtain two clusters, C_1 and C_2, and the estimated threshold T_1, which is the highest gray level of the background.

3.2.5 The multilevel thresholding method

There is another multilevel segmentation method that is an extension of Otsu's method, called the multilevel thresholding method [32]. Assume there are m thresholds, $(t_1,\ldots,t_m)$ dividing the image into m classes. Then, the optimal thresholds can be determined by the following equations:

$$\begin{aligned} Maximize\ J(t) &= \sigma_0 + \sigma_1 + \sigma_2 + \ldots + \sigma_m \\ where\ \sigma_0 &= \omega_0(\mu_0 - \mu_T)^2 \\ \sigma_1 &= \omega_1(\mu_1 - \mu_T)^2 \\ \sigma_2 &= \omega_2(\mu_2 - \mu_T)^2 \quad \ldots \\ \sigma_m &= \omega_m(\mu_m - \mu_T)^2 \end{aligned} \tag{3.5}$$

where σ_0, ..., σ_m, ω_0, ..., ω_m, and μ_0, ..., μ_m, μ_T are the variance, the probability, the mean intensity of each class, and the mean intensity for the whole image, respectively. Each of the grayscale images in Figure 3.3 is divided into three classes with three optimal thresholds t_1, t_2, and t_3.

3.2.6 Support vector machine classifier

The support vector machine method [33] is a supervised machine learning algorithm that has been applied to numerous classification problems. The key idea is to find the optimal

hyperplane to separate two classes. The optimal hyperplane has a maximum margin between it and the nearest data points of both classes, termed Support Vectors. From our image data, we can observe that the grayscale values of the brightest pixels from the target are much closer to or a little larger than the grayscale values of the darkest pixels from the background. Therefore, due to overlapping intensity distributions and unclear boundaries, we choose the soft margin SVM algorithm [35] to apply to non-separable data. The training dataset is defined as $(x_\mathrm{i}, y_\mathrm{i})$, i = 1, ..., n where x_i is the training sample and $y_\mathrm{i} \in \{-1, +1\}$ is the class label. The objective function is the dual representation of the maximum margin problem:

$$\begin{aligned} L_D(\alpha) &= -\sum_{\mathrm{ij}} \alpha_\mathrm{i}\alpha_\mathrm{j}t_\mathrm{i}t_\mathrm{j}x_\mathrm{i}x_\mathrm{j} \\ subject \quad to \quad & 0 \leq \alpha_\mathrm{i} \leq C \\ & \sum_{\mathrm{i}} \alpha_\mathrm{i}t_\mathrm{i} = 0 \end{aligned} \tag{3.6}$$

where the parameter C controls the trade-off between the training error and the margin, and the α_i's are the Lagrange multipliers. The optimal hyperplane is given by:

$$\begin{aligned} f(x) &= w^T x + b \\ where \quad w &= \sum_{\mathrm{i}} \alpha_\mathrm{i}t_\mathrm{i}x_\mathrm{i} \end{aligned} \tag{3.7}$$

Here, w is the surface normal to the hyperplane, and $\|b\|/\|w\|$ represents the perpendicular distance between the hyperplane and the origin. The features adopted for classification in this work consist of normalized values of the grayscale images, and the $CIE\ L^*a^*b^*$ values at each pixel position. Drawing on the training experience of medical image processing [35][36], we employ a subject-specific training scenario. The golden standard segmentation results of the training images are obtained by manual segmentation based on the results from the multilevel thresholding method and morphological operations. The ten images used as the training set consist of 10,000 test zones data samples and 20,000 background data samples.

3.2.7 Data analysis

Figure 3.3 shows the final versions of binary results using the above six segmentation methods combined with a 4-point connected component method. It can be seen that the segmentation results of Otsu's and the valley-emphasis methods are very close, and they can detect the presence of test zones. However, when the images have poor signal-to-noise ratio, neither method can precisely segment the test zone, as illustrated in Figures 3.3 O-7 and V-7. The twice Otsu method can extract the refined test zone from the background. For most images, the histogram thresholding method mainly segments a significant part of the test zone with larger grayscale values, but this can cause information loss, as illustrated in Figure 3.3 H-5. Compared with the SVM method, the detection results of the multilevel

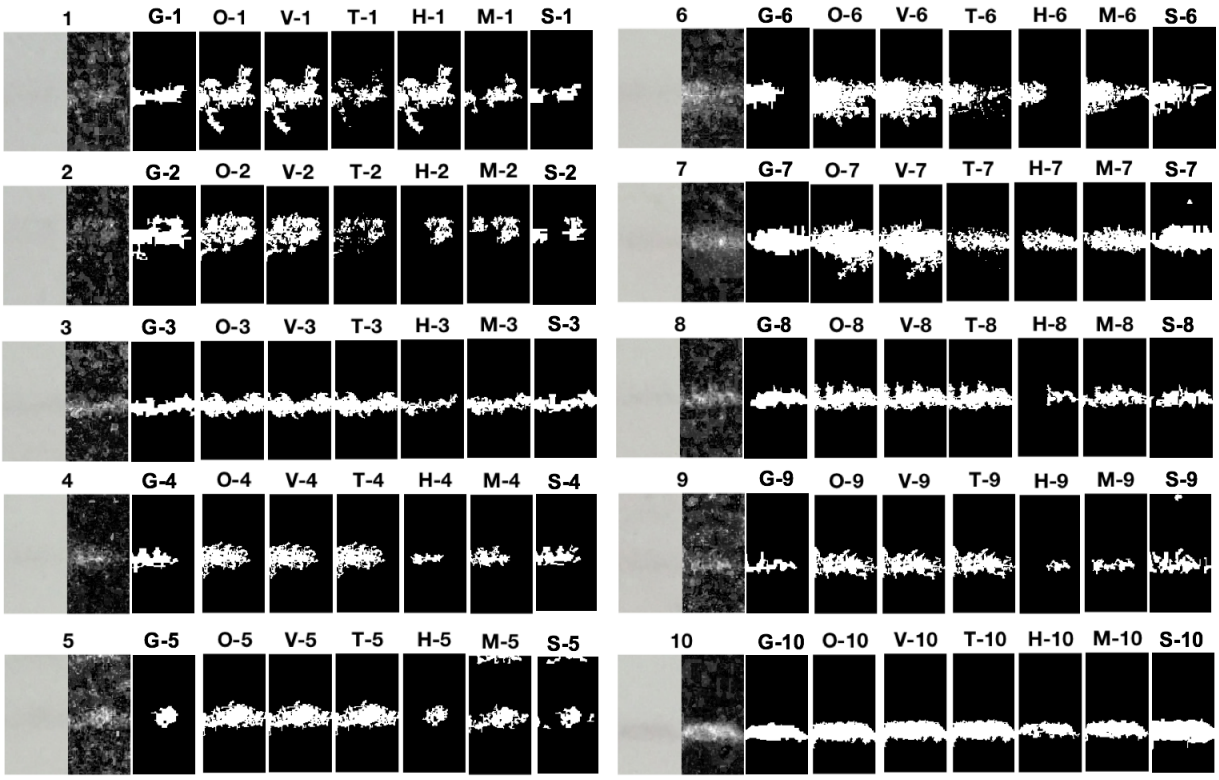

Figure 3.3. The original images, grayscale images, and segmentation results for test images by the selected methods. (G, O, V, T, H, M, and S represent the abbreviation of the ground truth segmentation result, Otsu's method, valley-emphasis method, twice-Otsu method, histogram thresholding method, multi threshholding, and SVM, respectively.)

thresholding method are more refined. The segmentation results of the SVM method are mostly determined by the training data. For example, a training set with a low brightness contrast between the target origin and the background leads to a classifier that has a greater probability of confusing overlapping intensities of foregrounds and backgrounds, as illustrated in Figure 3.3 S-10. The segmentation results indicate that the multilevel thresholding method will extract the relatively bright region in the grayscale image.

To assess the variation among the responses in the test lines, we use the sum of ΔE from the detected region as the metric to quantify the visual response. Figure 3.4 shows graphs of the variations of the grayscale values for each test strip based on the metric and the selected segmentation methods. When analyzing the variation in the response results of the Otsu's method, the valley-emphasis method, and the multilevel thresholding method, we observe that the data of these three plots follow the same trend since they are all related to Otsu's method. For the first two methods, 70% of the data is located in the area comprising the mean $\pm$ 1 SD (Standard Deviation), while the response of the multilevel thresholding result varies greatly. 70% of the data values from the twice Otsu method are also located in the area comprising the mean $\pm$ 1 SD, while they are more concentrated more closely near the mean. The variation result of the histogram thresholding method shows that 60% of the data is distributed in the mean $\pm$ 1 SD. More data values spread out from the mean in the histogram thresholding method because of the incomplete extracted pattern. Although the binary results of the multilevel threshold method are better, its response variation is large. The plot of the SVM method shows that 80% of the data is located in the mean $\pm$ 1 SD. We measure the variation among the responses as the percentage of total data distributed in the interval of the mean $\pm$ 1 SD. We can then note that the SVM method yields the highest percentage of total data distributed in the mean $\pm$ 1 SD interval. Overall, we conclude that the SVM method can segment test zones quite accurately and presents less variation of color response in the test zones.

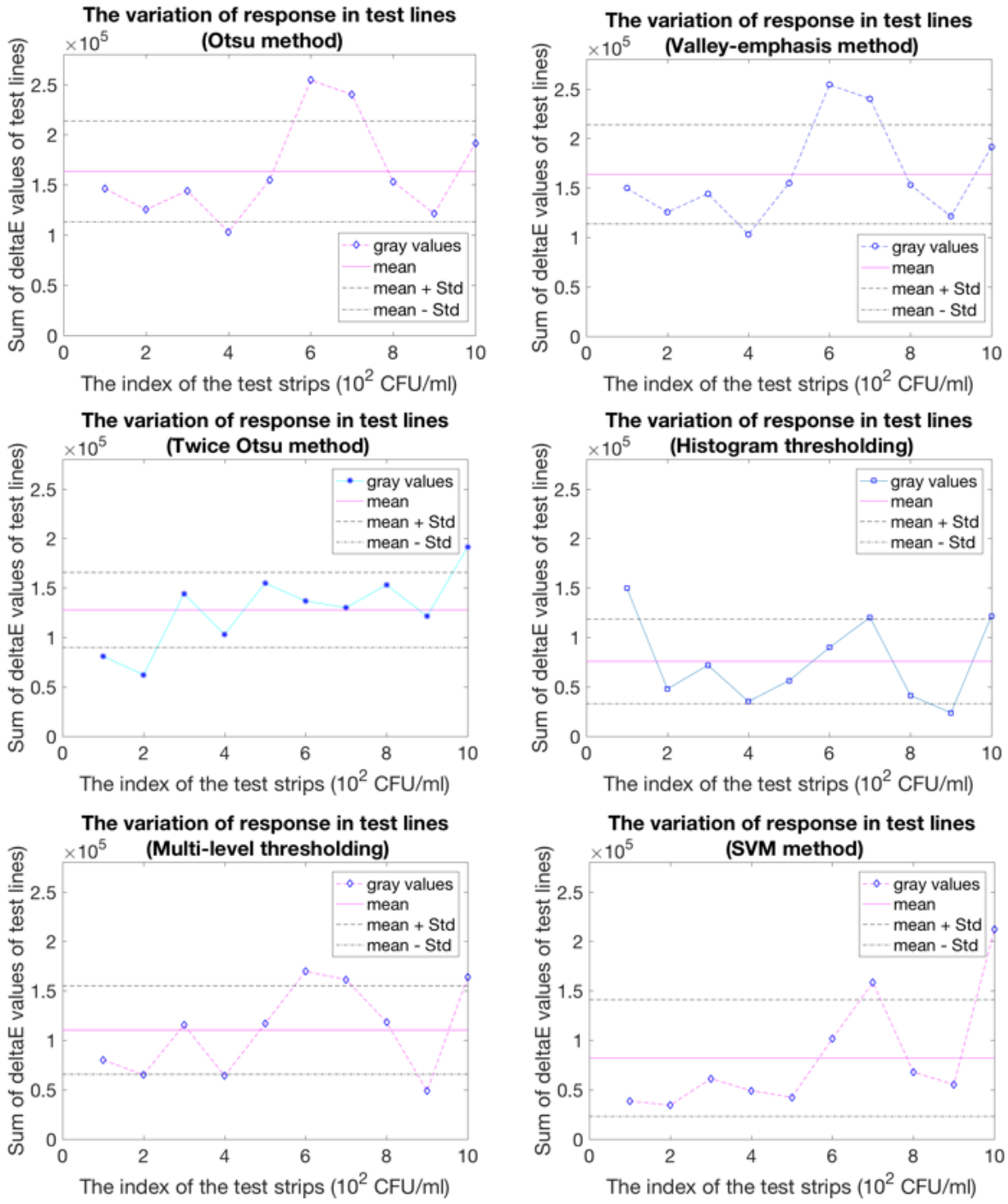

Figure 3.4. The plots of the variation of the grayscale values as a function of the index of test strips for the different segmentation methods.

3.3 The Optimization of the Printing Process

The extra amounts of bio-inks printed on substrates increases the diffusion areas of the test lines. To address this problem, we optimize the print layers for test lines and control lines in the test strips. To find the optimal print number of layers of drop deposition, it is advantageous to observe the color change in test strips based on the different numbers of print layers. Here we use the checkerboard print mask [25] which has been previously shown to provide better control of the printed DNA pattern.

Figure 3.5 shows the image of the response signal in the test strips with varying numbers of print layers (from 4 to 9 layers) captured by a mobile phone camera. For the target concentration at 10^3 CFU/ml, we notice that we could observe a visible color change on the test strips printed with 9 layers compared with other numbers of print layers. Since we wish to minimize the number of print layers, we chose 9 layers as the optimal minimum number of layers to print the solution on the test strip.

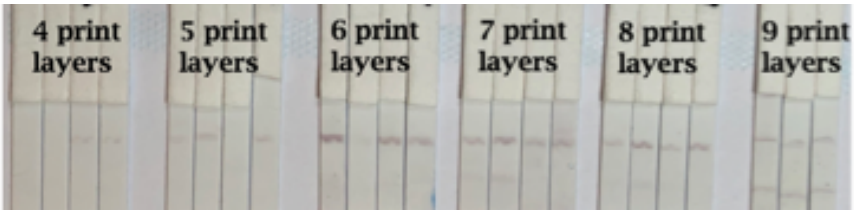

Figure 3.5. An image of the response signal in the test strips with varying numbers of print layers captured by a mobile phone camera.

3.4 Conclusion

The response variation of the optical properties of the test lines detecting the target at the same concentration is investigated. To reduce the sample-to-sample variation in response to *E. coli* O157:H7, as well as an effort to reduce material cost and printing time, we optimize the numbers of print layers. An analysis of the response variation using various image segmentation methods has also been given. We evaluate selected thresholding methods for test zone images with the extracted patterns. And one example with ten samples has been provided to show the comparison of the response variations using these methods. We observe

that the proposed SVM method has the least response variance. Also, we show that there is a less sample-to-sample variation of response signals in the test strips with the optimal set of printing layers.

4. PRINTING SYSTEM AND TRADITIONAL IMAGE ANALYSIS MODEL FOR HEAVY METAL DETECTION

4.1 Introduction

Nowadays, safety in food becomes critical. The main two types of threats related to food safety are foodborne pathogens and heavy metals [37][38]. One of the most common foodborne pathogens that can be found in our daily food is *E. coli* O157:H7. It can produce toxins that damage the lining of the intestine, cause bloody diarrhea, and sometimes result in kidney failure and even death. Human infections with *E. coli* O157:H7 are associated with the consumption of contaminated water and contaminated food, especially undercooked ground beef, milk and juice, raw fruits and vegetables. Moreover, such infections continue to occur regularly and result in severe disease and even loss of life. Therefore, it is crucial to develop an affordable, rapid, and simple method for detecting *E. coli* O157:H7.

To date, the widely used pathogen detections methods include culture-based counting, polymerase chain reaction (PCR), and enzyme-linked immunosorbent assay (ELISA). Among these methods, a plate culture takes 2-3 days to identify the suspected pathogens, and PCR involves laborious procedures. ELISA, which offers rapid detection, precision, high throughput, and low cost has attracted considerable interest; and it has a low detection limit of 10^4 CFU/mL [39]. To further push the limit of detection, our group incorporated printing and biomaterials technologies to develop inkjet printing lateral flow test strips for aptamer-based pathogen detection, and designed an image analysis method to characterize and quantify the response in the biosensors to statistically prove that the detection limit of our biosensor is 10^2CFU/mL [40][25].

Beyond the foodborne pathogen *E. coli* O157:H7, we notice that the presence of heavy metals in food chains also poses a threat to public health. Heavy metals, including Mercury (Hg), Arsenic (As), Copper (Cu), and so on can be enriched in living tissue through food chains and have been proven harmful to human health at low concentrations. Currently, heavy metal detection methods used are Mass spectroscopy, Atomic Emission Spectroscopy, Potentiometric Methods, and so on [41][42][43][44]. These methods are sensitive but expensive and require expensive equipment, trained personnel and cannot support on-site detec-

tion. Therefore, rapid detection methods for heavy metal pollutants are more and more in demand.

During the last few decades, a wide variety of microfluidic paper-based biosensors have been successfully developed, demonstrating powerful tools for detecting food and environmental contamination [45][46]. Microfluidic paper-based analytic devices (μPADs), developed in 2007 by Whiteside's team, have the characteristic of controlling a fluid motion via capillary force through specially designed microfluidic channel patterns on cellulose paper. As the major component of μPADs, cellulose papers with flexible porous fiber structure can wick liquids in small volumes without the need for external pumping equipment. The major task in the fabrication of μPADs is to create well-defined, millimeter-sized dimensional channels, comprising hydrophilic paper bounded by hydrophobic materials (wax or UV-curable inks) on cellulose papers. The heavy metals can be detected by gold nanoparticles (AuNPs) usually preloaded in reaction zones by providing colorimetric signals in biosensors. The colorimetric signals in the detection zones are commonly collected using a professional digital camera or a high-resolution scanner. Then, the color intensity of the signal in the captured images will be analyzed by some open source software. Unsurprisingly, μPADs have gained great attention due to their ease of use, low cost, amenability to colorimetric detection, and little test sample consumption.

To detect multiple targets in one test, which is hard to achieve with traditional lateral flow strips, our group focuses on developing a novel paper-based biosensor for colorimetric detection of two types of heavy metals: As and Hg. In this work, we first present paper-based devices fabricated by different technologies –different materials used to pattern hydrophobic walls across chromatography paper. Second, we propose preliminary patterns for multiple and multiplexed detection. Then, we detect the heavy metals at different concentrations to validate our approach. Finally, our optical system and image analysis pipeline guarantee to obtain consistent data acquisition captured by a mobile phone camera, and deliver quantitative responses to correlate the colorimetric change of the biosensors to the concentration of the target substance.

4.2 Experimental Details

The major task in fabrication of μPADs is to create well-defined microfluidic channels, comprising hydrophilic paper bounded by hydrophobic materials. Among the available manufacturing technologies in the market, three techniques that are mainly employed are inkjet printing, wax screen printing, and UV-curable ink screen printing [47][48][49].

4.2.1 Manufacturing methods

To compare the different manufacturing methods, we pattern the paper with some materials (like wax, or UV-curable inks) to form the hydrophobic boundaries on hydrophilic paper in three different ways: (i) inkjet printing with UV-curable ink, (ii) wax screen printing, (iii) UV-curable ink screen printing.

4.2.2 Inkjet printing with UV-curable ink

To precisely control the amount of UV-curable inks, a piezoelectric inkjet printer PipeJet (BioFluidiX, Freiburg, Germany) with deposition of single droplets in the range of 2 - 70 nL is used to print UV-curable inks onto the substrates, as is illustrated in Figure 4.1.

The hydrophobic wall is then generated by a UV lamp illuminating the printed UV-curable ink on the filter paper. Meanwhile, the unprinted regions retain their hydrophilic properties. We notice that the actual channel width is much smaller than the nominal width after the printing due to the long printing time; and the fact that the solvent of the UV-curable ink spreads faster than the pigment, as illustrated in Figure 4.5(a). Here, the pigment defines a channel of width 4.5 mm, whereas the channel defined by the spread of the solvent is only 1.5 mm wide.

4.2.3 Wax screen printing

Screen printing is a well-known, simple, low-cost, and reproducible technique used for printing designed patterns on clothing and other materials. For screen printing, the ink is rubbed through the screen stencil to the substrate to form hydrophobic barriers. The

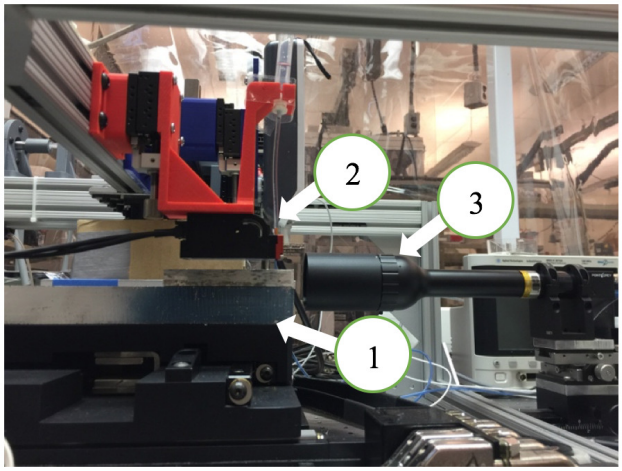

Figure 4.1. Inkjet system includes: (1) An XY motorized stage, (2) A PipeJet printer, (3) An optical system.

fabrication steps of the screen stencil for screen printing are shown in Figure 4.2. To make a stencil, we first apply specific emulsion coatings into the screen and put the mask above it under a UV light to be cured, thereby the meshes under the transparent area of the mask will be filled by the cured emulsion coatings. In contrast, the emulsion coatings under the black area of the mask will be rinsed off, as shown in Figures 4.2(c), 4.2(d), and 4.2(e). Therefore, black areas of the mask can generate a hydrophobic area on the substrate.

For wax screen printing, the wax is rubbed through the screen stencil with a squeegee to the filter paper. The printed paper is then heat-treated at 100 °C for 45 seconds; so that the wax can melt and spread vertically and laterally into the paper to form hydrophobic wax barriers. Finally, the printed paper is cooled to room temperature.

Since the melted wax also laterally spreads, which can impact the final pattern dimensions, we study the relationship between the printing and the resulting width after melting the wax. To evaluate this and the smallest hydrophobic barrier width, we generate patterns with constant whole length and widths but varying the middle edges from 1 mm to 2 mm with an increment of 0.2 mm, as illustrated in Figures 4.2(a) and 4.2(b). Here, a 110 mesh nylon is considered. We drop the red food dye onto the hydrophilic substrate to increase the color difference between the background and the white wax, so that the white wax can be easily separated from the background in the image by applying Otsu's method. We capture

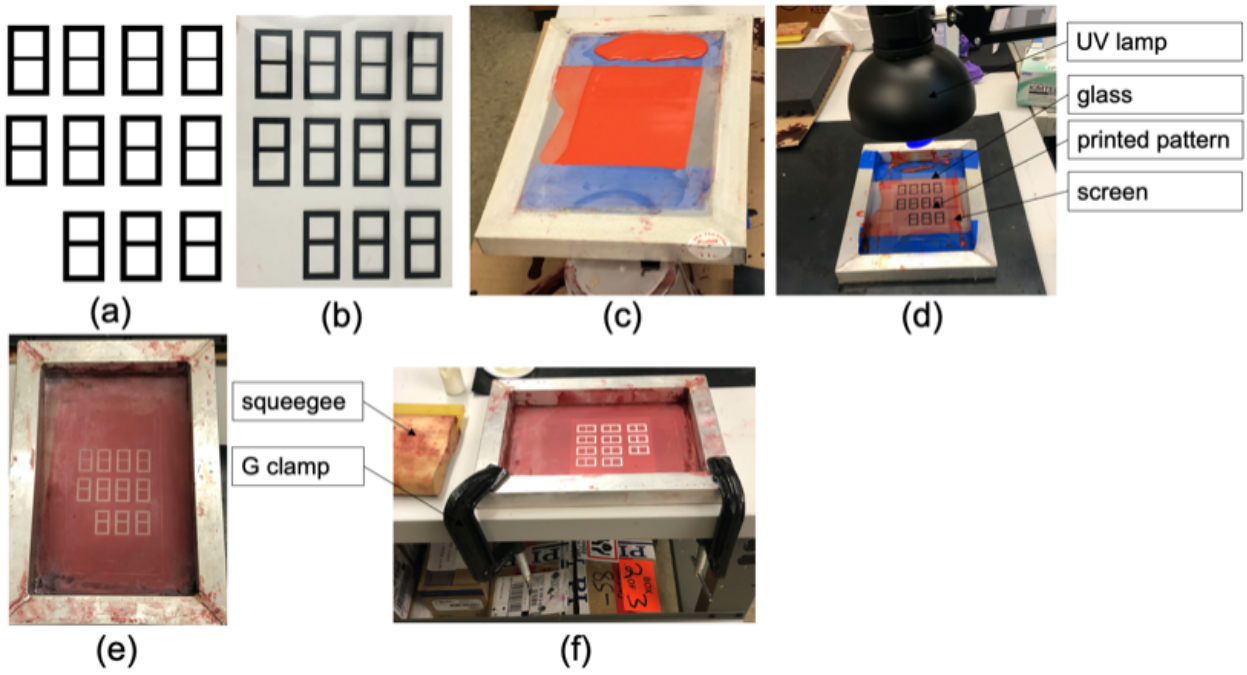

Figure 4.2. Fabrication steps of making a stencil for screen printing method: (a) a digital pattern, (b) the digital design is printed in a transparent film with a laser printer, (c) a screen is coated with an orange emulsion which is light sensitive, (d) the printed pattern is pressed against the screen and exposed to UV-light to harden the emulsion, (e) after washing the screen, a stencil of the digital design is created, (f) a substrate is placed under the screen, which is fixed with two G clamps, and inks can be rubbed through the mesh of the white areas onto the substrate by a squeegee.

the images of the samples using a QEA PIAS-II (QEA, Inc., Billerica, MA, USA) camera with resolution 1080.5 dpi and a field of view of 24.07 mm $\times$ 18.05 mm. An example of the image is shown in Figure 4.3(b).

Given an image containing a rotated pattern at an unknown angle, we can correct its skew in the following steps: (i) find the edge using the Canny method, (ii) calculate its convex hull and the minimum bounding rectangle (the red box in Figure 4.3(d)), (iii) rotate the image based on the slope of one side of the rectangle to correct for the skew. After correcting for the skew, we extract the edge of the middle barrier and calculate the average width by performing a vertical projection to record the distance between the left and the right position of each row. Then the average values of these distances are calculated as the average width of the middle barrier. To measure the width variations, three independent experiments are

performed to obtain statistically reliable data. Figure 4.3(e) shows the relationship between the printing and the resulting width after melting the wax.

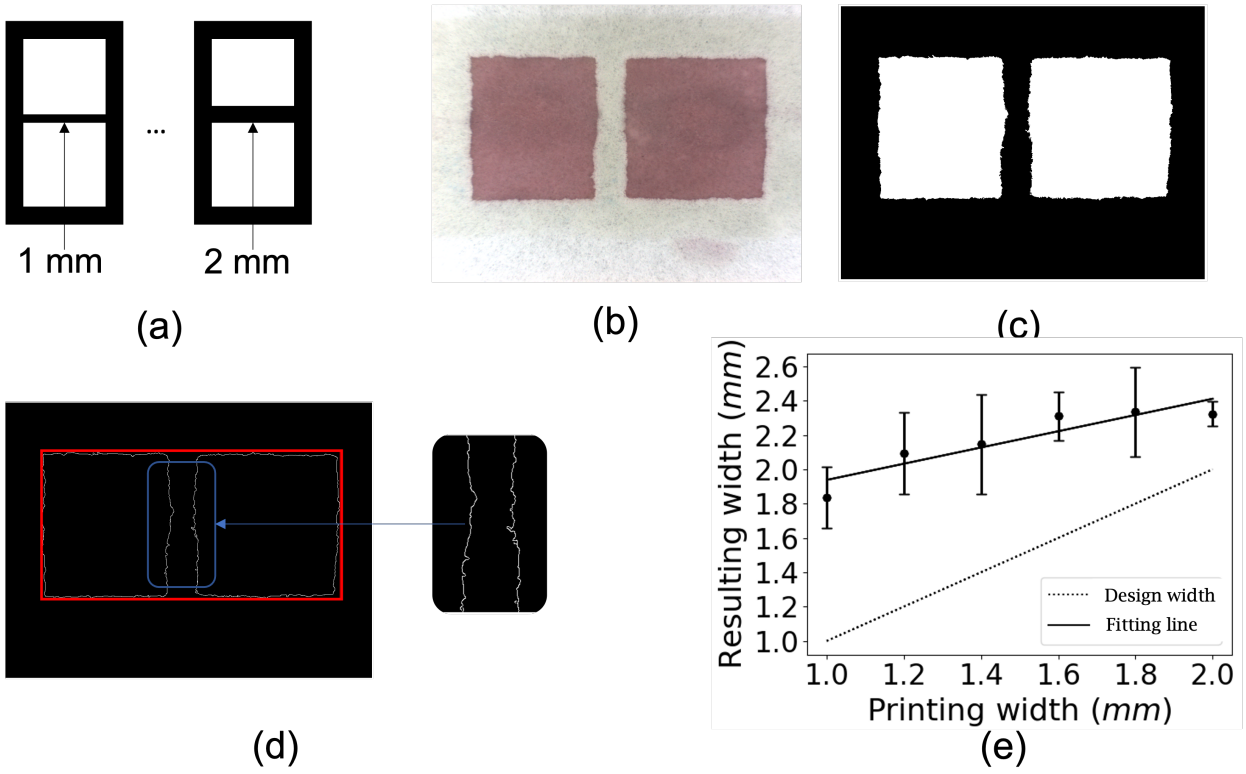

Figure 4.3. The relationship between the resulting width after melting the wax and the wax's printed width in front of the substrates: (a) digital patterns, (b) sRGB image captured by a QEA PIAS camera, (c) binary image, (d) correction for the skew, (e) result of statistical fit between the resulting width and the printing width.

As seen from Figure 4.3(e), the relationship between the printing width and the resulting width can be fitted as $y = 0.47x + 1.46$, with a coefficient of determination (R^2) 0.8373, thus showing a reasonably linear relationship. Each error bar represents the standard deviation of the corresponding three independent experiments. In addition, the resulting width may be affected by the different materials of the solid wax, the different mesh sizes, and the varying force pushing the ink through the screen. Therefore, it is anticipated that the fitting line will vary for the different printing parameters. To explore the hydrophobicity of the printed middle barrier, we print the digital patterns in Figure 4.3(a) and place them in the food dye solution to find the minimum barrier width that could be hydrophobic. We determine that

the minimum hydrophobic barrier that can prevent the food dye solution penetration is 1.5 mm. Figure 4.4(a) shows an example of the hydrophobic barriers printed with wax.

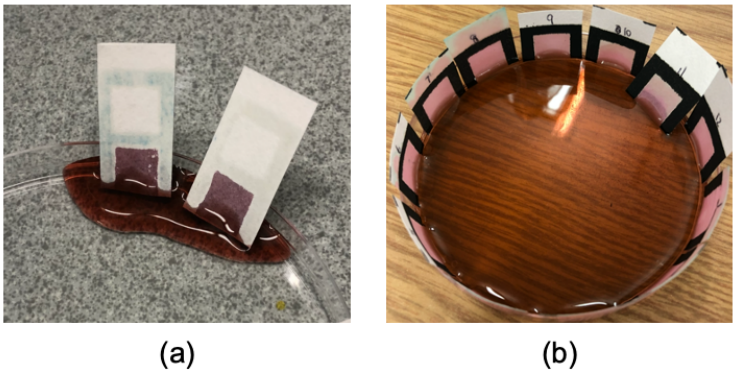

Figure 4.4. (a) An example of the hydrophobic property of the barriers patterned with wax screen printing. (b) Hydrophobic testing of the barrier patterned with UV-curable ink screen printing.

Figure 4.3(b) and Figure 4.5(b) show that the wax spreads unevenly after heating on a hot plate, therefore causing low-resolution printing. Based on this observation, we did not further explore how the mesh size and the different materials of the wax affect the resulting width after melting the wax.

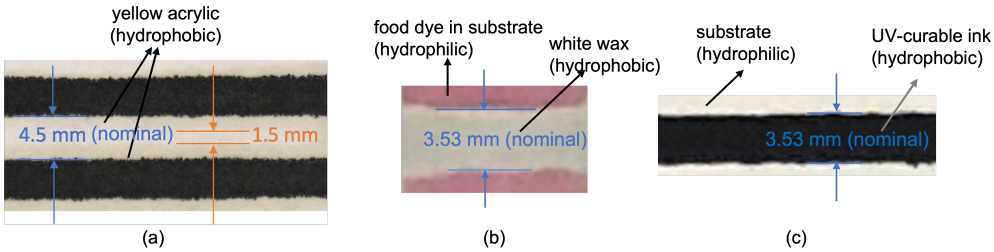

Figure 4.5. Results of three fabrication methods: (a) inkjet printing, (b) wax screen printing, (c) UV-curable ink screen printing.

4.2.4 UV-curable ink screen printing

For UV-curable ink screen printing, the UV-curable inks are rubbed using a squeegee, and then the screened paper is cured under a UV light to create the hydrophobic barriers on the filter paper.

The mesh size of the screen can affect the ink volumes, which further affects the printed result. To determine the resolution of our UV-curable screen printing method, we study the final width of the hydrophobic wall in the different screen mesh sizes. Here, screen frames with 110, 230, and 330 mesh nylons (Victory Factory, NY, USA) are considered. The numbers 110, 230 and 330 refer to the mesh count per cm.

Commercial screen-printing UV-curable inks are not suitable for patterning hydrophobic barriers on filter paper because their viscosity is too high to fully penetrate the substrates. To find the UV-curable inks' optimal penetrating ability, we prepare different proportions of pure UV-curable inks (Ultra Switch UVSW180, Maribu, Barcelona, Spain) and Thinner (UVV6 Thinner, Maribu, Barcelona, Spain) used to lower the ink viscosity for the experiments. Here, a pure UV-curable ink, one portion of UVSW 180 mixed with one portion of UVV6 Thinner (1:1), two portions of UVSW 180 mixed with one portion of UVV6 Thinner (2:1), and three portions of UVSW 180 mixed with one portion of UVV6 Thinner (3:1) are considered.

For each mesh size, we study the relationship between the resulting width and the nominal printing width of four types of inks. To evaluate this and the smallest hydrophobic barrier width, we design the patterns with varying widths from 1 pixel to 12 pixels (1 pixel = 0.353 mm), as shown in Figure 4.6(a). Figures 4.6(b) and 4.6(c) show the front and the back of the printing using the pure UV-curable inks. To measure the width variations, three independent experiments are performed. We use the same image analysis pipeline as the wax-screen printing to calculate the average widths of the middle barries of the UV-curable inks. Figures 4.7(a), 4.7(b), and 4.7(c) show the plots of the resulting widths in front versus the nominal printing widths of four kinds of inks. For each type of screen, the resulting widths are linearly fitted with the nominal printing width, with R^2 ranging from 0.9934 to 0.9995, thus showing an excellent linear relationship for each type of ink. The error bars represent the standard deviation of each three independent experiments. The relative standard deviations of the barrier printed by 3:1 inks are less than 13%, which shows evidence of the controlled widths and acceptable reproducibility. Besides, the printed middle barriers of 3:1 inks maintain better penetrability to yield a good hydrophobic ability. Thus, we conclude that the 3:1 inks are the optimal ink mixture for our UV-curable ink screen printing. To explore the hydrophobicity of the printed barrier, we place the printed

patterns in a red dye solution to find the minimum barrier width that could be hydrophobic. As seen in Figure 4.4(b), starting from the 9th sample, no pink solution passes through the intermediate barrier near the top of the test strip. The nominal width of the middle barrier for the 9th sample is 9 pixels (1 pixel = 0.353 mm), which corresponds to 3.17 mm. Therefore, we conclude that the smallest nominal hydrophobic barrier of 3:1 inks is 9 pixels.

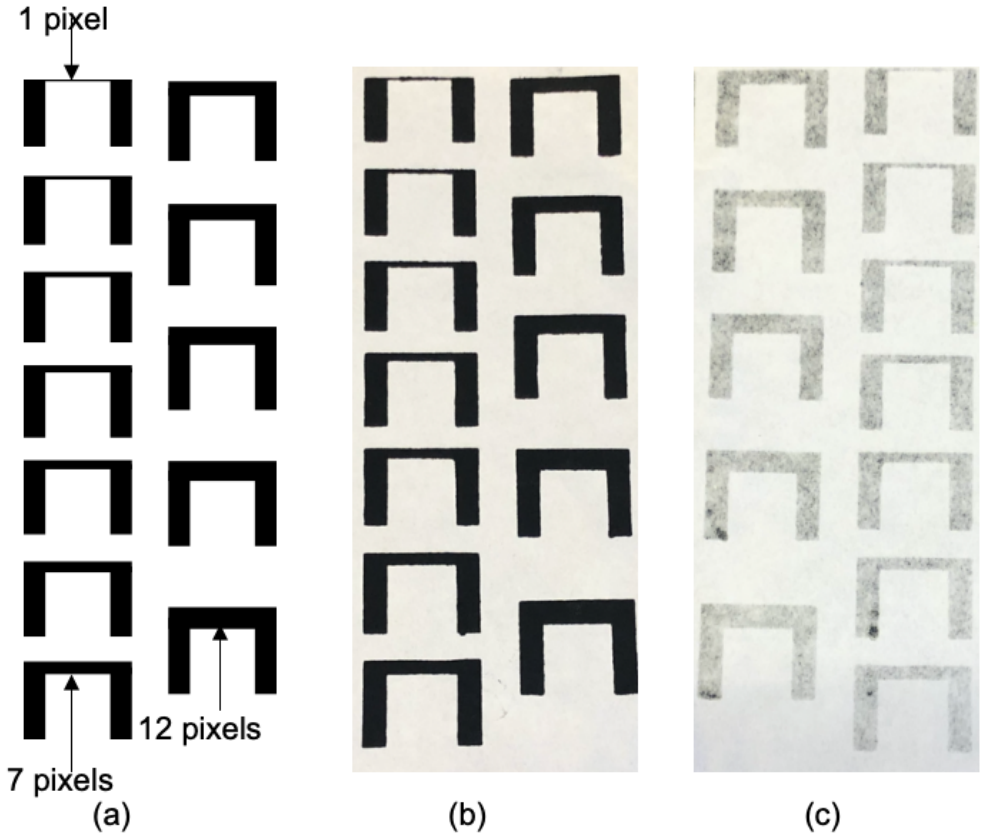

Figure 4.6. Result of UV-curable ink screen printing: (a) digital patterns, (b) photograph of the front of the patterning using UV-curable ink screen printing, (c) photograph of the back of the patterning using UV-curable ink screen printing.

Figure 4.5 shows the comparison between the above three fabrication methods of the hydrophobic barriers. The result of the UV-curable ink screen printing shows that the diffusion of UV-curable ink is more uniform, and the variation of the boundary width is smaller, as illustrated in Figure 4.5(c). Considering the requirements of cost and resolution,

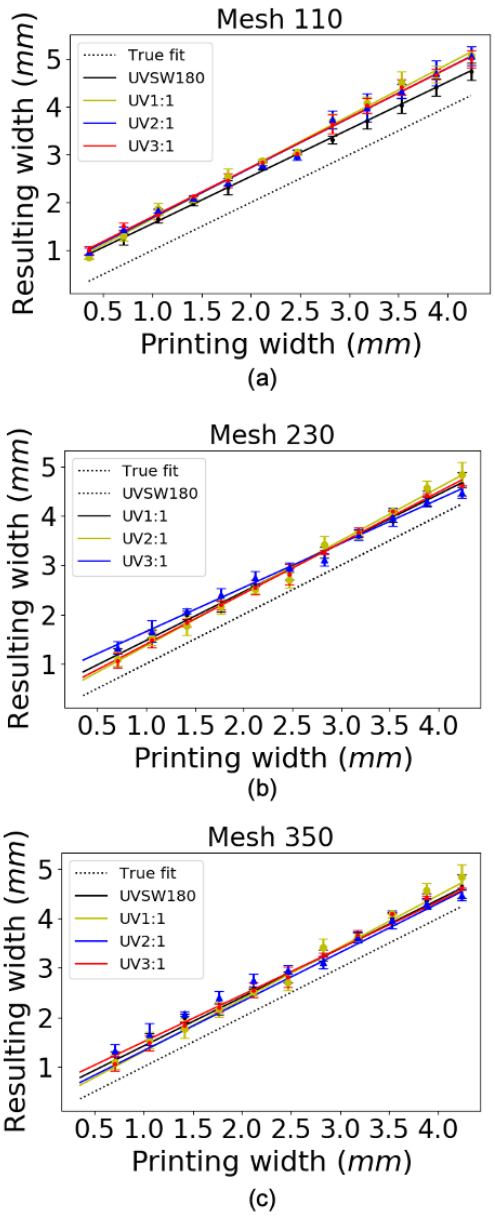

Figure 4.7. Plots of linear fit between the resulting width and the nominal printing width: (a) the linearly fitting lines for mesh 110 are: $y = 0.9881x + 0.5699, y = 1.0784x + 0.5779, y = 1.0425x + 0.6412$, and $y = 1.0342x + 0.6691$, (b) the linearly fitting lines for mesh 230 are: $y = 0.9874x + 0.4854, y = 1.0683x + 0.2963, y = 0.8942x + 0.7585$, and $y = 1.0285x + 0.3675$, (c) the linearly fitting lines for mesh 350 are: $y = 0.9849x + 0.4364, y = 1.0518x + 0.2582, y = 0.9917x + 0.3345$, and $y = 0.9442x + 0.5620$.

we choose UV-curable ink screen printing as the fabrication method for our fluidics paper-based biosensors.

4.2.5 Materials

Paper-based devices are made from Whatman chromatography filter paper (Grade No.1, 20 cm width × 20 cm length). Screen stencils on aluminum frames with 230 polyester meshes (mesh opening 55 μm, Victory Factory, NY, USA), and UV curable inks (Ultra Switch UVSW180 and UVV6 Thinner, Maribu, Barcelona, Spain) are used to pattern the hydrophobic walls on the filter paper.

4.2.6 Fabrication of fluidic paper-based device

We design the digital pattern (mask) on a computer using graphics software (Adobe Illustrator CC 2019), and print it on a transparent film (Lexmark, 12A8240, KY, USA)) with a laser printer (HP LaserJet 500 color MFP, USA).

To improve the penetrating ability of the UV-curable ink, one portion of UVSW 180 and three portions of UVV6 Thinner are mixed and stirred manually. The ink mixture is rubbed through the screen stencil with a squeegee to the filter paper. Owing to the porous structure of the filter paper, the low viscosity UV-curable inks can penetrate into the paper to form well-defined channels on the paper. Finally, the patterned papers are placed under a UV light (120 w/cm, 3 min) to be cured to form the hydrophobic walls.

4.3 Preliminary Pattern Design

To simplify our model, we start with a single target detection with two replicates. As shown in Figure 4.8, the fluidics paper-based device consists of two circular detection zones (diameter D), one central inlet for depositing the sample solution, and two fluidics channels (whole length L, channel width d). Therefore, there are three parameters to be determined: d, L, and D.

For channel width d, we have two main requirements: yield fast flow velocity and less solution loss in the path. We vary the values of d from 1 to 6 mm with an increment of 1

mm to observe the flow velocity and solution loss. Figure 4.9 shows the relationship between d and the flow distance of 100 μl DI water, which flows fastest when the channel width d equals 4 mm.

Moreover, we choose the value of L, the channel length, by pipetting 20 μl aptamer-labels on two test zones to measure the smallest channel length that prevents overlap after the label diffusion. For the optimal value of D (circle diameter), we vary the diameter values from 8 mm to 12 mm with an increment of 2 mm, to choose the one that has the most visible color change by dropping the same amount of aptamer-labels on test areas.

To detect multiple pathogens in one test, we add two more test areas to the paper-based device. The details of the size and shape of our fluidics paper-based device are shown in Figure 4.10(a). The diameter of all the circular pads is 8 mm, and the length of the entire fluidic channel is 20 mm, whereas the width is 4 mm.

4.4 Signal Quantification

The common way to quantity the colorimetric detection of biosensors is to take pictures of the device with an expensive, high resolution and professional digital camera or microscope, then analyze the images to obtain the color values using ImageJ software or Adobe

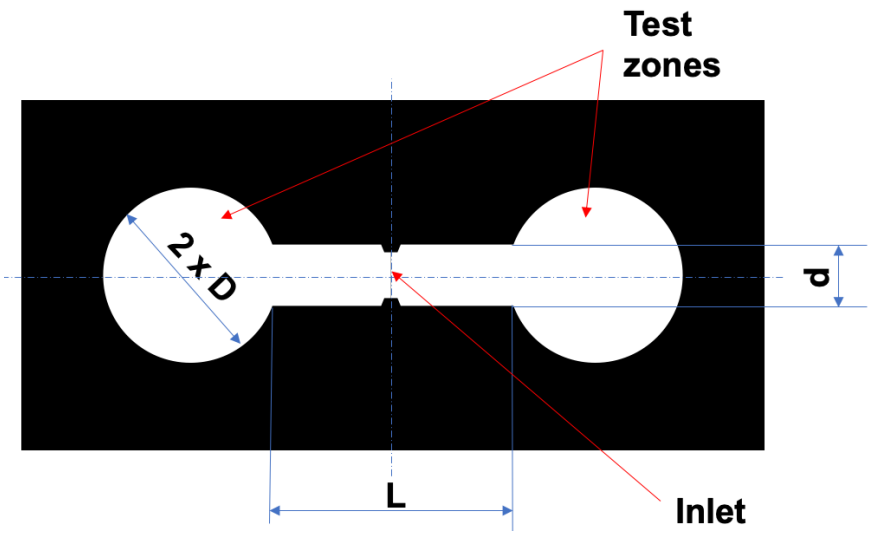

Figure 4.8. Digital pattern with 2 test areas (the black area is the hydrophobic part generated by the UV-curable inks, the white area is paper).

software. Currently, mobile phones have become a popular and accessible platform for diagnostic systems due to the integration of cameras and light-sensors [50]. Motivated by these findings, we set up an optical system to capture images using a mobile phone camera of different batches of biosensors by an optical system in a consistent and controlled illumination environment. Furthermore, the image analysis pipeline designed by our group is enabled to provide on-site recognition of the biosensors, characterization, and quantification of the colorimetric signals from the biosensors with minimal delay.

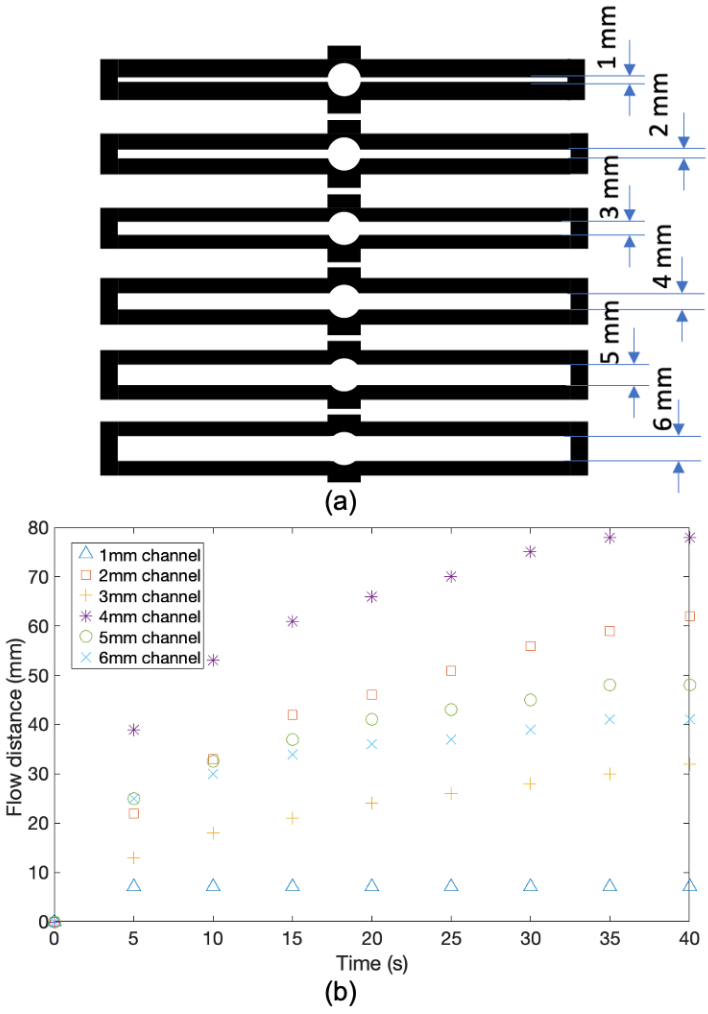

Figure 4.9. The optimization of channel width d: (a) Digital patterns with different channel widths, (b) Flow distance of DI water on the channels with different widths. (Droplet volume = 100 μl).

4.4.1 Colorimetric detection

For the fabrication of the biosensor, 5 μl of the aptamer-functionalized particles (ssDNA-PEI-Au-Ps) binding to Hg^{2+} (the number corresponds to the ion charge) is added to each of the upper two circular pads, and 5 μl of apatamer-functionalized particles specific to As^{3+} is preloaded on each of the lower two circular pads, as shown in Figure 4.10(b). These four pads serve as the colorimetric labels. The biosensor is dried at room temperature for around 10 minutes. To detect the analytes in the test samples, 100 μl of test samples with nine different concentrations of As^{3+}, or Hg^{2+} were dropped in the inlet of the biosensors, from which the solution flowed evenly until reaching the testing areas. There is a colorimetric response in the presence of the target after the test solution interacts with the colorimetric label deposited on each of the testing areas. The color of the target testing areas gradually changes from light pink to deep purple as the concentration increases from 0 ppm to 30 ppm. Then, there is a dramatic color change from deep gray to light gray for a higher concentration test, from 50 ppm to 100 ppm.

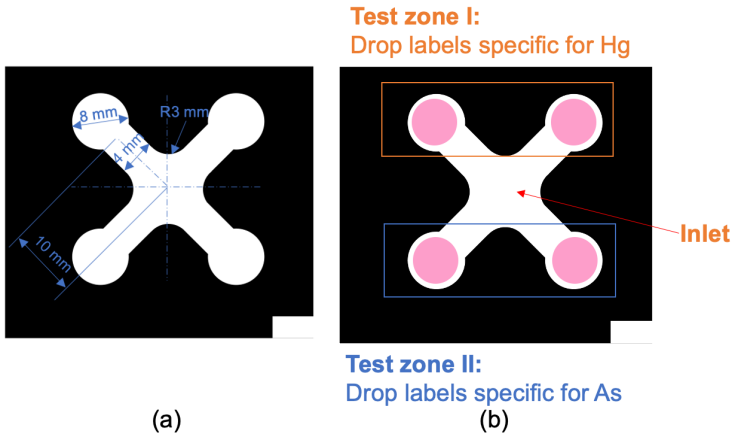

Figure 4.10. The digital patterns: (a) Preliminary pattern design for fluidics paper-based devices with 4 test areas (detail of the size and shape), (b) The preloaded location of the two types of aptamer-functionalized particles (ssDNA-PEI-Au-Ps).

4.4.2 Data acquisition

The colorimetric signals in the detection zones are captured by our optical system, as illustrated in Figure 4.11(a). The optical system mainly consists of a photo studio booth (Amzdeal, 16 ×16, 6500K, purchased from Amazon.com) for providing the controlled D65 illumination environment, a mobile phone camera (iPhone 11 Pro Max, CA, USA), and a fixture to hold the mobile phone. One of the most significant reasons for poor quality images taken is shadows or uneven illumination. To verify the illumination stability of our optical system, ten images of a sheet of paper are taken under the same optical setting in the morning, and afternoon of the day, respectively. The photos are then converted to CIE $L^*a^*b^*$ color space, which is used to analyze the variance of the L^* values. As an example, Figure 4.11(b) shows the L^* value map for an image of the sheet of paper. From this example, it can be concluded that the illumination variation of the captured image is pretty low. Also, the standard deviation of the L^* values averaged over each page, and then averaged over the 10 pages is 0.19, which again, suggests that the illumination variation of the captured image is low.

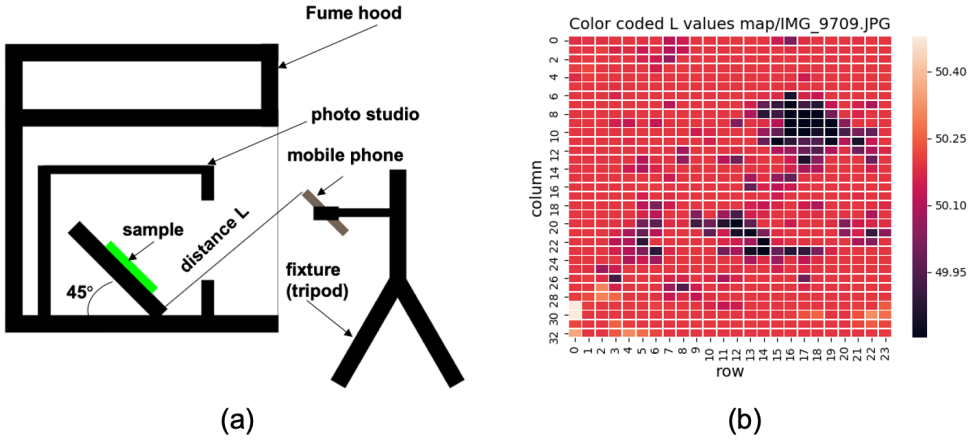

Figure 4.11. (a) The schematic view of the optical system for capturing images, (b) The distribution of L^* values of the image of a sheet of white paper.

4.4.3 Template matching

For our experiment, we captured images of eight biosensors with each photograph. The approximate resolution of each biosensor is 400 × 400 pixels. Figure 4.12(a) shows one of the images captured using our optical system.

The first step in our image analysis pipeline is to identify the region of the captured image corresponding to each of the 8 biosensors. To accomplish this task, we perform template matching [51]. One template image (400 × 400 pixels), including a fabricated biosensor, is chosen to recognize the positions of all biosensors in the source image by labeling all the detected positions of each biosensor using red squares (Figure 4.12(a)) and recording the centroid coordinates of each red square as shown in Figure 4.12(b). Unfortunately, after application of the template matching method to the captured images, the position of each biosensor is detected multiple times, as shown by the thick borders of the red squares in Figure 4.12(a) and by each red pixel cluster in Figure 4.12(b), corresponding to one of the eight biosensors. We will refine our estimates of the biosensor locations using the K-means algorithm, as discussed next.

4.4.4 K-means clustering method

We generate a distribution of the centroids of the red squares, where the two dimensions are the pixel indices in the x and y direction, as shown in Figure 4.12(b). Each red cluster composed of some red dots in Figure 4.12(b) corresponds to all centroid positions of a biosensor detected by the template matching method. To refine our estimates of the biosensor locations, we then apply the K-means algorithm [52] to compute a centroid for each cluster, as shown by the blue dots in Figure 4.12(b). Finally, the individual biosensor images are cropped based on the blue squares determined by the blue dots and saved in TIFF format without compression, as illustrated in Figure 4.12(c).

4.4.5 Image analysis pipeline

After a region of interest is identified, the region of interest is further processed to obtain a quantified measurement of the results. We use image analysis methods to characterize the response of our fluidics paper-based devices to the heavy metals, due to colorimetric changes in the region of interest. We propose an image analysis method to assess the responses by using a mobile phone camera. In this approach, the metric that we use to characterize the responses in each circular detection zone is based on the average grayscale value, which is the average $CIE\ \Delta E$ value in the detection zone. Here, the ΔE value is calculated as the difference between the average L^* value of test area and the average L^* value of a region located in the central inlet. Our image analysis process involves two steps: segmentation of the detection zone or test area and colorimetric signal quantification.

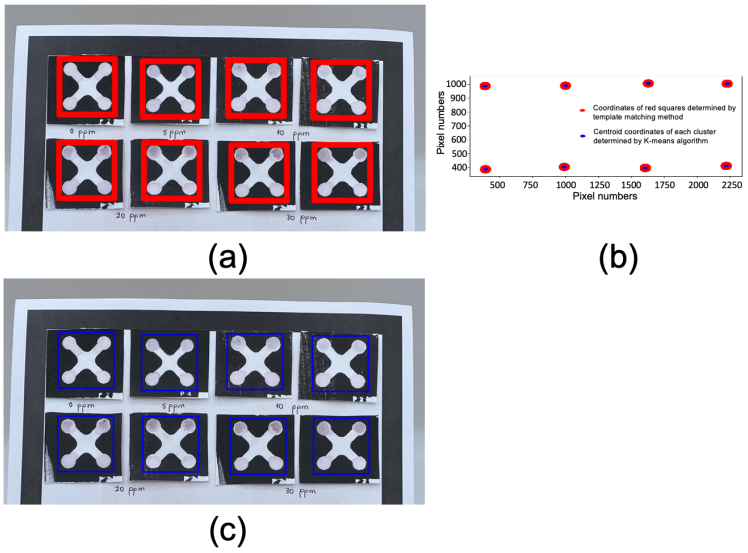

Figure 4.12. The process of extracting the region of interest: (a) The template matching result (the thick borders of red squares show that each ROI has been recognized many times), (b) The distribution of the centroid coordinates (red dots) of the red squares, and the centroid coordinate (blue dot) for each red cluster, (c) The classification results after using K-means algorithm to partition the coordinates of the red squares into 8 regions.

4.4.6 Image segmentation

Image segmentation is one of the essential operations in image processing, in which an image is subdivided into several regions with the aid of pixel information, such as color, lightness, and texture. A number of automatic segmentation methods and unsupervised methods have been developed [16][28]. It is observed that the segmentation result can directly affect the subsequent analysis, and there is no universal or best image segmentation method because different images have different characteristics.

In this section, we focus on a hybrid segmentation approach based on Otsu's method and the K-means clustering method. The first step is to detect the whole channel of each biosensor using Otsu's method. Then, we apply the K-means clustering method to the channels obtained by the boundary detection to segment the test area from the white background. Finally, a morphological operation is applied to remove the noise and boundaries of the channels. The flow chart of the proposed segmentation method is illustrated in Figure 4.13.

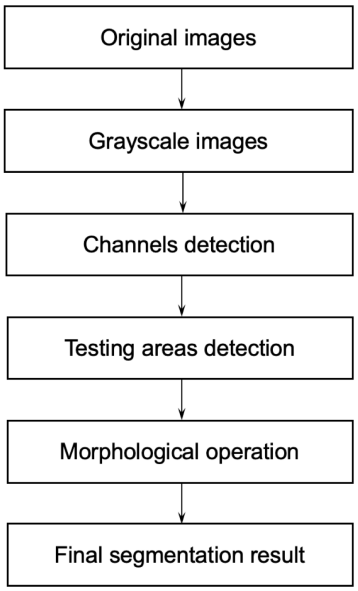

Figure 4.13. Flow chart of the proposed segmentation method.

4.4.7 Otsu's method

Otsu's thresholding method [16] is one of the best-known methods for automatic image segmentation. Based on the histogram of a grayscale image, Otsu's method finds the optimal threshold t^* that maximizes the between-class variance.

To obtain the grayscale images, we transform the gamma-corrected sRGB values of each digital image (Figure 4.14(a)) to $CIE\ L^*a^*b^*$ color space, which has a visually uniform distribution of colors and is closer to human perception of color differences than is sRGB. After transformation, an image difference matrix ΔE of each test image is obtained by subtracting the average $L^*a^*b^*$ value in the central inlet of the biosensor from the test zone images using Equation (4.1),

$$\Delta E(\mathrm{i},\mathrm{j}) = \sqrt{(L^*(\mathrm{i},\mathrm{j}) - L^*_{avg})^2 + (a^*(\mathrm{i},\mathrm{j}) - a^*_{avg})^2 + (b^*(\mathrm{i},\mathrm{j}) - b^*_{avg})^2} \tag{4.1}$$

where (i,j) denotes the pixel indices and $\left(L^*_{avg}, a^*_{avg}, b^*_{avg}\right)$ is the average value in the central inlet. Then, we normalize the ΔE values of the images to the range [0, 255] to obtain our grayscale image for each biosensor, as shown in Figure 4.14(b).

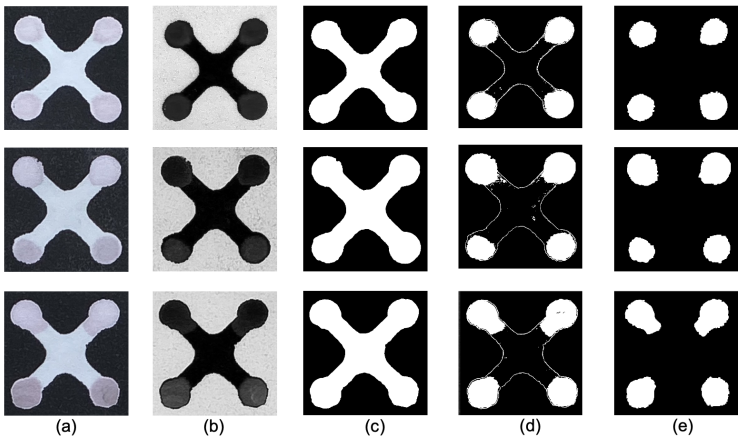

Figure 4.14. Results of the proposed hybrid segmentation approach based on Otsu's method and the K-means clustering method: (a) Original sRGB images, (b) Grayscale images, (c) Channel detection results, (d) Testing areas detection results, (e) Final segmentation results after applying a morphological closing operation.

Otsu's thresholding method works well in segmenting the channels from the black hydrophobic area because the histogram of each image, including the channels, has a strongly bimodal distribution. Figure 4.14(c) shows the channel segmentation results.

4.4.8 Feature selection and K-means clustering method

The following step is used to recognize the testing areas inside the channels. The color difference between the pads and the central inlet region increases as the detected concentration of the analyte increases.

The following features are selected as the input to K-means clustering method: [$L^*(\mathrm{i},\mathrm{j})$, $a^*(\mathrm{i},\mathrm{j})$, $b^*(\mathrm{i},\mathrm{j})$, $\Delta E(\mathrm{i},\mathrm{j})$, $w \cdot \mathrm{i}$, $w \cdot \mathrm{j}$], where $L^*(\mathrm{i},\mathrm{j})$, $a^*(\mathrm{i},\mathrm{j})$, $b^*(\mathrm{i},\mathrm{j})$ are the pixel values in the CIE L^*, a^*, b^* channels. $\Delta E(\mathrm{i},\mathrm{j})$ is the grayscale values of each pixel. i, j are the pixel coordinates, and w is a weighting factor applied to these coordinates. In this case, w is chosen empirically to be 0.05. The number of clusters K equals 5 because there are four testing areas and a white background (filter paper).

After applying the K-means clustering method, we distinguish the four testing pads from the white background, as illustrated in Figure 4.14(d).

4.4.9 Morphological operation

The biosensors in Figure 4.14(d) show the presence of the boundaries of the channels and some noise. Morphological operations are widely applied to remove unnecessary features from images [53]. The basic morphological operations widely used in image processing are erosion and dilation, which are performed over a neighborhood specified by a structuring element or a kernel [54]. To remove the boundaries of the channels and unwanted noise, a window size of 5×5 is chosen to do erosion followed by dilation, which is also called an opening operation. The result in Figure 4.14(e) shows that the opening operation effectively removes the undesired features in Figure 4.14(d).

The final segmentation results prove that our proposed hybrid segmentation combining Otsu's method, the K-means clustering method, and morphological opening enables us to locate the testing areas accurately.

4.4.10 Qantification results

With the aid of the binary images, the position of the colorimetric responses in the testing areas can be defined. We use grayscale values as a metric, calculating average ΔE from the white reference ($[L^*, a^*, b^*] = [93.1927, -2.3147, -0.7811]$) of the response areas of all the devices, to characterize the response of the paper-based devices.

Various concentrations of Hg^{2+} and As^{3+} are tested on the proposed fluidics paper-based biosensors. The detection of each concentration is repeated in at least six replicates, and the data is averaged. The analytical response ΔE is calculated after image processing and analysis. Figure 4.15(a) shows the colorimetric signal evolution versus various concentrations of As^{3+} from 0 ppm to 100 ppm. As illustrated in Figure 4.15(b), correlations can be seen between the ΔE values and the increasing concentrations of the analytes. According to the data collected, the variable ΔE and the As^{3+} concentration is found to be strongly correlated from 0 to 30 ppm, which can be fitted as $y = 0.5218x + 17.1160$, with R^2 of 0.9238. Furthermore, the results in Figure 4.15(b) show evidence that the limit of detection of our proposed biosensor is 2 ppm of As^{3+}. Figure 4.15(c) shows the color evolution of the response for Hg^{2+} under increasing concentrations. The analytical response in Figure 4.15(d) shows the evidence of a linear correlation from 0 ppm to 30 ppm ($y = 0.4562x + 16.8415$, R^2 is 0.8801) with a limit of detection of 1 ppm.

At the higher concentration of 100 ppm, there is a dramatic color change from deep gray to light gray due to an aggregation effect of the aptamer-based particles (ssDNA-PEI-Au-Ps). The mechanism for forming these particles is induced-aggregation. So a higher concentration of the analytes can increase the particle aggregation effect, and grow the particle size. Then, they might start absorbing light at longer wavelengths (IR spectrum). Therefore, the visible wavelengths reflected from the aggregated particles will show a more neutral color.

Figure 4.15(a) shows that there is a non-uniform color response to 20, 30 and 50 ppm on the lower circular pads. To account for spatial nonuniformity of the sensor pad responses, we apply the alpha-trimmed mean filter to calculate the mean response of the pads [55]. The basic idea of the alpha-trimmed mean filter is to eliminate the $\alpha/2$ lowest and the $\alpha/2$ largest grayscale values of each response pad and then compute the average value of the remaining

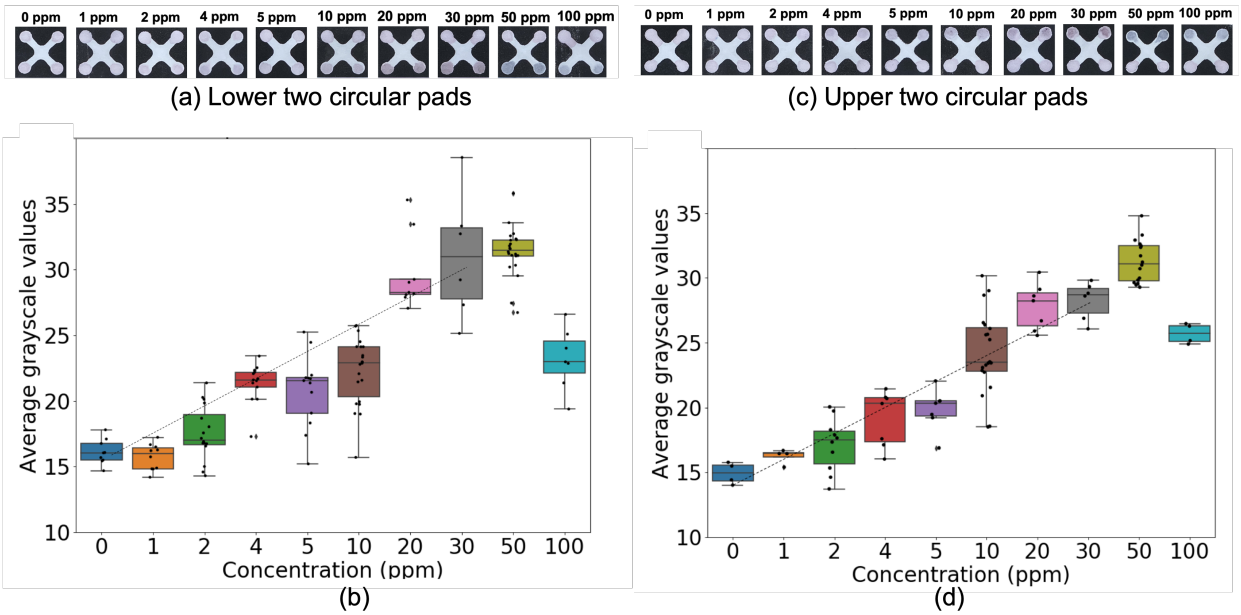

Figure 4.15. (a) The colorimetric signal response to As^{3+}, (b) The correlation between ΔE values and the increasing concentrations of As^{3+}, (c) The colorimetric signal response to Hg^{2+}, (d) The correlation between ΔE values and the increasing concentrations of Hg^{2+}.

values. The selection of the value for α is crucial for a given data set. In this work, we observe the experimental results by tuning the value of α at 10%, 20% and 30%. The experimental results of a response pad is illustrated in Figure 4.16. We note that alpha-trimmed mean estimator is used to remove some outliers from the grayscale distribution, thus concentrating the distribution of grayscale values. We also notice that the difference between the average grayscale value at α of 0% and the value at α of 30% is 0.09, which is negligible.

Figure 4.17 shows the correlation between ΔE values and the increasing concentrations of As^{3+} for 3 different values of α. With these three sets of results, we observe that the ΔE values corresponding to the black dots are very slightly different, and their correlation relationship is very close. Considering that the alpha-trimmed mean filter does not change the distribution of the average grayscale values too much, we will keep using the average ΔE values of the response areas to characterize the response of the paper-based devices.

Our proposed biosensor has been shown to be able to effectively detect heavy metals Hg^{2+} and As^{3+} at a low concentration. To predict the biosensing performance of the proposed

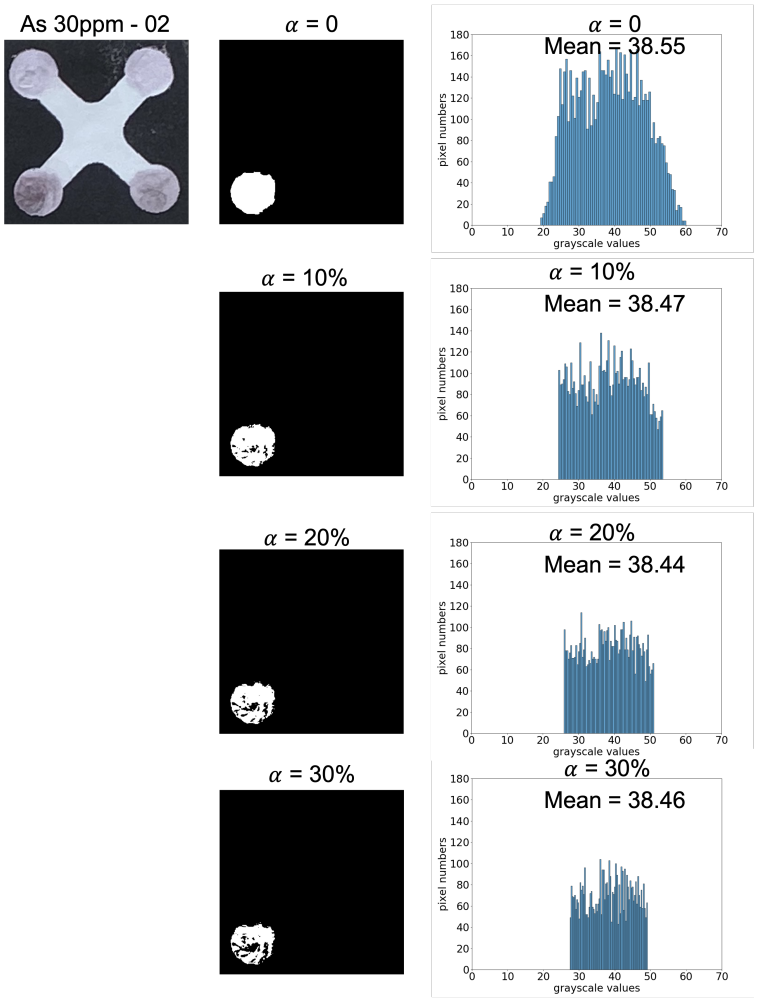

Figure 4.16. (Left) The colorimetric signal response to As^{3+} at 20 ppm, (Middle) The segmentation masks of the lower left pad for three different α values, (Right) The corresponding histograms for three different α values.

paper-based biosensor in complex water, a real sample test of the local river water spiked with Hg^{2+} and As^{3+}, is performed. The detection of each heavy metal with the same concentration is repeated in 3 replicates, and the data is averaged. The analytical response ΔE is calculated after image processing and analysis. Figure 4.18(a) shows the colorimetric signal evolution versus various concentrations of As^{3+} from 0 ppm to 100 ppm in the local river water, and there is a drastic color change from deep gray to light gray at the concentration of 50 ppm (the saturation point of the pure sample is 100 ppm) due to the complexity of the real samples. As illustrated in Figure 4.18(b), correlations can be seen between the ΔE values and the

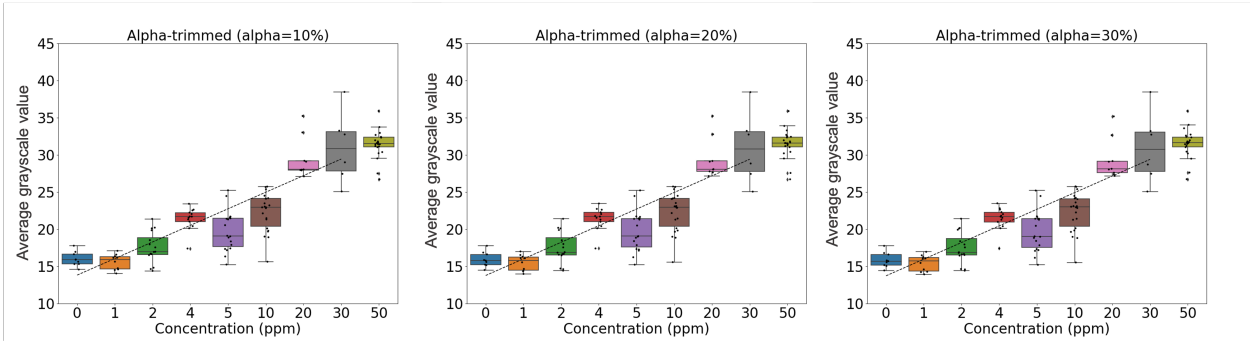

Figure 4.17. The correlation between ΔE values and the increasing concentrations of As^{3+} for three different values of α: 10%, 20%, 30%

increasing concentrations of the analytes. According to the data collected, the variable ΔE and the As^{3+} concentration is found to be correlated from 0 to 30 ppm, which can be fitted as $y = 0.4719x + 17.9294$, with R^2 of 0.7734. Furthermore, the results in Figure 4.18(b) show evidence that the limit of detection of our proposed biosensor is 2 ppm. Figure 4.18(c) shows the color evolution of the response for Hg^{2+} under increasing concentrations in the local river water. The analytical response in Figure 4.18(d) shows the evidence of a strongly linear correlation from 0 ppm to 30 ppm ($y = 0.6306x + 16.1917$, R^2 is 0.9209) with a limit of detection of 2 ppm.

To predict the biosensing performance of the proposed paper-based biosensor in complex solution with various kinds of heavy metals, a specificity test focused on the most common heavy metals Cadmium (Cd), Iron (Fe), Magnesium (Mg), and Lead (Pb) with the concentrations of 50 ppm, is performed. The detection of each heavy metal with the same concentration is independently repeated in 6 replicates; and the data is averaged. The signal of the blank solution is used as a negative reference for comparing the colorimetric signal. The results in Figure 4.19(a) show there is a visually large color difference in the testing areas between the targets and the non-targeted heavy metals. Also, Figure 4.19(b) demonstrates that Hg^{2+} and As^{3+} have the highest positive signal in the test groups after image processing and analysis. Therefore, the test results confirm that our proposed biosensor is highly specific to Hg^{2+} and As^{3+}.

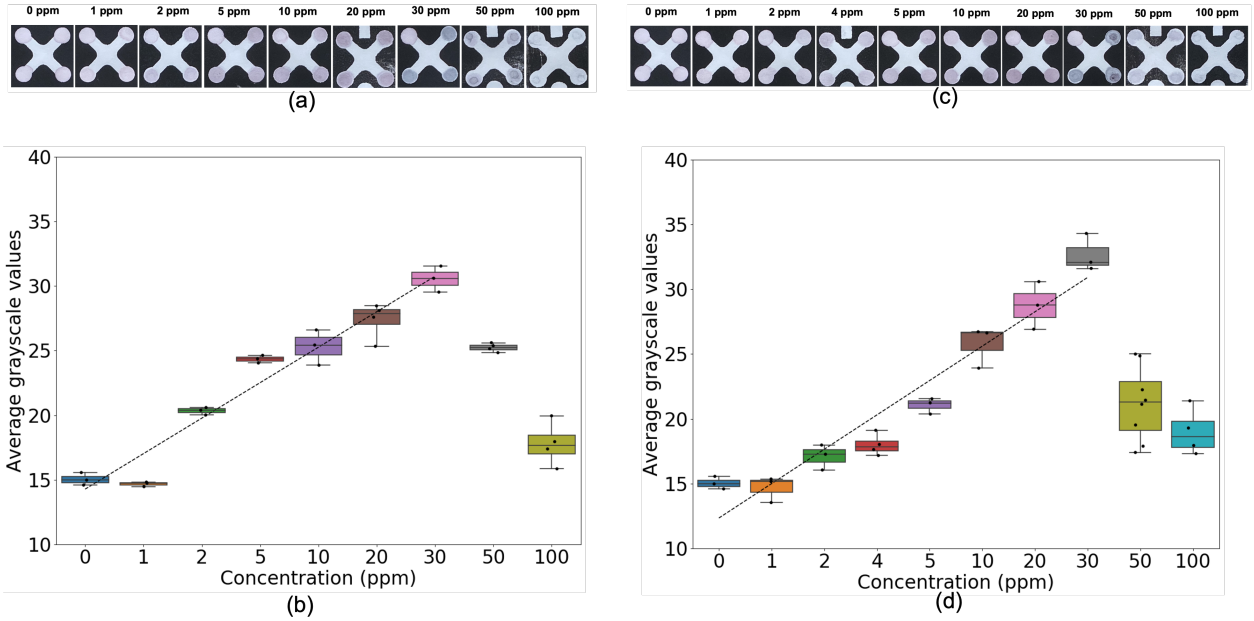

Figure 4.18. (a) The colorimetric signal response to As^{3+} in the local river water, (b) The correlation between ΔE values and the increasing concentrations of As^{3+}, (c) The colorimetric signal response to Hg^{2+} in the local river water, (d) The correlation between ΔE values and the increasing concentrations of Hg^{2+}.

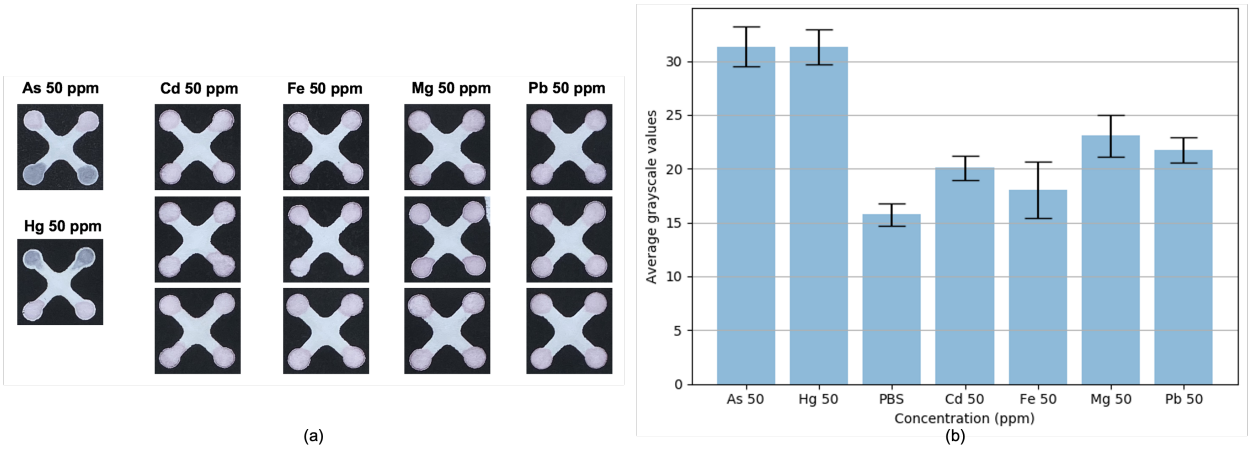

Figure 4.19. The specificity test results of the proposed paper-based devices: (a) Images of the test results, (b) Box plot of the colorimetric signal of the test samples.

To further evaluate the reliability and long-term stability of the response of the proposed biosensor to the analyte, we perform two sets of experiments to observe the colorimetric

signal of the paper-based devices stored at room temperature for several weeks. The paper-based devices are prepared in different weeks, and one batch is used to evaluate the stability of the reagent by testing with the blank solution, the rest of the biosensors are used to test with Hg^{2+} at the concentration of 10 ppm. The difference between the signal for samples with blank solution and Hg^{2+} at 10 ppm is visually apparent and analytically significant at the end of the study period, as illustrated in Figures 4.20(a) and 4.20(b). These results demonstrate that the proposed paper-based biosensor is able to provide temporally robust detection results for the analytes.

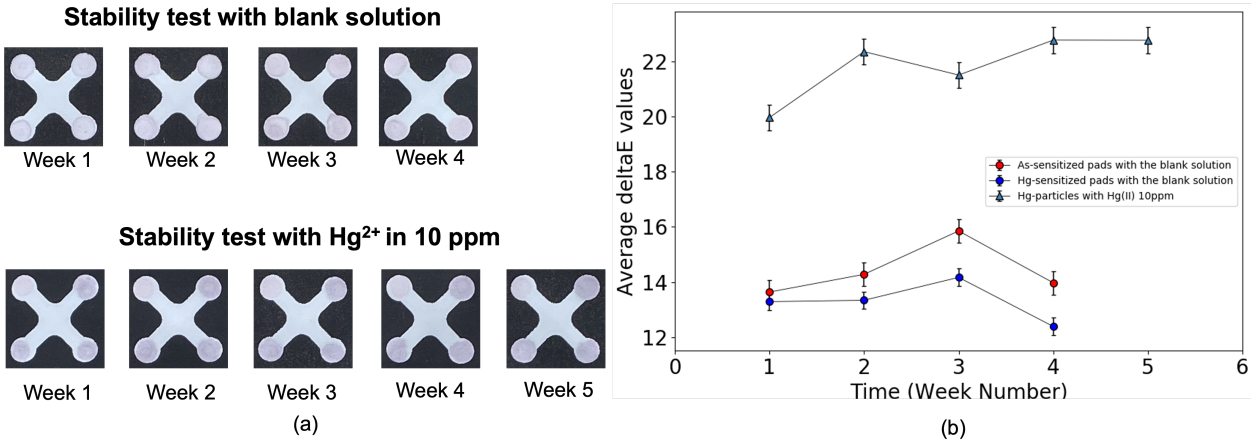

Figure 4.20. The stability test results: (a) Test Images for the samples with blank solution and Hg^{2+} at 10 ppm (3 replicates per each test: upper right, lower left, and lower right), respectively, (b) Analytical results (No data was acquired with the blank solution at the end of Week 5.)

4.5 Conclusion

In this chapter, we have developed a novel biosensor using a paper-based, microfluidic architecture. We explored three different printing technologies for fabricating these devices, and chose screen printing with UV cured inks for further development. We then conducted empirical studies to optimize the device geometry. Finally, we developed a complete image processing pipeline to enable detection of the presence of contaminants in the designed test areas.

Then, we showed that our biosensor can detect the presence of heavy metals (Mercury and Arsenic), and confirmed an Aptamer-based assay detection limit of 1 ppm, and 2 ppm, respectively, for these two contaminants in the pure samples. The relationship between the optical properties and the different concentrations of the target was also investigated. The real sample test, specificity test, and stability results prove that our proposed biosensor is highly specific and robust to the analytes.

5. SPECTRAL IMAGING TO DIFFERENTIATE CONTAMINANT LEVELS

5.1 Introduction

Nowadays, the safety of food has become crucial. One of the main types of threats related to food safety is heavy metals [38]. Heavy metals, including Mercury (Hg), Arsenic (As), Copper (Cu), and so on, can be enriched in living tissue through food chains and have been reported to be harmful to human health at low concentrations. The commonly used methods for detecting heavy metals are mass spectroscopy, atomic emission spectroscopy, potentiometric methods, and so on [44]. These methods are sensitive, but require expensive equipment, trained personnel, and cannot support on-site detection. Therefore, rapid and low-cost detection methods for contaminants are more and more in demand.

To detect multiple targets in one test, our group focuses on developing a novel paper-based, microfluidic biosensor for colorimetric detection of two types of heavy metals: As and Hg [56][57]. Figure 5.1 shows the proposed detection mechanism of our biosensors and the test interpretation. A cell-phone integrated image analysis pipeline can determine the detection result of our biosensors. Two kinds of the aptamer-functionalized particles (ssDNA-PEI-Au-Ps) specific to Hg^{2+} and As^{3+} are preloaded on each of the upper, and lower two circular pads, respectively. These four pads serve as the colorimetric labels. To detect the analytes in the test samples, test samples with different concentrations of Hg^{2+} or As^{3+} were dropped in the inlet of the biosensors. There is a colorimetric response in the presence of the target after the test solution interacts with the colorimetric label deposited on each of the testing areas. Figure 5.2 shows the colorimetric signal evolution versus various concentrations of As^{3+} and Hg^{2+} from 0 ppm to 100 ppm. The color of the target testing areas gradually changes from light pink to deep purple as the concentration increases from 0 ppm to 30 ppm. Then, there is a drastic color change from deep gray to light gray for a higher concentration test, from 50 ppm to 100 ppm.

To yield a quantitative and objective color analysis, color measuring instruments are favored. As digital technologies continue to develop, cheap, and compact image sensors

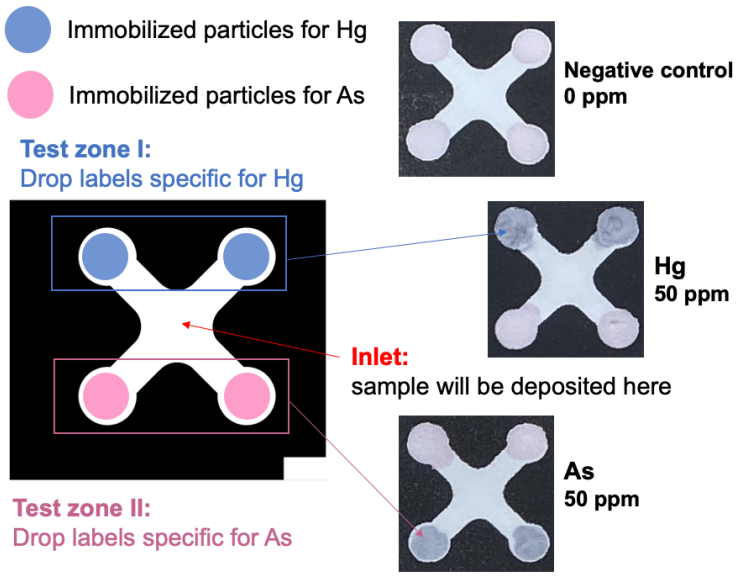

Figure 5.1. The detection mechanism of our biosensors and test interpretation. (To illustrate the different particles specific for Hg and As, the particles specific for Hg are labeled blue in the figure; but the actual particles are colored light pink.)

are widely used in everyday electronics, like cell phones. A phone-based imaging system is promising for signal detection due to the above features emerging in different fields.

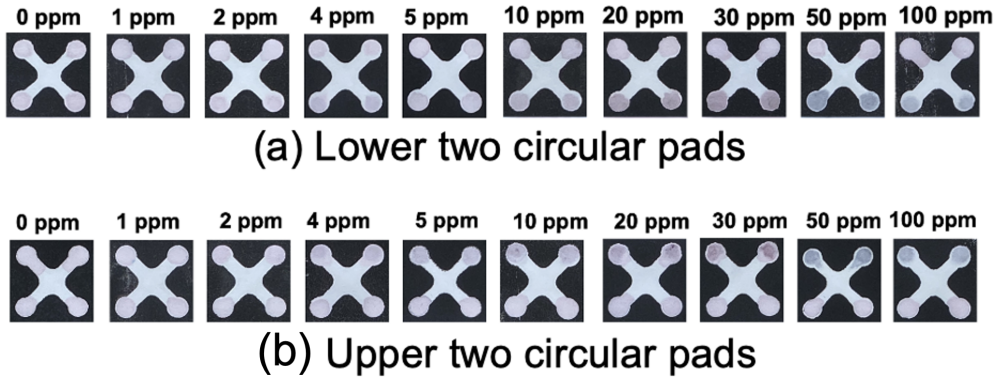

Figure 5.2. (a) The colorimetric signal response to As^{3+}, (b) The colorimetric signal response to Hg^{2+}.

In our previous work, our proposed optical system and image analysis pipeline provides consistent data acquisition captured by a mobile phone camera, and delivers quantitative responses to correlate the colorimetric change of the biosensors to the concentration of the target substance [57]. We used the grayscale values as a metric, calculating average $CIE\ \Delta E$ [25][58] from the white reference, to characterize the response of the paper-based devices,

and to correlate the response with the concentration of the analytes. As an example, Figure 5.3 shows the correlations between the ΔE values and the increasing concentrations of As^{3+}. According to the data collected, the variable ΔE and the As^{3+} concentration is found to be strongly correlated from 0 to 30 ppm, which can be fitted as $y = 0.52x + 17.12$, with R^2 of 0.9238. Nonetheless, the relationship is not monotonic. In particular, the repsonses to 0 ppm and 4 ppm are too high.

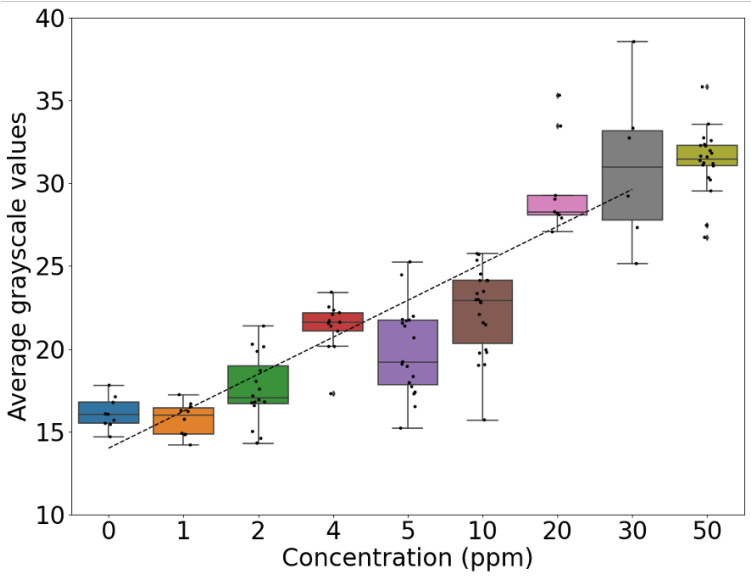

Figure 5.3. The correlation between ΔE values and the increasing concentrations of As^{3+} for a non-spectral imaging method.

Thus, we aim to find a prediction model with higher accuracy for our limited data set. In this study, the colorimetric responses of 5 contamination levels (As^{3+}) are used as the experimental data. Considering the limited number of samples for each concentration, we first rearrange the 126 phone captured images of the samples into five classes: 35 in Class 1 (0, 1, 2 ppm), 32 in Class 2 (4, 5 ppm), 22 in Class 3 (10 ppm), 15 in Class 4 (20, 30 ppm), and 22 in Class 5 (50 ppm). Then, we divide the original dataset into a training set, a validation set, and a test set according to the ratio 5: 2: 3, as shown in Table 5.1.

In the following sections, we first present an overview of the base model using grayscale values and its prediction accuracy. Second, we propose two classification models for discriminating the spectral responses for the different classes; then, we compare the prediction accuracy. Finally, we present our phone-based narrow-band spectral imaging system that

Table 5.1. Overview of the small-scale dataset showing the division, respectively, into training, validation, and test sets.

Class	Training set	Validation set	Test set	Total
Class 1	17	7	11	35
Class 2	16	6	10	32
Class 3	11	4	7	22
Class 4	7	3	5	15
Class 5	11	4	7	22

can obtain the camera spectral response for accurate and precise heavy metals analyses with the aid of a narrow bandpass filter in front of the cell phone's camera lens.

5.2 Base Model

For our base model, we use grayscale as a metric to characterize the responses for the different classes. In this section, we present two methods to evaluate the prediction accuracy of our base model. In the first model, we apply the Lloyd-Max scalar quantizer method to find the optimal threshold boundaries, i.e. average ΔE values, for the training data of five classes [59][60]. Figure 5.4 shows the optimal threshold boundaries for the five classes. The prediction accuracy for the test dataset is shown in Table 5.2. The base model shows a relatively high prediction accuracy for Classes 1 and 5, but a relatively low accuracy for Classes 2 - 4, with an average prediction performance of 41%.

Table 5.2. Performance of the quantizer method based on ΔE from the global background.

Class	C 1	C 2	C 3	C 4	C 5
Accuracy	91%	60%	43%	20%	86%

In the second model, we propose a DAGSVM model for differentiating contaminant levels [61][62]. Figure 5.5 shows the structure of the DAGSVM for predicting the class of our five-class. The DAGSVM model comprises 10 SVM classifiers. This proposed system is trained and evaluated on 126 responses of five contamination levels, as shown in Table 5.1.

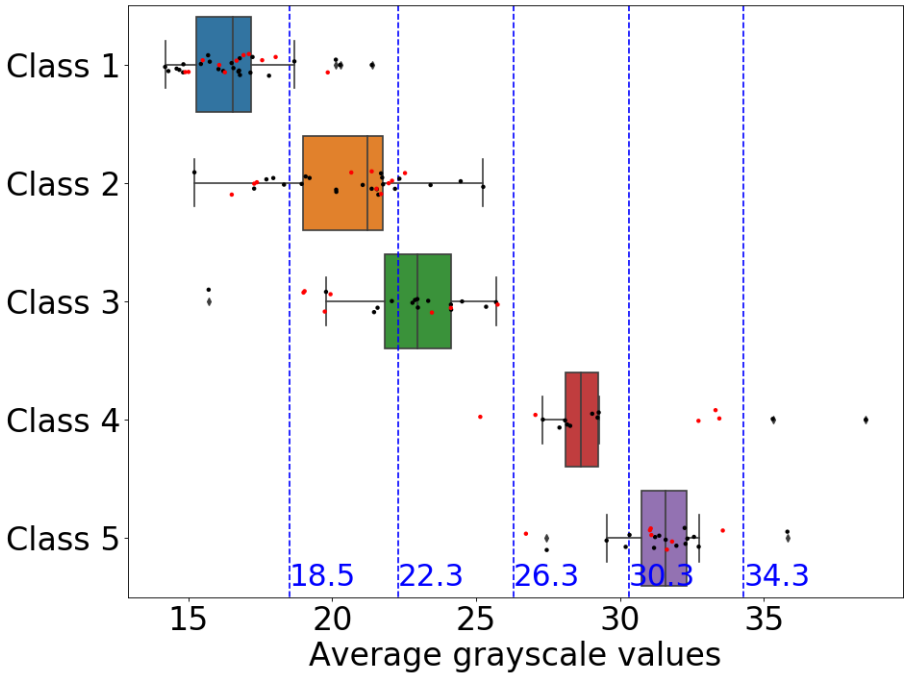

Figure 5.4. The optimal threshold boundaries for 5 classes detecting As^{3+} for the base non-spectral imaging method. (Dark points represent the training data, and red points show the test data.)

Considering the limited datasets, we evaluate the performance of the five-class classification model by processing the leave-one-out cross-validation [63]. One data point per training procedure will be used as the validation set and the rest of the data points are used as the training set. Table 5.3 shows the confusion matrix for the test data set. The DAGSVM model yields 69% average accuracy, which is higher than the result of the first model, and shows a relatively higher predication accuracy for Class 3 than the first model. However, we also observe that the DAGSVM model shows the same low accuracy for Class 4.

Table 5.3. Performance of the DAGSVM model based on ΔE from the global background.

Class	C 1	C 2	C 3	C 4	C 5
Accuracy	73%	70%	71%	20%	86%

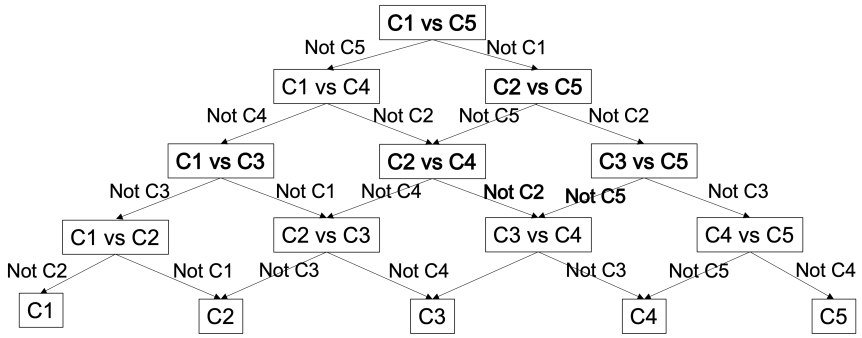

Figure 5.5. The tree structure of the DAGSVM for predicting the class of our five-class framework.

The ΔE from the global background method calculates the Euclidean distance between the white reference and the response area. As can be seen in Figure 5.4, there exist situations where the ΔE values calculated from two different reaction colors are out of order, which causes low accuracy. The limited dataset and the insufficient utilization of the spatial information contained in the sensor pad images also restrict the effectiveness of the base model.

5.3 Spectral Imaging Classification Models

The main challenges of our project are the insufficient feature information, the limited number of samples, and the large intra-class variance of the sensor pad images. To overcome these challenges, we use the spectra data of the colorimetric response pads and propose two kinds of classification models for differentiating contaminant levels with higher test accuracy.

5.3.1 Non-contact optical measurement system

The spectral radiance in the detection zones is acquired by our non-contact optical measuring system, illustrated in Figure 5.6. The optical system mainly consists of a photo studio booth (FotodioX LED440-16×16, purchased from bhphotovideo.com) for providing the controlled illumination environment, and for measuring the visible wavelength range, a spectroradiometer (PR 705, Photo Research Inc., CA, USA), and a tripod to provide a 45° configuration of the spectroradiometer. The spectral radiance of the samples and of a

white reflectance standard (Spectralon white diffuse reflectance standard, model #54-302, Edmund Optics) are obtained from 380 nm to 780 nm with an interval of 2 nm. To evaluate the stability of the illumination light intensity, the measurements of the spectral irradiance of the white reflectance standard are taken every 30 minutes for 3 hours. Then the spectral reflectance of the colorimetric response is calculated by dividing the spectral radiance of the object by the average reflectance radiance of the perfect reflecting standard under the same spectral conditions of measurement [64][65].

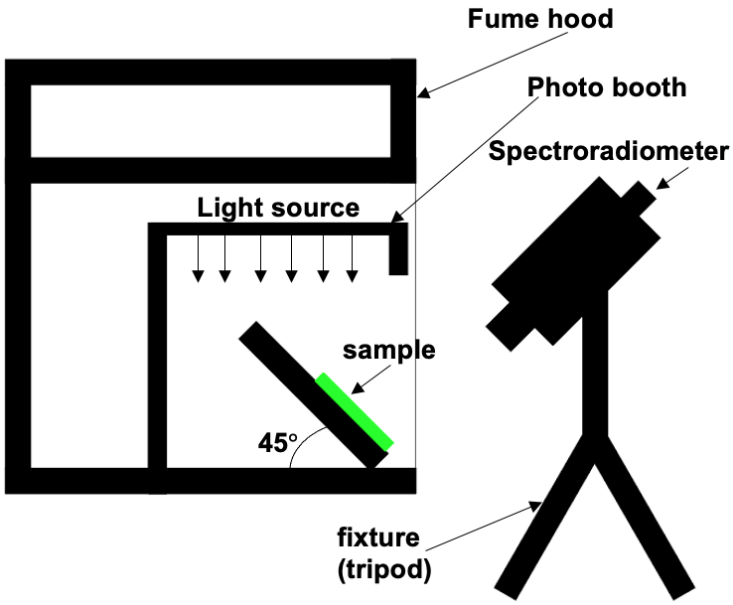

Figure 5.6. The optical setup for spectral data acquisition.

The light sources used are an LED light (FotodioX LED440-16×16, purchased from bhphotovideo.com), fluorescent light (mounted on the ceiling of the laboratory), and halogen light (Sunlite 100T10 frosted Halogen double envelope lamp, purchased from bhphotovideo.com). Figure 5.7 shows the relative luminous power comparison of these three kinds of illumination used in our project. Our goal is to find the optimal illumination source for which the spectral data of the entire set of objects (responses of As^{3+} and of Hg^{2+}) are most separated for each different concentration. The spectral radiance of each object under the three illuminations is taken and averaged with respect to wavelength. At each illumination level, we measure the spectral emissivity of all test responses and calculate the average spec-

tral radiance for each level. Figure 5.8 shows an example of the average spectral radiance curves for As^{3+} for all five contamination levels. We can note that there is a correct order between the average spectral radiance and the contamination levels in the wavelength range above 620 nm. Table 5.4 records the relationship between the averaged spectral reflectance and the contamination levels under the three different illuminations. From the table, we note that for both As^{3+} and Hg^{2+}, there is a correct order between their mean spectral radiance and the contamination levels. So we can conclude that the LED source is optimal to distinguish the different concentrations of the colorimetric response of both As^{3+} and Hg^{2+}. LED illumination is thus used as an optimal light source for spectral acquisition.

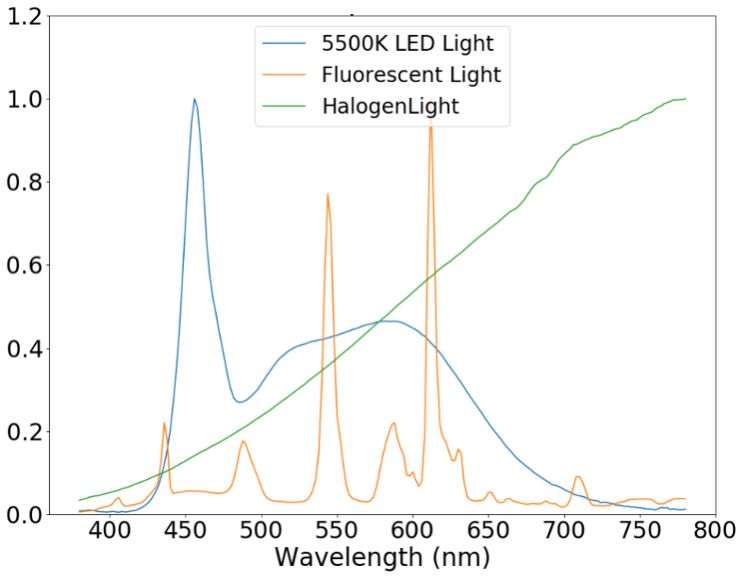

Figure 5.7. The relative luminous power comparison of the three kinds of illumination sources.

5.3.2 Data description

The spectral radiances of the colorimetric responses to As^{3+} are used as the experimental data. The curve in Figure 5.8 represents the mean of all spectral radiance measurements of the training samples for each contamination levels. Although there are visible differences at approximately 460 nm and from 480 nm to 600 nm, the spectral radiance curves have quite similar shapes within the visible wavelength range.

Table 5.4. The relationship between the averaged spectral radiance and the contamination levels under the three different illuminations.Here "Cmm → Cnn" means that Cmm has a higher averaged spectral radiance than Cnn. Note that we only observe the correct ordering across all five concentrations with both contaminants for the 5500K LED illumination.

Illumination	As^{3+}	Hg^{2+}
Fluorescent Light	C1 → C2 → C3 → C4 → C5	C2 → C1 → C3 → C4 → C5
5500K LED Light	C1 → C2 → C3 → C4 → C5	C1 → C2 → C3 → C4 → C5
Halogen Light	C1 → C2 → C3 → C4 → C5	C2 → C1 → C3 → C4 → C5

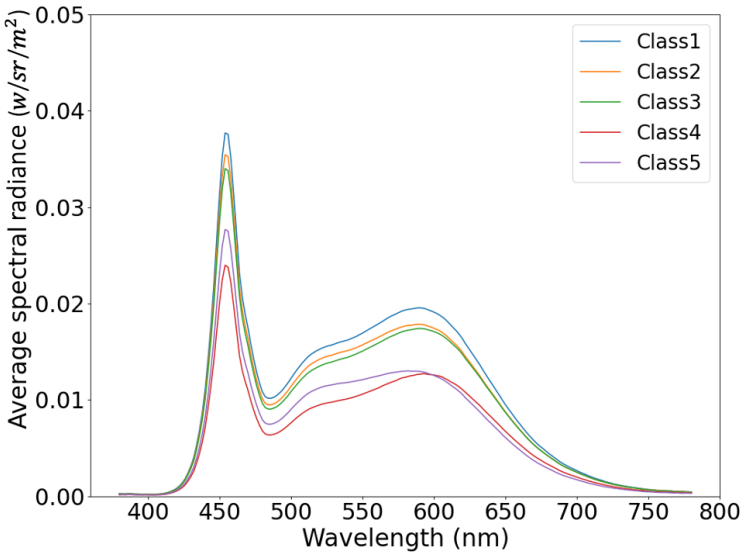

Figure 5.8. The mean spectral radiance measurements of the training samples for five contamination levels of As^{3+}. The measurements were made under the LED illumination. Note that spectral radiances decrease according to increasing class number at each fixed wavelength above 620 nm.

The data set comprising 126 spectral radiances at 5 contamination levels, are randomly divided into training, validation, and test data sets, as shown in Table 5.1. For each sample, the measured spectral band varies from 380 nm to 780 nm with a sampling interval of 2 nm; this leads to an original vector space of dimension 200. The number of components of the feature vector is much larger than the small number (less than 40) of samples for each class in our application. The number of training samples required for typical machine learning problems increases dramatically with the dimensionality for such high dimensionality [66].

Therefore, the first step in preprocessing is to obtain smaller feature dimensions by dividing the spectral range of the wavelengths into 20 equal parts, then calculating the corresponding averages within each wavelength range. The corresponding feature names are '390 nm', '410nm', … , '770 nm', which are the center wavelengths of each interval.

5.4 Machine Learning Algorithm

The next goal is to develop classification models for differentiating contaminant levels with high test accuracy. The majority of the existing works prove that k-nearest-neighbor and random forest classifiers have powerful classification capabilities [67][68]. Further, sequential selection and PCA are widely used to extract a subset of features in higher dimensions to improve computational efficiency and reduce the generalization error of classification [7][69]. Based on this, we use the spectral data of the colorimetric response pads and propose two kinds of classification models for differentiating contaminant levels with high test accuracy. The flow chart of the general machine learning pipeline for these two models is shown in Figure 5.9.

Here, two kinds of classification models are investigated in our work to evaluate their classification accuracy and generalizability to the test data.

5.4.1 Multiclass classification model I

In the first model, we apply the sequential forward feature selection (SFS) algorithm [7] to select or extract a subset of wavelength features in combination with the k-nearest-neighbor (k-NN) classifier to discriminate five contaminant levels.

5.4.2 Sequential forward feature selection

After the first step of preprocessing, we have 20 wavelength features for each set of spectral radiance data. To improve the classification performance and simplicity, we can further reduce the dimensionality. Sequential feature selection has been recognized as a crucial feature selection technique. It is an iterative procedure. The SFS method performs the following steps: (1) starts with an empty feature set, (2) generate all possible feature

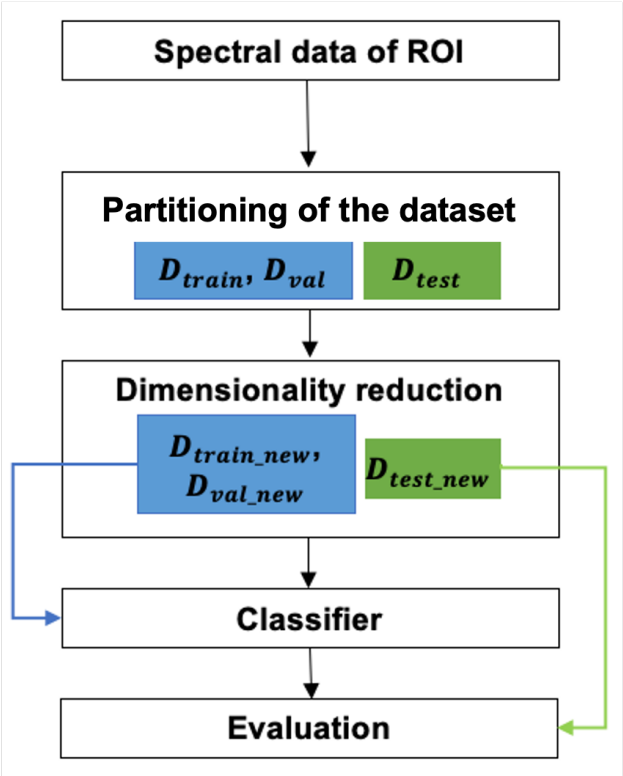

Figure 5.9. The flow chart of the general machine learning pipeline for the two proposed classification models.

subsets of size 1, then choose the feature subset that leads to the best classification accuracy, (3) add another feature from the remaining available features to generate all possible feature subsets of size 2, (4) gradually add features until the size of the subsets is equal to the number of desired features, or until the classification accuracy starts to decrease or no longer increases. In this work, we apply the SFS based on the k-NN classifier to choose a subset of wavelength features that yields the minimum classification error.

5.4.3 k-NN classifier

The k-NN classifier is one of the most widely used classification methods. It is based on the majority vote of the neighbors of the test sample. The k-NN method calculates a distance between the test sample and all training samples to obtain its nearest neighbors, and then assigns the test sample a label according to the majority vote of the k nearest neighbors [70].

We calculate the standard Euclidean distance in the feature space to measure the similarity between the test sample and the training samples. As is well known, the selection of the value for k is crucial for good classification performance. In this work, we obtain the appropriate value for k experimentally. With the validation data set, we evaluate the k-NN classifier with different k values from 1 to 6. This procedure can be repeated each time by increasing k to include one more neighbor. Two examples are illustrated in Figure 5.10. We note that almost all of these 6 models yield 80% validation accuracy when 4 wavelengths are selected, so the feature subset's size is taken as 4. The k value is chosen to be 5 because the validation accuracy stabilizes after a certain point as the number of feature selections increases. The optimal wavelength features include 670 nm, 490 nm, 410 nm, and 430 nm.

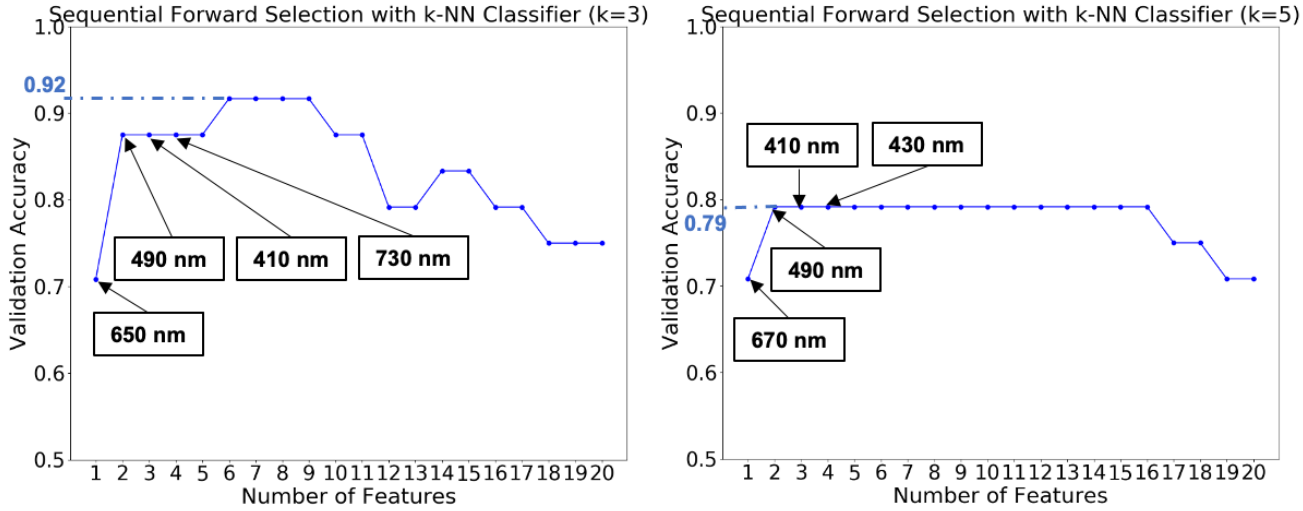

Figure 5.10. Validation accuracy of the k-NN classifier models with $k = 3$ and $k = 5$, respectively.

5.4.4 Classification result of model I

We perform 4-fold cross-validation to evaluate the performance of the k-NN classifier ($k = 5$) with the SFS algorithm. The confusion matrix for the test data is reported in Table 5.5. The classification performance yields 84.4% average precision, 76.7% average recall, and 80.4% average F-1 score. We note that the low classification accuracy for Class 3 might be due to the fact that a fixed k-NN classifier is applied to all test samples. This leads to a low

prediction rate in real applications in many existing works because the fixed classifier for all test data does not consider the distribution of the data [71].

Table 5.5. Confusion matrix for the multiclass classification model I (k-NN classifier).

Class	C 1	C 2	C 3	C 4	C 5	Precision	Recall
C 1	10	1	0	0	0	84.6%	90.9%
C 2	4	5	1	0	0	62.5%	50%
C 3	2	2	3	0	0	75 %	42.9%
C 4	0	0	0	5	0	100%	100%
C 5	0	0	0	0	7	100%	100%

5.4.5 Multiclass classification model II

The second classification model comprises principal component analysis (PCA) used as a dimensionality reduction technique in combination with a random forest (RF) classifier to classify five contaminant levels.

5.4.6 PCA

Principle component analysis (PCA) is one of the most widely used algorithms for reducing redundant and irrelevant features. PCA uses singular value decomposition to project the high feature dimensions into an orthogonal basis set called the principal components, while preserving as much of the data's variation as possible [69][72]. In our work, PCA is applied to the training data set to select the principal components that explain the data's maximum variance. Figure 5.11 shows that the first three principal components can cover 99% of the variance of the training data set. Then, we reduce the original feature vectors of the testing data to the same lower dimensional subspace as the training data set.

5.4.7 Random forest

Random forest (RF) has been successfully applied to multiclass classification problems [9]. The RF algorithm is an ensemble method of classification based on generating multiple

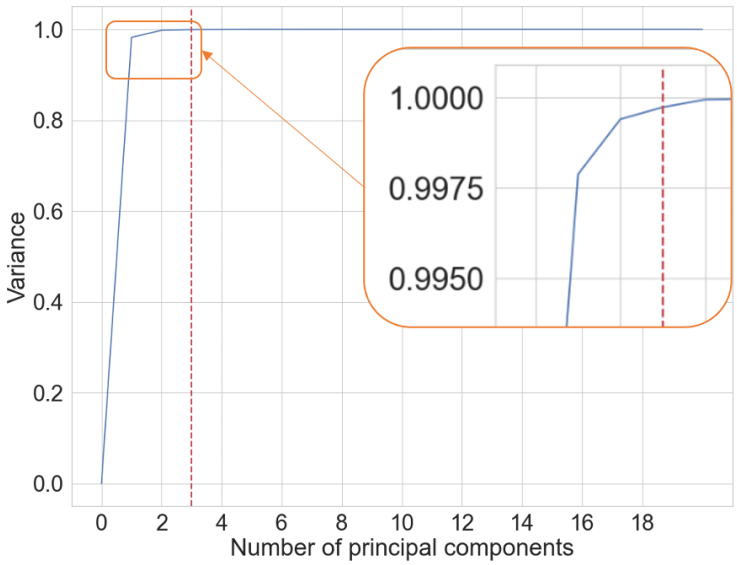

Figure 5.11. Variance of the first 20 principal components for the training data set.

decision trees. The RF algorithm independently constructs each tree using bootstrap sample data. Each node in the standard tree is split using the best decision based on a randomly chosen subset of the input variables. Each tree in RF predicts its output; then, the RF makes a final prediction based on the majority vote of all the trees.

5.4.8 Classification result of model II

The RF models involve several parameters: depth of trees, number of features randomly selected, and number of trees in the forest. We perform 4-fold cross-validation to select the optimal parameters which yield the lowest classification errors on the validation data set.

After selecting the optimal parameter values, the classification model is evaluated on the test data with the lower dimensional subspace. Table 5.6 shows the confusion matrix for the test data. The classification performance yields 86.8% average precision, 86.6% average recall, and 86.7% average F-1 score. It turns out that the RF model with PCA feature selection performs well in terms of accuracy compared to the k-NN classifier.

Table 5.6. Confusion matrix for the multiclass classification model II (RF classifier).

Class	C 1	C 2	C 3	C 4	C 5	Precision	Recall
C 1	9	1	1	0	0	90%	81.8%
C 2	1	8	1	0	0	72.7%	80%
C 3	0	2	5	0	0	71.4 %	71.4%
C 4	0	0	0	5	0	100%	100%
C 5	0	0	0	0	7	100%	100%

5.5 Phone-based Narrow Band Spectral Imaging

In the previous sections, we prove that the spectral data of the colorimetric response pads can improve classification performance. The challenging part is that the spectral data must be obtained using an expensive and professional optical component, like a spectroradiometer. As digital technologies continue to develop, cell phones are cheap and widely used globally, so a phone-based spectral imaging system is promising for differentiating different contaminant levels.

We propose a smartphone-based narrow-band spectral imaging system that incorporates a hardware plug-in module that fixes a bandpass filter in front of the smartphone's camera lens, as illustrated in Figure 5.12. In the optical setup, the cell phone (iPhone 8, CA, USA) with a bandpass filter (center wavelength is 620 nm, and full width at half maximum is 10 nm, Edmund Optics Inc., Barrington, NJ) replaced the spectroradiometer on the tripod, as shown in Figure 5.6. We also conduct a preliminary evaluation of the proposed phone-based narrow-band spectral imaging system regarding its performance and capability to replace the spectroradiometer.

We use the average red channel value of the colorimetric response under the bandpass filter to represent the camera response. Figure 5.13 shows the camera response for various concentrations of As^{3+} from 0 ppm to 50 ppm. According to the data collected, it is found that the variable camera response had a very similar trend to the spectral radiance at As^{3+} concentrations from 0 to 50 ppm. Our preliminary result suggests that the phone-based narrow-band spectral imaging system can replace the spectroradiometer for differentiating different contaminant levels.

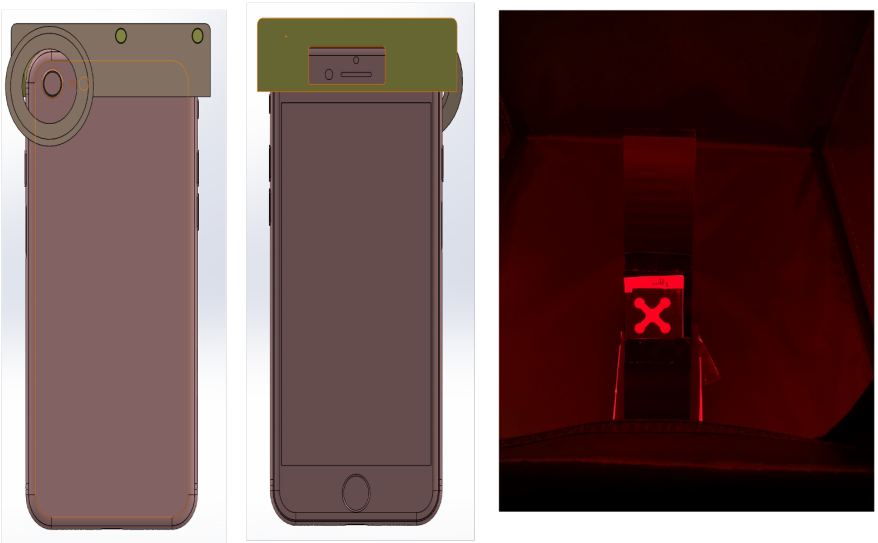

Figure 5.12. (Left) 3D model of add-on for iPhone 8. (Right) The image captured with the 620 nm bandpass filter.

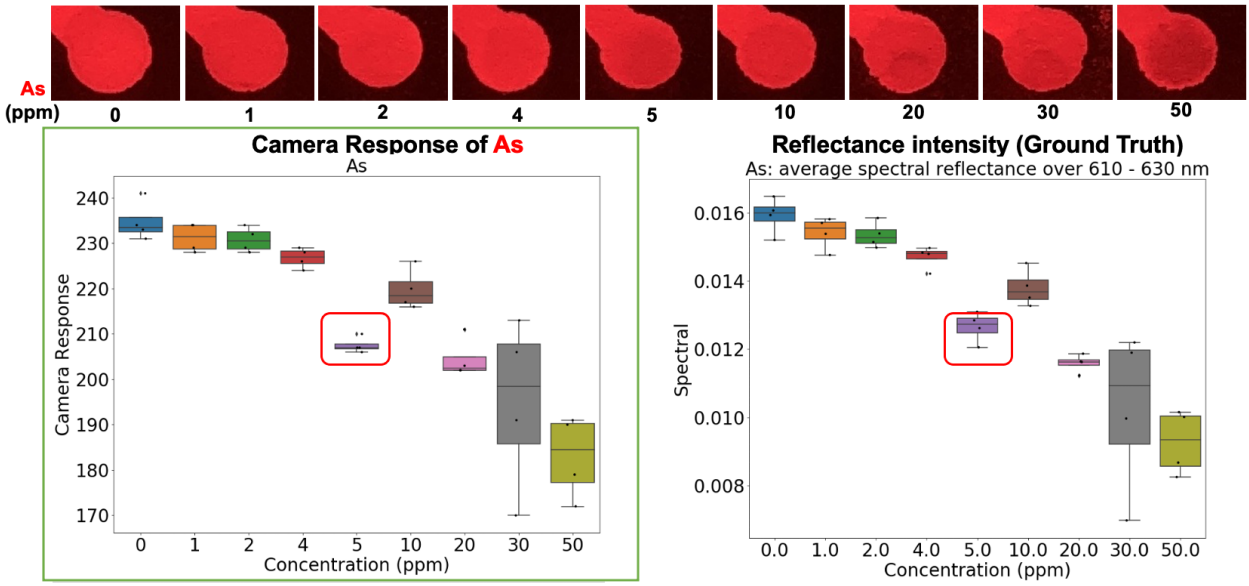

Figure 5.13. (Top) Bandpass-filter-equipped camera captured images of a sensor pad with different concentrations of As^{3+}. (Left) Box plot of the camera responses with a bandpass filter (620nm) for different As^{3+} concentrations. (Right) Box plot of the corresponding spectral radiances measured by using the PR 705.

To evaluate whether the camera responses can be used for classification, we collect the camera responses (the average red, and green channel value) of all samples and use ran-

dom forest classifier to classify five contaminant levels. Table 5.7 shows the corresponding confusion matrix for differentiating camera response of the test data. The classification performance yields 73% average accuracy, which is higher than the classification accuracy of our base model, as shown in Table 5.2.

Table 5.7. Confusion matrix for differentiating camera response of the test data).

Class	C 1	C 2	C 3	C 4	C 5	Precision
C 1	9	2	0	0	0	82%
C 2	1	4	2	1	0	50%
C 3	0	2	5	0	0	71%
C 4	0	1	0	4	1	80%
C 5	0	0	0	1	4	80%

5.6 Conclusion

In this chapter, we investigated how to improve the accuracy of our previously developed paper-based devices for detecting and measuring heavy metal contaminants (As^{3+} and Hg^{2+}) in food or liquids. Specifically, we considered the use of the spectral reflectance of the sensor pad, as opposed to our baseline method which simply conputes ΔE from a white background, and optimally quantizes these responses into five groups. We described a laboratory set-up for capturing the spectral reflectances of the detection devices, including an investigation of three possible types of illumination. Having chosen an LED as the best source of illuminantion, we then developed two different machine learning approaches for classifying the level of contamination by As^{3+} into one of five categories: k-nearest-neighbor with sequential forward feature selection to determine the best subset of features, and random forest with principal component analysis for feature reduction. We found that the latter yields the best performance. Finally, we compared the spectral responses, as a function of contaminant level, of the sensor pads within the band 610-630 nm measured with our spectroradiometer to the spectral responses captured by a mobile phone with an inexpensive narrowband filter attached to the front of the camera lens. Based on the similarity of the responses between these two capture modalities, we conclude that the mobile phone narrowband filter

combination could be used as an inexpensive means of accurately measuring heavy metal contaminant levels, as indicated by the color change in our paper-based sensor device.

6. DEEP LEARNING APPROACH FOR CLASSIFYING CONTAMINATION LEVELS WITH LIMITED SAMPLES

6.1 Introduction

Nowadays, convolutional neural networks (CNN) have gained tremendous popularity in computer vision, especially in the image classification domain for better performance than popular image processing methods [73][74]. Deep learning algorithms yield high classification accuracy by using large, annotated datasets of images. Therefore, to develop accurate image classifiers for the contamination-levels classification task, we need a large dataset of images of colorimetric responses. However, obtaining large-scale datasets of detection images of contamination levels is challenging because of limited test samples.

One approach to overcome this challenge is to use data augmentation, a standard procedure to obtain good performance by deploying rotation, flip, translation, and scaling techniques. Another emerging deep learning generative model inspired by game theory to synthesize images is the Generative Adversarial Network (GAN) [75]. The GAN model consists of a generator to create fake images and a discriminator to distinguish between the real and fake images. These two parts are trained in an adversarial process. Different variations of the classic GAN models have been proposed. As a representative example, pix2pix is a GAN model addressing image-to-image translation problems [76]. Recent medical and biological imaging applications have shown that the GAN framework can successfully generate images and obtain reasonable performance [77][78][79]. Therefore, it is appropriate to apply a GAN model to generate synthetic images for our training purposes.

We aim to solve the classification problem posed by a small scale of data samples and large intra-class variance. In this chapter, we propose an approach to generate high-quality colorimetric responses from our detection images captured by a phone camera and apply a CNN based on EfficientNet-B0 [80] for the contamination-levels multi-classification. The proposed method is evaluated on five contamination levels, and is compared with our previous work. We hope that the proposed methods can be a strong candidate for phone-based contamination-levels detection. Because the user need only take an image of the test response

using their phone camera and feed the captured image into the proposed model, the model can automatically classify the test sample's contamination level.

The rest of this chapter is organized as follows. In Section 6.2, we present the dataset, explore two methods for generating realistic synthetic images, and evaluate the classification results achieved by the proposed CNN classifier. Section 6.3 reports the experimental results for classifying contamination levels. In Section 6.4, the conclusions and the plans for future work are given.

6.2 Methodology

The main challenges of our project are the small scale of available data samples and the large intra-class variance. To overcome these challenges, we first use traditional data augmentation techniques to enlarge the training dataset of the colorimetric signals (AUG data), then train the proposed CNN model with these training sets, and test with the real test dataset. Finally, we synthesize realistic images using pix2pix (GAN data), and observe the classification accuracy after adding the GAN data to the AUG training set.

6.2.1 Dataset description

In this study, the colorimetric responses of 5 contamination levels (As^{3+}) are used as the experimental data. Our optical system first acquires the colorimetric signals of the biosensors. The optical system mainly consists of a photo studio booth (Amzdeal, purchased from Amazon.com) for providing the controlled D65 illumination environment, a mobile phone camera (iPhone 11 Pro Max, CA, USA), and a fixture to hold the mobile phone. Next, we extract the regions of interest and obtain the corresponding segmentation masks, as illustrated in Figure 6.1. Through the above-mentioned steps, our dataset consists of 126 phone captured images: 35 in Class 1 (0, 1, 2 ppm), 32 in Class 2 (4, 5 ppm), 22 in Class 3 (10 ppm), 15 in Class 4 (20, 30 ppm), and 22 in Class 5 (50 ppm). All the ROIs are resized to a uniform dimension of 200 $\times$ 200 pixels. Finally, we divide the original dataset into a training set, a validation set, and a test set according to the ratio 5: 2: 3, as shown in Table 6.1.

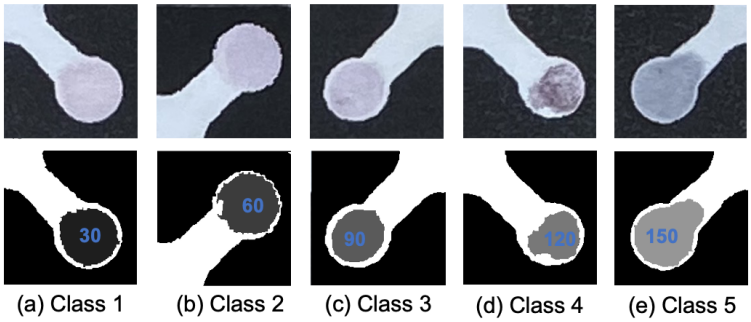

Figure 6.1. Dataset examples of 5 contamination levels: the ROI images of the colorimetric signal and the corresponding segmentation masks (The numbers in blue are the grayscale values. To distinguish different classes, we use different grayscale values to label different classes' response areas).

Table 6.1. Partitioning of the dataset for use with our CNN classifier.

Class	Training set	Validation set	Test set	Total
Class 1	17	7	11	35
Class 2	16	6	10	32
Class 3	11	4	7	22
Class 4	7	3	5	15
Class 5	11	4	7	22

6.2.2 Traditional data augmentation

Deep learning algorithms yield high classification accuracy by using large, annotated datasets of images to train a network. This can cause a danger of overfitting when a deep network deals with a limited numbers of training images. One standard method to address this problem uses traditional data augmentation methods. Classic data augmentation techniques include scaling, cropping, flipping, rotation, translation, and other deformations. The color of the image is important to our application, and we aim to train a classifier to predict the unknown test image's contaminant level based on its colorimetric signal. Therefore, we choose the rotation, flipping, and shifting data augmentation methods, and avoid color deformation.

6.2.3 Generative adversarial network

Another promising tool to generate synthetic images is the Generative Adversarial Net (GAN). The GAN model consists of a discriminator D to discriminate between the real and fake images, and a generator G generating fake images to fool the discriminator. These two parts are trained in an adversarial process. Recent studies have shown that the GAN framework can successfully generate images and obtain good performance [81]. Inspired by [78], we explore pix2pix, a variant of conditional GANs for learning the translation from the binary segmentation images to the colorimetric signal images. The loss function is shown in (6.1).

$$G^* = \arg\min_G \max_D L_{cGAN}(G, D) + \lambda L_{L1}(G) \tag{6.1}$$

Here the generator G tries to minimize this loss function, whereas the discriminator D tries to maximize it, λ is the hyperparameter that balances the $L1$ loss term, which is used to obtain sharp images. One of the limitations of pix2pix is that it requires paired images to train the network. For our application, the input paired images to train the network are the ROI images of the colorimetric signal and the corresponding segmentation masks, as illustrated in Figure 6.1. Then, we only feed the segmentation masks to the trained pix2pix network to generate realistic colorimetric signals.

6.2.4 Proposed CNN architecture

EfficientNet models are based on uniformly scaling the network width, depth, and resolution to yield higher test accuracy and better efficiency with a smaller number of parameters than previous ConvNets, like RestNet-50, and Inception-v2 [82][83]. EfficientNet consists of a series of models from B0 to B7, and the number of parameters varies from 5×10^6 to 66×10^6 [80]. Considering that we focus on a phone-based contamination detection application, we use EfficentNet-B0 with the least number of parameters for transfer learning and to extract features of the generated detection images. To perform the five-contamination-levels classification task, we add a sequence of two fully connected layers with batch normalization, RELU activation functions, and a dropout layer. Finally, the classification layer contains

five output units for 5-class classification based on using the softmax activation function. To test the performance of our proposed CNN classifier, we use accuracy, precision, and F-1 score as the evaluation metrics.

6.3 Experiments and Results

To solve the multi-class classification problem posed by the small scale of our dataset and its large intra-class variance, we explore two kinds of data augmentation techniques, and compare their effectiveness for classifying the five contamination levels. The experiments are set up as follows:

(1) We enlarge our training dataset (AUG training data) by using traditional data augmentation, then calculate the test accuracy of our proposed CNN model trained with the different numbers of the AUG data. Figure 6.2 shows the workflow for evaluating the effects of traditional data augmentation in the task of classifying different contamination levels.

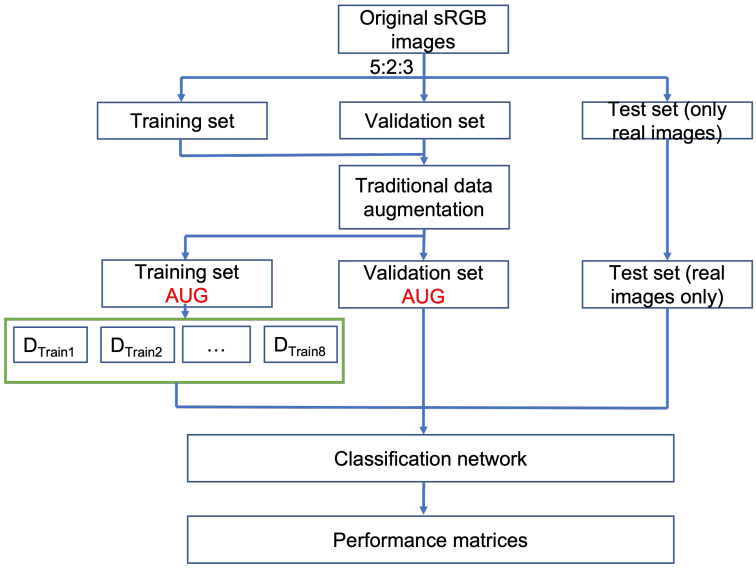

Figure 6.2. Workflow for evaluating traditional data augmentation in the task of classifying different contamination levels.

(2) To compare the classification effects between the traditional data augmentation method and pix2pix, we use the AUG training dataset that yields the highest test accuracy to train pix2pix. Then, we input the segmentation mask of the image in D_{Train8} into pix2pix to generate the corresponding realistic chromaticity signal image. The detailed ex-

perimental procedure is explained in Section 6.3.2. Figure 6.3 shows the block diagram for synthesizing high-quality colorimetric images.

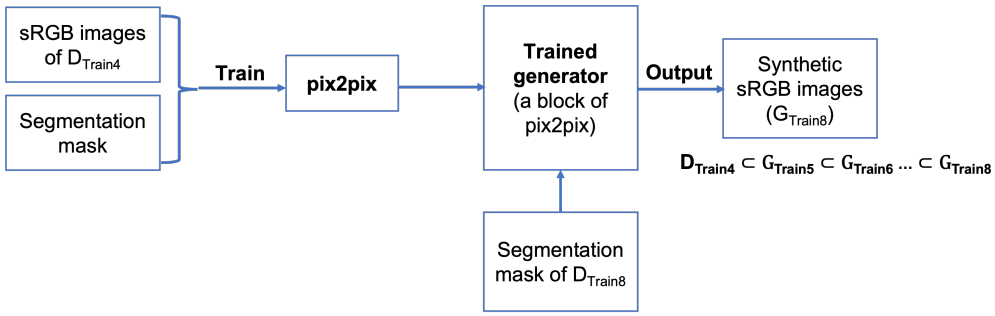

Figure 6.3. Block diagram for synthesizing high-quality colorimetric images.

6.3.1 Traditional data augmentation evaluation

According to the proposed approach, we first apply rotation, flipping, and shifting to produce a large number of images for the training and validation datasets. Here, $N_{rotation} = 70$, $N_{flip} = 2$, and $N_{trans} = 24$. Inspired by [84], we randomly sample the augmented images to additively form the different training dataset groups $D_{Train1} \subset D_{Train2} \subset \ldots \subset D_{Train8}$ such that D_{Train1} only consists of the original training dataset, each class of D_{Train2} includes 1,000 samples, ..., and each class of D_{Train8} includes 7,000 images. Then, we randomly select 1,000 images per class for the validation dataset.

We train the proposed CNN classifier separately for each set of the training groups and evaluate the test results on the same original test dataset. Figure 6.2 shows the workflow of this step. The accuracy results for five contamination levels with the increasing training datasets are illustrated in Figure 6.4. It shows that the classification results improve from 61.9% with no AUG data to 88.1% (D_{Train4}, the optimal AUG data group). We also notice that after D_{Train4}, the classification results drop down slightly and continue to fluctuate around 80%. Table 6.2 presents the confusion matrix for the optimal AUG training data group D_{Train4}. The classification performance using only classic data augmentation (D_{Train4}) yields 91.9% average precision, 86.6% average recall, and 86.7% average F-1 score.

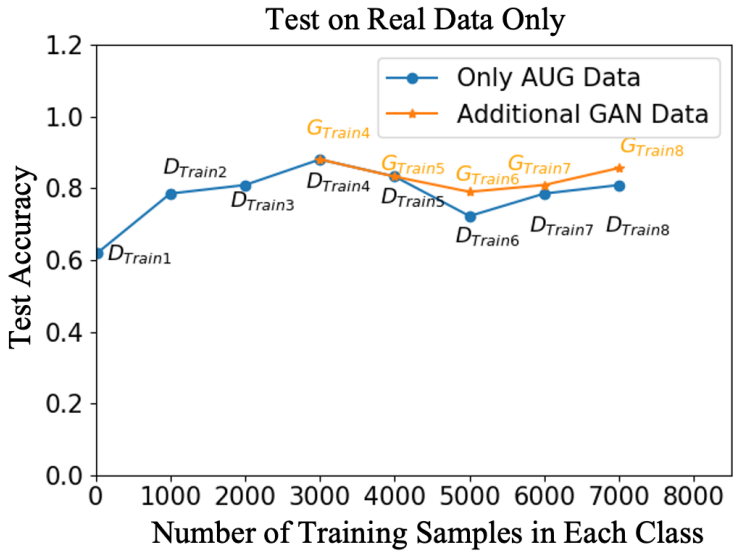

Figure 6.4. Classification results for the five-classes test data as a function of the training set size.

Table 6.2. Confusion matrix for the CNN model trained with the D_{Train4} group.

Class	C 1	C 2	C 3	C 4	C 5	Precision	Recall
C 1	11	0	0	0	0	84.6%	100%
C 2	1	9	0	0	0	75%	90%
C 3	1	3	3	0	0	100 %	42.9%
C 4	0	0	0	5	0	100%	100%
C 5	0	0	0	0	7	100%	100%

6.3.2 Pix2pix data augmentation evaluation

Researchers have reported that the augmented images produced by the traditional data augmentation approach are highly correlated; and GANs are a promising approach to generate a large, diversified dataset of images for training purposes [78][84]. So, we use the optimal AUG data group D_{Train4} to train pix2pix and input the segmentation masks of the well-trained pix2pix to generate a realistic colorimetric images dataset. Here, we also additively form the synthetic training group datasets (GAN data) $D_{Train4} \subset G_{Train5} \subset G_{Train6} \subset G_{Train7} \subset G_{Train8}$. To avoid the influence of the edges in the training group on the classification, the segmentation masks of G_{Train5} and D_{Train5} are the same, and this requirement applies to the rest of the training groups.

Figure 6.3 and Figure 6.5 show the block diagram for synthesizing high-quality colorimetric images and the synthesized high-quality colorimetric images of five-classes with the well-trained pix2pix. Figure 6.6 and Figure 6.4 show the flowchart for evaluating synthetic

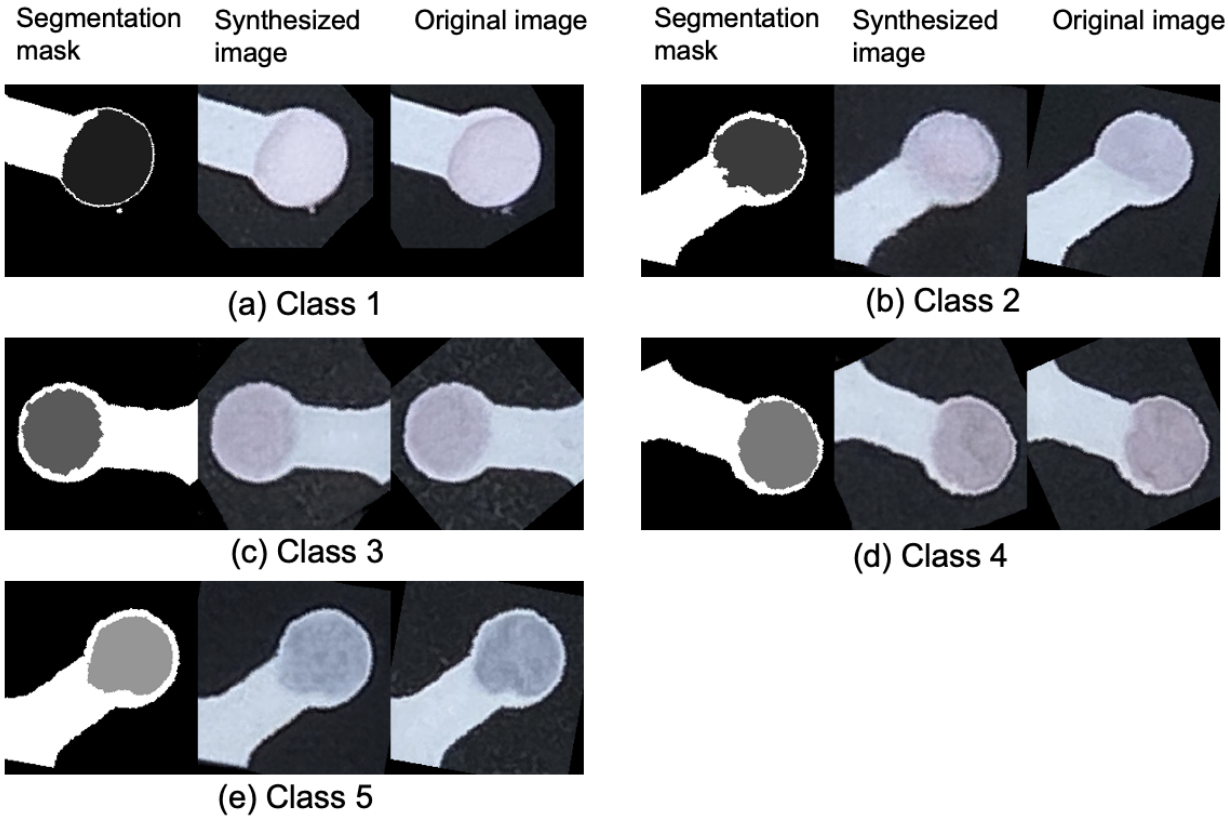

Figure 6.5. Synthesized examples of five-classes with pix2pix. For each class, the figures from left to right are a segmentation mask, a synthesized image generated by a well-trained pix2pix, and the colorimetric signal's original image.

data augmentation in the task of classifying five contamination levels and the test accuracy of the GAN-based synthetic augmentation experiments. Figure 6.4 shows the classification accuracy that is achieved by training with the GAN-based synthetic augmentation images. Even though the highest classification result is still obtained with D_{Train4}, adding the synthetic training data does improve the accuracy for the training sets G_{Train6}, G_{Train7}, and G_{Train8}, compared with the same training set number in the AUG training group. It also reduces the fluctuation in accuracy.

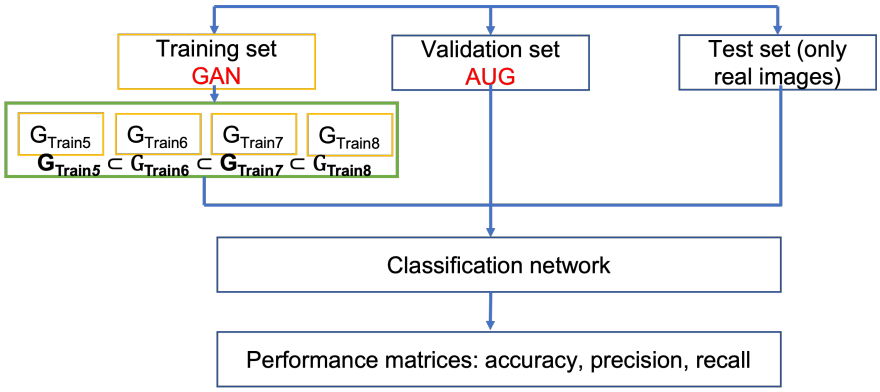

Figure 6.6. Flowchart for evaluating synthetic data augmentation in the task of classifying 5 contamination levels.

6.4 Conclusion

In this chapter, we focused on solving the multi-class classification problem posed by a small scale dataset and large intra-class variance. We proposed a CNN classifier and explored two kinds of data augmentation techniques to compare their effectiveness for a classification task. Moreover, we conclude that this proposed approach demonstrates promising results for a contamination-levels classification task with limited data.

In the future, we plan to extend our work to colorimetric images captured in different ambient illumination environments to provide a more convenient phone-based detection method.

7. SUMMARY AND CONCLUSION

This dissertation mainly discusses two systems for the detection of *E.coli* O157:H7, and As and Hg, respectively.

In Chapter 2, we proposed a system for printing test strips to detect foodborne pathogens, and imaging processing algorithms to analyze images of the exposed test strip that have been captured with a mobile phone camera. The image processing algorithms were designed to detect the presence a pathogen, and to estimate its concentration. The overall goal of the project is to develop a test system that is low-cost, and simple enough to implement in the field. We believe that printing offers a manufacturing method that is low-cost, reliable, and scalable. In Chapter 3, we worked on the response variation of the optical properties of the test lines detecting the target at the same concentration. To reduce the sample-to-sample variation in response to *E.coli* O157:H7, as well as an effort to reduce material cost and printing time, we optimized the numbers of print layers. The analysis data of response variation using the various image segmentation methods has also been given. We evaluated selected thresholding methods for test zone images with the extracted pattern.

Major contributions of Chapter 2 and Chapter 3:

- Developed the printing optimization methods for a higher printing quality with the aid of image processing.

- Developed processes for inkjet printing patterns of aptamer bio-inks with capture biomolecules highly specific for *E. coli* O157:H7 detection. (To best of our knowledge, this is the first report describing nanopatterning of aptamer-based inks for inkjet printed platforms.)

- Created an image analysis system to locate the test (control) lines and efficiently quantify the responses of the test strips to the foodborne pathogen.

- Optimized the ink print layers to reduce the sample-to-sample variation material cost and printing time.

In Chapter 4, we present a novel biosensor using a paper-based, microfluidic architecture. We explored three different printing technologies for fabricating these devices. We then conducted empirical studies to optimize the device geometry. Finally, we developed a complete image processing pipeline to enable detection of the presence of contaminants in the designed test areas. The relationship between the optical properties and the different concentrations of the target was also investigated. The real sample test, specificity test, and stability results prove that our proposed biosensor is highly specific and robust to the analytes.

Major contributions of Chapter 4:

- Developed fabrication methods for fluidics paper-based devices that capture biomolecules highly specific for Hg and As detection.
- Created an image analysis system to locate the response pads and measure the level of response for each pad.
- Quantified and correlated the colorimetric responses of test pads to the different concentrations of heavy metals Hg and As.

In Chapter 5, we worked on improving the accuracy of our previously developed paper-based devices for detecting and measuring heavy metal contaminants in liquids by using the spectral reflectance of the sensor pad. We described a laboratory set-up for capturing the spectral reflectances of the detection devices, including an investigation of three possible types of illumination. We then developed two different machine learning approaches for classifying the level of contamination by As^{3+} into one of five categories. Finally, we compared the spectral responses, as a function of contaminant level, of the sensor pads within the band 610-630 nm measured with our spectroradiometer to the spectral responses captured by a mobile phone with an inexpensive narrowband filter attached to the front of the camera lens. Based on the similarity of the responses between these two capture modalities, we conclude that the mobile phone narrowband filter combination could be used as an inexpensive means of accurately measuring heavy metal contaminant levels, as indicated by the color change in our paper-based sensor device.

Major contributions of Chapter 5:

- Proposed a multispectral classification method to prove that optical spectroscopy can improve the prediction accuracy of heavy metals using the bulky optical component (spectroradiometer).

- Proposed a smartphone-based narrow band spectral imaging system that can obtain the camera spectral response for accurate and precise heavy metals analyses. Our system is incorporated with a hardware plug-in module that fixes the bandpass filter in front of the smartphone's camera.

- Conducted a preliminary evaluation of proposed phone-based narrow band spectral imaging system regarding its performance and capability to replace the spectroradiometer.

In Chapter 6, we focused on solving the multi-class classification problem posed by a small scale dataset and large intra-class variance. We proposed a CNN classifier and explored two kinds of data augmentation techniques to compare their effectiveness for a classification task. Moreover, we concluded that this proposed approach demonstrates promising results for a contamination-levels classification task with limited data.

Major contributions of Chapter 6:

- Explored two kinds of data augmentation techniques (traditional data augmentation and the pix2pix which is a GAN-based augmentation technique) to obtain largescale datasets of detection images of contamination levels and to compare their effectiveness for a classification task.

- Proposed a CNN classifier for five-contamination-levels classification with higher predication accuracy.

REFERENCES

[1] J. Credou, R. Faddoul, and T. Berthelot, "Photo-assisted inkjet printing of antibodies onto cellulose for the eco ^{2}-friendly preparation of immunoassay membranes," *RSC Advances*, vol. 5, no. 38, pp. 29 786–29 798, 2015.

[2] J. T. Delaney, P. J. Smith, and U. S. Schubert, "Inkjet printing of proteins," *Soft Matter*, vol. 5, no. 24, pp. 4866–4877, 2009.

[3] A. Zhdanov, J. Keefe, L. Franco-Waite, K. R. Konnaiyan, and A. Pyayt, "Mobile phone based ELISA (MELISA)," *Biosensors and Bioelectronics*, vol. 103, pp. 138–142, 2018.

[4] E. Archibong, K. R. Konnaiyan, H. Kaplan, and A. Pyayt, "A mobile phone-based approach to detection of hemolysis," *Biosensors and Bioelectronics*, vol. 88, pp. 204–209, 2017.

[5] F. Zhu, M. Bosch, I. Woo, *et al.*, "The use of mobile devices in aiding dietary assessment and evaluation," *IEEE Journal of Selected Topics in Signal Processing*, vol. 4, no. 4, pp. 756–766, 2010.

[6] S.-A. Jin, Y. Heo, L.-K. Lin, *et al.*, "Gold decorated polystyrene particles for lateral flow immunodetection of Escherichia coli O157: H7," *Microchimica Acta*, vol. 184, no. 12, pp. 4879–4886, 2017.

[7] P. Pudil, J. Novovičová, and J. Kittler, "Floating search methods in feature selection," *Pattern recognition letters*, vol. 15, no. 11, pp. 1119–1125, 1994.

[8] E. Fix and J. L. Hodges, "Discriminatory analysis. nonparametric discrimination: Consistency properties," *International Statistical Review/Revue Internationale de Statistique*, vol. 57, no. 3, pp. 238–247, 1989.

[9] L. Breiman, "Random forests," *Machine Learning*, vol. 45, no. 1, pp. 5–32, 2001.

[10] W. C. Wilson Jr and T. Boland, "Cell and organ printing 1: Protein and cell printers," *The Anatomical Record Part A: Discoveries in Molecular, Cellular, and Evolutionary Biology*, vol. 272, no. 2, pp. 491–496, 2003.

[11] J. P. Allebach, G.-Y. Lin, C.-L. Chen, F. A. Baqai, J.-H. Lee, and G. T.-C. Chiu, "Image analysis as a tool for printer characterization and halftoning algorithm development," in *Proceedings Fifth IEEE Southwest Symposium on Image Analysis and Interpretation*, pp. 3–8, 2002.

[12] T. Bhuvana, W. Boley, B. Radha, *et al.*, "Inkjet printing of palladium alkanethiolates for facile fabrication of metal interconnects and surface-enhanced Raman scattering substrates," *Micro & Nano Letters*, vol. 5, no. 5, pp. 296–299, 2010.

[13] P.-H. Chen, W.-C. Chen, and S.-H. Chang, "Bubble growth and ink ejection process of a thermal ink jet printhead," *International Journal of Mechanical Sciences*, vol. 39, no. 6, pp. 683–695, 1997.

[14] A. K. Adak, J. W. Boley, D. P. Lyvers, *et al.*, "Label-free detection of Staphylococcus Aureus captured on immutable ligand arrays," *ACS Applied Materials & Interfaces*, vol. 5, no. 13, pp. 6404–6411, 2013.

[15] E. Bernal, J. Allebach, and Z. Pizlo, "Improved pen alignment for bidirectional printing," *Journal of Imaging Science and Technology*, vol. 51, no. 1, pp. 1–22, 2007.

[16] N. Otsu, "A threshold selection method from gray-level histograms," *IEEE Transactions on Systems, Man, and Cybernetics*, vol. 9, no. 1, pp. 62–66, 1979.

[17] P. Goyal and J. P. Allebach, "Print quality assessment for stochastic clustered-dot halftones using compactness measures," in *2016 IEEE International Conference on Image Processing*, pp. 3792–3796, 2016.

[18] H. Maurer, *New Results and New Trends in Computer Science*. Springer Science & Business Media, vol. 555, 1991.

[19] E. Welzl, "Smallest enclosing disks (balls and ellipsoids)," in *New Results and New Trends in Computer Science*, pp. 359–370, 1991.

[20] Y. Ju, E. Maggard, R. Jessome, and J. Allebach, "Autonomous detection of text fade point with color laser printers," in *Image Quality and System Performance XII*, vol. 9396, 93960G, 2015.

[21] Y. Lei, "Camera/projector-based document/object capture system using structured light: Reflectance map image quality assessment and design of structured light patterns and analysis algorithms," Ph.D. dissertation, Purdue University, 2014.

[22] W. Wang, "A study on image quality evaluation in image capture and production process," Ph.D. dissertation, Purdue University, 2016.

[23] D. N. Breslauer, R. N. Maamari, N. A. Switz, W. A. Lam, and D. A. Fletcher, "Mobile phone based clinical microscopy for global health applications," *PloS one*, vol. 4, no. 7, e6320, 2009.

[24] H. Zhu, O. Yaglidere, T.-W. Su, D. Tseng, and A. Ozcan, "Cost-effective and compact wide-field fluorescent imaging on a cell-phone," *Lab on a Chip*, vol. 11, no. 2, pp. 315–322, 2011.

[25] M. Zhao, S. Diaz Amaya, S.-a. Jin, *et al.*, "Inkjet printing platforms for DNA-based pathogen detection," in *NIP & Digital Fabrication Conference*, pp. 107–112, 2018.

[26] N. R. Pal, "A review on image segmentation techniques," *Pattern Recognition*, vol. 26, no. 9, pp. 1277–1294, 1993.

[27] L. Lucchese and S. K. Mitra, "Colour image segmentation: A state-of-the-art survey," *Proceedings-Indian National Science Academy Part A*, vol. 67, no. 2, pp. 207–222, 2001.

[28] W. Khan, "Image segmentation techniques: A survey," *Journal of Image and Graphics*, vol. 1, no. 4, pp. 166–170, 2013.

[29] A. Z. Arifin and A. Asano, "Image segmentation by histogram thresholding using hierarchical cluster analysis," *Pattern Recognition Letters*, vol. 27, no. 13, pp. 1515–1521, 2006.

[30] P.-S. Liao, T.-S. Chen, P.-C. Chung, *et al.*, "A fast algorithm for multilevel thresholding," *Journal of Information Science and Engineering*, vol. 17, no. 5, pp. 713–727, 2001.

[31] D.-Y. Huang and C.-H. Wang, "Optimal multi-level thresholding using a two-stage Otsu optimization approach," *Pattern Recognition Letters*, vol. 30, no. 3, pp. 275–284, 2009.

[32] P. Sathya and R. Kayalvizhi, "Modified bacterial foraging algorithm based multilevel thresholding for image segmentation," *Engineering Applications of Artificial Intelligence*, vol. 24, no. 4, pp. 595–615, 2011.

[33] C. Cortes and V. Vapnik, "Support-vector networks," *Machine Learning*, vol. 20, no. 3, pp. 273–297, 1995.

[34] H.-F. Ng, "Automatic thresholding for defect detection," *Pattern recognition letters*, vol. 27, no. 14, pp. 1644–1649, 2006.

[35] C.-H. Lee, M. Schmidt, A. Murtha, A. Bistritz, J. Sander, and R. Greiner, "Segmenting brain tumors with conditional random fields and support vector machines," in *International Workshop on Computer Vision for Biomedical Image Applications*, pp. 469–478, 2005.

[36] K. Zhang, J. Deng, and W. Lu, "Segmenting human knee cartilage automatically from multi-contrast MR images using support vector machines and discriminative random fields," in *2011 18th IEEE International Conference on Image Processing*, pp. 721–724, 2011.

[37] H. L. DuPont, "The growing threat of foodborne bacterial enteropathogens of animal origin," *Clinical Infectious Diseases*, vol. 45, no. 10, pp. 1353–1361, 2007.

[38] G. Mance, *Pollution threat of heavy metals in aquatic environments*. Springer Science & Business Media, 2012.

[39] M. Feng, Q. Yong, W. Wang, H. Kuang, L. Wang, and C. Xu, "Development of a monoclonal antibody-based ELISA to detect Escherichia coli O157: H7," *Food and Agricultural Immunology*, vol. 24, no. 4, pp. 481–487, 2013.

[40] S. Díaz-Amaya, M. Zhao, L.-K. Lin, *et al.*, "Inkjet printed nanopatterned aptamer-based sensors for improved optical detection of foodborne pathogens," *Small*, vol. 15, no. 24, p. 1 805 342, 2019.

[41] R. Flamini and A. Panighel, "Mass spectrometry in grape and wine chemistry. Part II: The consumer protection," *Mass Spectrometry Reviews*, vol. 25, no. 5, pp. 741–774, 2006.

[42] P. Pohl, "Determination of metal content in honey by atomic absorption and emission spectrometries," *TrAC Trends in Analytical Chemistry*, vol. 28, no. 1, pp. 117–128, 2009.

[43] J. Wang, G. Liu, and A. Merkoçi, "Electrochemical coding technology for simultaneous detection of multiple DNA targets," *Journal of the American Chemical Society*, vol. 125, no. 11, pp. 3214–3215, 2003.

[44] M. Saidur, A. A. Aziz, and W. Basirun, "Recent advances in DNA-based electrochemical biosensors for heavy metal ion detection: A review," *Biosensors and Bioelectronics*, vol. 90, pp. 125–139, 2017.

[45] L. S. A. Busa, S. Mohammadi, M. Maeki, A. Ishida, H. Tani, and M. Tokeshi, "Advances in microfluidic paper-based analytical devices for food and water analysis," *Micromachines*, vol. 7, no. 5, p. 86, 2016.

[46] Y. Zhang, P. Zuo, and B.-C. Ye, "A low-cost and simple paper-based microfluidic device for simultaneous multiplex determination of different types of chemical contaminants in food," *Biosensors and Bioelectronics*, vol. 68, pp. 14–19, 2015.

[47] C. Xu, L. Cai, M. Zhong, and S. Zheng, "Low-cost and rapid prototyping of microfluidic paper-based analytical devices by inkjet printing of permanent marker ink," *Rsc Advances*, vol. 5, no. 7, pp. 4770–4773, 2015.

[48] W. Dungchai, O. Chailapakul, and C. S. Henry, "A low-cost, simple, and rapid fabrication method for paper-based microfluidics using wax screen-printing," *Analyst*, vol. 136, no. 1, pp. 77–82, 2011.

[49] P. J. Lamas-Ardisana, P. Casuso, I. Fernandez-Gauna, *et al.*, "Disposable electrochemical paper-based devices fully fabricated by screen-printing technique," *Electrochemistry Communications*, vol. 75, pp. 25–28, 2017.

[50] A. K. Yetisen, J. Martinez-Hurtado, A. Garcia-Melendrez, F. da Cruz Vasconcellos, and C. R. Lowe, "A smartphone algorithm with inter-phone repeatability for the analysis of colorimetric tests," *Sensors and Actuators B: Chemical*, vol. 196, pp. 156–160, 2014.

[51] R. Brunelli, *Template matching techniques in computer vision: theory and practice*. John Wiley & Sons, 2009.

[52] J. A. Hartigan and M. A. Wong, "A k-means clustering algorithm," *Journal of the Royal Statistical Society. Series C (Applied Statistics)*, vol. 28, no. 1, pp. 100–108, 1979.

[53] J. Serra, "Morphological filtering: An overview," *Signal processing*, vol. 38, no. 1, pp. 3–11, 1994.

[54] Q. Chen, P. Gong, D. Baldocchi, and G. Xie, "Filtering airborne laser scanning data with morphological methods," *Photogrammetric Engineering & Remote Sensing*, vol. 73, no. 2, pp. 175–185, 2007.

[55] J. Bednar and T. Watt, "Alpha-trimmed means and their relationship to median filters," *IEEE Transactions on acoustics, speech, and signal processing*, vol. 32, no. 1, pp. 145–153, 1984.

[56] S. Díaz-Amaya, M. Zhao, J. P. Allebach, G. T.-C. Chiu, and L. A. Stanciu, "Ionic strength influences on biofunctional Au-decorated microparticles for enhanced performance in multiplexed colorimetric sensors," *ACS Applied Materials & Interfaces*, vol. 12, no. 29, pp. 32 397–32 409, 2020.

[57] M. Zhao, S. Diaz-Amaya, A. J. Deering, L. Stanciu, G. T.-C. Chiu, and J. P. Allebach, "Image analytics for food safety," *Electronic Imaging*, vol. 2020, no. 8, pp. 302–1, 2020.

[58] M. Zhao, R. Zhang, S. Diaz-Amaya, *et al.*, "Detection, imaging, and quantification of DNA-based pathogen based on inkjet-printed test strips," in *NIP & Digital Fabrication Conference*, vol. 2019, pp. 177–181, 2019.

[59] S. Lloyd, "Least squares quantization in PCM," *IEEE Transactions on Information Theory*, vol. 28, no. 2, pp. 129–137, 1982.

[60] J. Max, "Quantizing for minimum distortion," *IRE Transactions on Information Theory*, vol. 6, no. 1, pp. 7–12, 1960.

[61] J. C. Platt, N. Cristianini, J. Shawe-Taylor, *et al.*, "Large margin dags for multiclass classification.," in *nips*, vol. 12, 1999, pp. 547–553.

[62] R. Zhang, E. Maggard, Y. Bang, M. Cho, M. Shaw, and J. Allebach, "Color text fading detection," *Electronic Imaging*, vol. 2021, no. 16, pp. 253–1, 2021.

[63] M. Kearns and D. Ron, "Algorithmic stability and sanity-check bounds for leave-one-out cross-validation," *Neural computation*, vol. 11, no. 6, pp. 1427–1453, 1999.

[64] A. Bierman, M. G. Figueiro, and M. S. Rea, "Measuring and predicting eyelid spectral transmittance," *Journal of Biomedical Optics*, vol. 16, no. 6, p. 067 011, 2011.

[65] A. G. Wee, D. T. Lindsey, S. Kuo, and W. M. Johnston, "Color accuracy of commercial digital cameras for use in dentistry," *Dental Materials*, vol. 22, no. 6, pp. 553–559, 2006.

[66] K. Fukunaga, *Introduction to statistical pattern recognition*. Elsevier, 2013.

[67] N. S. Altman, "An introduction to kernel and nearest-neighbor nonparametric regression," *The American Statistician*, vol. 46, no. 3, pp. 175–185, 1992.

[68] A. Liaw, M. Wiener, *et al.*, "Classification and regression by randomforest," *R News*, vol. 2, no. 3, pp. 18–22, 2002.

[69] H. Hotelling, "Analysis of a complex of statistical variables into principal components," *Journal of Educational Psychology*, vol. 24, no. 6, p. 417, 1933.

[70] M.-L. Zhang and Z.-H. Zhou, "ML-KNN: A lazy learning approach to multi-label learning," *Pattern Recognition*, vol. 40, no. 7, pp. 2038–2048, 2007.

[71] S. Zhang, X. Li, M. Zong, X. Zhu, and R. Wang, "Efficient KNN classification with different numbers of nearest neighbors," *IEEE Transactions on Neural Networks and Learning Systems*, vol. 29, no. 5, pp. 1774–1785, 2017.

[72] A. Amjad, R. Ullah, S. Khan, M. Bilal, and A. Khan, "Raman spectroscopy based analysis of milk using random forest classification," *Vibrational Spectroscopy*, vol. 99, pp. 124–129, 2018.

[73] S. P. Mohanty, D. P. Hughes, and M. Salathé, "Using deep learning for image-based plant disease detection," *Frontiers in Plant Science*, vol. 7, p. 1419, 2016.

[74] A. Krizhevsky, I. Sutskever, and G. E. Hinton, "ImageNet classification with deep convolutional neural networks," *Advances in Neural Information Processing Systems*, vol. 25, pp. 1097–1105, 2012.

[75] I. Goodfellow, J. Pouget-Abadie, M. Mirza, *et al.*, "Generative adversarial nets," *Advances in Neural Information Processing Systems*, vol. 27, 2014.

[76] P. Isola, J.-Y. Zhu, T. Zhou, and A. A. Efros, "Image-to-image translation with conditional adversarial networks," in *Proceedings of the IEEE Conference on Computer Vision and Pattern Recognition*, pp. 1125–1134, 2017.

[77] M. Frid-Adar, I. Diamant, E. Klang, M. Amitai, J. Goldberger, and H. Greenspan, "GAN-based synthetic medical image augmentation for increased CNN performance in liver lesion classification," *Neurocomputing*, vol. 321, pp. 321–331, 2018.

[78] H. Hu, Y. Lei, D. Xin, *et al.*, "2D label free microscopy imaging analysis using machine learning," *Electronic Imaging*, vol. 2020, no. 14, pp. 341–1, 2020.

[79] Y. Liu, Y. Zhou, X. Liu, F. Dong, C. Wang, and Z. Wang, "Wasserstein GAN-based small-sample augmentation for new-generation artificial intelligence: A case study of cancer-staging data in biology," *Engineering*, vol. 5, no. 1, pp. 156–163, 2019.

[80] M. Tan and Q. Le, "EfficientNet: Rethinking model scaling for convolutional neural networks," in *International Conference on Machine Learning*, pp. 6105–6114, 2019.

[81] P. Costa, A. Galdran, M. I. Meyer, *et al.*, "Towards adversarial retinal image synthesis," *arXiv:1701.08974*, 2017.

[82] K. He, X. Zhang, S. Ren, and J. Sun, "Deep residual learning for image recognition," in *Proceedings of the IEEE Conference on Computer Vision and Pattern Recognition*, pp. 770–778, 2016.

[83] C. Szegedy, V. Vanhoucke, S. Ioffe, J. Shlens, and Z. Wojna, "Rethinking the inception architecture for computer vision," in *Proceedings of the IEEE Conference on Computer Vision and Pattern Recognition*, pp. 2818–2826, 2016.

[84] M. Frid-Adar, E. Klang, M. Amitai, J. Goldberger, and H. Greenspan, "Synthetic data augmentation using GAN for improved liver lesion classification," in *2018 IEEE 15th International Symposium on Biomedical Imaging*, pp. 289–293, 2018.

VITA

Min Zhao is a graduate student in Electrical and Computer Engineering Department at Purdue University under the supervision of Professor Jan P. Allebach. She received her B.S. degree in Mechanical Engineering from Qingdao Technological University, Shandong, China. Her current research interests include image processing, computer vision, machine learning, and deep learning.